Effects of heating configuration and operating parameters on heat transfer and interfacial physics of microgravity flow boiling with subcooled inlet conditions – Experiments onboard the International Space Station

Issam Mudawar[a,*], V.S. Devahdhanush[a], Steven J. Darges[a],

Mohammad M. Hasan[b], Henry K. Nahra[b], R. Balasubramaniam[c], Jeffrey R. Mackey[d]

[a] Purdue University Boiling and Two-Phase Flow Laboratory (PU-BTPFL), School of Mechanical Engineering, Purdue University, 585 Purdue Mall, West Lafayette, IN 47907, USA

[b] NASA Glenn Research Center, 21000 Brookpark Road, Cleveland, OH 44135, USA

[c] Case Western Reserve University, 10900 Euclid Ave., Cleveland, OH 44106, USA

[d] HX5, LLC 3000 Aerospace Parkway, Brookpark, OH 44142, USA

Abstract – This study is part of the Flow Boiling and Condensation Experiment (FBCE), a collaborative effort between the Purdue University Boiling and Two-Phase Flow Laboratory (PU-BTPFL) and the NASA Glenn Research Center. The FBCE fitted with the Flow Boiling Module (FBM) was launched to the International Space Station (ISS) in August 2021 and experiments were successfully performed from February to July 2022 to amass a large microgravity-flow-boiling database. This study is focused on heat transfer and flow visualization of microgravity flow boiling of n-Perfluorohexane in a rectangular channel of 5.0 mm height, 2.5 mm width (heated), and 114.6 mm length, with subcooled inlet conditions. High-speed-video photography is utilized to present flow patterns and temporal interfacial behavior. Heat transfer results are presented in the form of flow boiling curves and both parametric curves and streamwise profiles of wall temperature and heat transfer coefficient. Firstly, the parametric effects of mass velocity (199.4 – 3200.0 kg/m^{2}s), inlet subcooling (0.2 – 46.0°C), and inlet pressure (124.2 – 176.7 kPa), on the aforementioned aspects are assessed for double-sided heating to establish them for a microgravity environment. Of these three parameters, mass velocity and inlet subcooling mostly determine the microgravity flow boiling behavior, while inlet pressure plays an insignificant role. Flow patterns for double-sided heating are more complex than those for single-sided heating due to interaction between the two vapor layers. Vapor interaction is minimized at high subcoolings and high mass velocities due to strong condensation offered by the subcooled bulk liquid layer separating them. Despite the different flow patterns, both single- and double-sided heating generally result in similar parametric trends and local heat transfer coefficients for similar operating conditions. Flow instabilities manifest as temporal flow anomalies and temperature oscillations, and their severity increases with increasing boiling number. Secondly, the effects of heating configuration are analyzed by comparing and contrasting several aspects of single- and double-sided heating data. The heat fluxes at which onset of nucleate boiling degradation (ONBD) and critical heat flux (CHF) occur are distinctly different for single- and double-sided heating.

There exists a threshold inlet subcooling demarcating the dominance of flow acceleration and condensation effects in vapor removal from the near-wall region and replenishment of fresh liquid for boiling. Above the threshold, condensation from the near-wall region is dominant and single-sided heating yields higher heat fluxes, and below it, acceleration is dominant and double-sided yields higher heat fluxes. At mass velocity in the range of 200 – 2400 kg/m^{2}s, the threshold inlet subcooling lies in the approximate range of 20 – 30°C (corresponding inlet quality of roughly -0.40 – -0.20).

Keywords: flow boiling; subcooled inlet; double-sided heating; two-phase heat transfer coefficient; interfacial physics; microgravity; heating configuration, International Space Station

* Author to whom correspondence should be addressed; Tel. (765) 494-5705; Fax (765) 494-0539; E-mail: *mudawar@ecn.purdue.edu;* Website: *https://engineering.purdue.edu/BTPFL*

Nomenclature

A	area [m^2]
A_c	cross-sectional area [m^2]
D_h	hydraulic diameter [m]
G	mass velocity [kg/m^{2}s]
g	gravitational acceleration [m/s^2]
g_e	gravitational acceleration on Earth [m/s^2]
μg_e	microgravity [m/s^2]
H	height of channel's cross section [m]
H_{tc}	conduction distance through heating strip [m]
h	enthalpy [J/kg]; heat transfer coefficient [W/m^{2}K]
$\overline{h}$	average heat transfer coefficient [W/m^{2}K]
h_{fg}	latent heat of vaporization [J/kg]
k	thermal conductivity [W/m.K]
L_d	upstream development length [m]
L_e	downstream exit length [m]
L_h	heated length [m]
$\dot{m}$	mass flow rate [kg/s]
N_z	number of streamwise measurement locations
P_h	heated perimeter [m]
p	pressure [Pa]
q''	heat flux [W/m^2]
q''_{CHF}	critical heat flux [W/m^2]

q''_{ONBD}	heat flux corresponding to ONBD [W/m^2]
T	temperature [°C]
$\overline{T}$	average temperature [°C]
ΔT_{sub}	fluid subcooling, $\Delta T_{sub} = T_{sat} - T_f$ [°C]
t	time [s]
u	velocity [m/s]
W	width of channel's cross section [m]
x_e	thermodynamic equilibrium quality
z	streamwise coordinate [m]

Subscripts

a	denotes wall 1 or 2 (= 1 or 2)
f	liquid; bulk fluid
g	vapor
h	heated
in	inlet to channel heated section
out	outlet of channel heated section
s	solid
sat	saturation
sp	single-phase
tc	thermocouple in heating strip
w	wall
wa	wall 1 or 2 (= *w*1 or *w*2)
x=0	corresponding to the location where $x_e = 0$
z	local (along streamwise direction)

Acronyms

BHM	Bulk Heater Module
CHF	Critical Heat Flux
DC	Direct Current
ESA	European Space Agency
FBCE	Flow Boiling and Condensation Experiment
FBM	Flow Boiling Module
FDB	Fully Developed Boiling
FIR	Fluid Integrated Rack
GRC	NASA's Glenn Research Center

ISS	International Space Station
MST	Mission Sequence Testing
nPFH	n-Perfluorohexane
NBD	Nucleate Boiling Degradation
ONB	Onset of Nucleate Boiling
ONBD	Onset of Nucleate Boiling Degradation
PDB	Partially Developed Boiling
PU-BTPFL	Purdue University Boiling and Two-Phase Flow Laboratory
RDAQM1	Remote Data Acquisition Module 1
RDAQM2	Remote Data Acquisition Module 2
RTD	Resistance Temperature Detector

1. Introduction

1.1 Boiling Heat Transfer in Aerospace Applications

NASA and other aerospace agencies around the world are both pursuing several highly complex space missions and developing highly advanced aircraft. These goals have one aspect in common – the new systems and components are very powerful compared to their existing counterparts, while being smaller and lighter in weight. While these new systems achieve enhanced performance and efficiencies, their energy densities are very high, meaning increased heat fluxes for cooling. Adequate thermal management of these systems and components is vital for their safe and reliable operation, and for the success of these aerospace endeavors. Although forced liquid convection heat transfer enables cooling of the existing systems, it cannot cater to the increased demands of the newer systems. Boiling heat transfer on the other hand, would be a prime contender to cool these new systems, due to its ability to dissipate copious amounts of heat while maintaining the system's temperature at low safe levels. This is because boiling relies on the fluid's latent heat of vaporization to yield heat transfer coefficients an order or more in magnitude than forced convection with no phase change. Boiling can be implemented in a variety of flow schemes, such as flows through capillary devices, macro-channels, micro-channels, and annuli, and in sprays and impinging jets, which all have been carefully researched at the Purdue University Boiling and Two-Phase Flow Laboratory (PU-BTPFL) and other research labs around the world. For aerospace applications, channel flow boiling (*i.e.*, boiling implemented in forced-convective flows in channels) is the most suitable of all schemes due to (i) its reliance on flow inertia to remove the produced vapor and replenish the walls with fresh liquid for boiling, (ii) need for relatively low pumping power, (iii) simplicity of implementation, (iv) ability to simultaneously cool multiple components in series, and (v) operation in a fully closed flow loop.

In a recent 2019 workshop [1], NASA recommended boiling schemes for the safe operation of several aerospace systems including high-power-density energy conversion equipment, avionics, Rankine-power-cycle-based Fission Power Systems (FPS), and onboard life support systems.

1.2 Effects of Gravitational Field on Boiling Heat Transfer

Aerospace applications experience gravitational fields ranging from microgravity (μg_e) in space to reduced gravity on Mars and the Moon ($< 1g_e$) to Earth gravity ($1g_e$) to hypergravity (>1 g_e) within fighter aircrafts and accelerating systems. Due to the simultaneous presence of two phases, *viz*. liquid and vapor having densities differing by several orders of magnitude, boiling schemes are extremely affected by the external gravitational field. This means developing boiling schemes for aerospace applications requires a thorough understanding of the heat transfer and flow physics and the effects of gravity on them. While these aspects are well understood in Earth gravity, the same is not true for other gravitational environments.

The effects of gravity (especially reduced gravity) have been studied via several experimental techniques. The simplest and least expensive technique is to perform experiments by having the flow geometry and/or heated surface orientated at different angles with respect to Earth gravity. At each orientation, the gravitational field's components acting on the fluid are different, so the effects of each component can be isolated, and the overall effects of gravity established. Experiments based on this technique have led to the development of criteria for gravity independent operation of flow boiling [2] and flow condensation [3]. This technique has its advantages and provides a preliminary assessment of gravity effects. However, the main disadvantage is the strength of the gravitational field is not changed and hence the experiments cannot accurately capture the effects of reduced gravity.

To overcome such drawbacks, experiments can be performed in a reduced gravity field by techniques utilizing drop towers, sounding/suborbital/ballistic rockets, parabolic flights, space shuttles/recoverable satellites, and the International Space Station (ISS) [4].

1.2.1 Flow Boiling Experiments in Short Periods of Microgravity

To conduct flow boiling experiments in short periods of microgravity, researchers most commonly utilize drop towers, parabolic flights, and sounding rockets (in ascending order of μg_e duration), all of which establish truly short periods of μg_e lasting from a few seconds to several minutes. Compared to pool boiling (boiling in a stagnant pool of liquid), fewer experiments have studied flow boiling. Some notable flow boiling studies in short term μg_e include the parabolic-flight and drop-tower experiments summarized in Table 1. The second column provides

information on the experiment type/platform, fluid, boiling geometry, and experimental operating conditions. The third column summarizes the key observations and conclusions of that study.

Even though short-term μg_e experiments are cost effective and yield some μg_e data, they suffer from several issues inherent to the experimental technique. For instance, although drop towers establish a high quality of μg_e, the established μg_e period is too short to reach steady state for most experiments [21]. On the other hand, although parabolic flights and sounding rockets establish longer μg_e durations relative to drop towers, (i) parabolic flights establish a relatively poor μg_e quality due to typical small fluctuations in the μg_e level (termed *g-jitter*) [22], which artificially enhances heat transfer [23], and (ii) sounding rockets suffer from excessive launch loads and μg_e durations of ~15 minutes.

1.2.2 Flow Boiling Experiments in Long Durations of Stable Microgravity

Of all μg_e experimental techniques, the most accurate and highest quality μg_e data were obtained by performing experiments onboard space shuttles, recoverable satellites, and the ISS, all of which help establish extremely lengthy periods of very stable μg_e. Despite the clear scientific advantages, few boiling experiments have utilized these venues, mainly due to their enormous cost, high possibility of failure, long times to obtain results, and volume, mass, and power constraints at the venue. These techniques were initially used for pool boiling experiments, which include Lee *et al.* [25] and Merte [26] onboard NASA space shuttles, Zhao *et al.* [27,28] onboard Chinese recoverable satellites, and the Microheater Array Boiling Experiment (MABE) [23] and Nucleate Pool Boiling eXperiment (NPBX [29,30]) onboard the ISS.

In 2022, several researchers supported by the European Space Agency (ESA) outlined a multiscale boiling experiment for the ISS aiming to: (i) observe both contact line behavior and bubble growth, (ii) assess the effects of an electric field, shear flow, and binary mixtures, all with respect to single bubbles, and (iii) bubble interaction effects. Image analysis algorithms to process the ISS data for μg_e subcooled boiling from ESA's multiscale boiling experiment have been reported in [31] and a benchmark analysis performed. In this regard, as evident from [32] and the references included within [33], Marco *et al*. have been studying various aspects of application of electric fields on single bubbles and boiling, including how to use an electric field as a replacement to buoyancy for two-phase flows.

Table 1 Summary of some notable studies on flow boiling in short-term microgravity.

Author(s) (Year)	Experiment Type and Specifications	Key Observations and Conclusions
Misawa (1993) [5]	• Drop tower experiments • R-113 • Uniformly heated, vertical, square channel of 5 × 5 mm^2 cross section and 0.5 m length • G = 37.7, 114.4 kg/m^2s for flow pattern observation and 75 – 570 kg/m^2s for pressure drop measurement • $\Delta T_{sub,in}$ = 4.6, 17.0°C for flow patterns and 3.1 – 4.5°C for pressure drop • $x_{e,out}$ = -0.045 – 0.175 for flow patterns and 0.002 – 0.207 fore pressure drop • q''_w = 2.9 kW/m^2	• In μg_e, bubbly flow regime had a significantly different void distribution. • Radial distributions of velocity and temperature in bubbly flow were different due to increased void fraction and bubble coalescence. • μg_e reduced bubble-induced turbulence, which usually aids heat transfer in $1g_e$. • The increased void fraction in μg_e, amplified the accelerational and frictional components of pressure drop at low qualities, resulting in significant pressure drops in the subcooled boiling regimes.
Misawa (1993) [5]	• Parabolic flight experiments • R-113 • Uniformly heated, vertical copper tube of 11.3 mm diameter and 0.5 m length • G = 37 – 384 kg/m^2s • $\Delta T_{sub,in}$ = 25.4 – 42.9°C • p_{in} = 0.94 – 1.43 bar • q''_w = 23.9 kW/m^2	• The absence of buoyancy in μg_e lessened bulk convection, resulting in higher wall superheats near the channel exit. • μg_e increased void fraction and stagnated coalesced bubbles in the subcooled boiling regime. • Overall flow boiling heat transfer coefficients were smaller in μg_e compared to vertically upward flows in Earth gravity.
Saito *et al*. (1994) [6]	• Parabolic flight experiments • Water • Horizontal heated rod of 8 mm diameter placed in a square channel of 25 × 25 mm^2 cross section	• Bubble detachment decreased in μg_e, instead bubble growth and coalescence produced large bubbles, which enveloped the downstream of the heater rod. • This behavior was amplified at low mass velocities, high heat fluxes, and low inlet subcoolings. • Local heat transfer coefficients at the bottom of the heater rod deteriorated in μg_e due to the absence of natural convection.

	• u_{in} = 3.7 – 22.9 cm/s • p = 0.9 – 2.04 bar • T_{in} = 86.1 – 112.8°C • q''_w = 5.3 – 18.6 W/cm^2	• Local heat transfer coefficients at the top of the heater rod were slightly augmented in μg_e. • Despite the significantly different flow regimes between μg_e and $1g_e$, differences in heat transfer coefficient were minimal.
Ohta (1997) [7]	• Parabolic flight experiments • R-113 • Glass tube of 8 mm diameter and coated with a thin resistive gold film • G = 150, 600 kg/m^{2}s • $x_{e,in}$ = 0 – 0.8 • p = 1.1 – 2.2 bar • $q''_w = 5\times10^3 – 1.5\times10^5$ W/m^2	• At both low and high mass velocities, nucleate boiling heat transfer in the low-quality bubbly flow regime at low qualities were similar in μg_e and $1g_e$. • Nucleate boiling in the annular flow regime at moderate qualities was suppressed and heat transfer deteriorated in μg_e. At high heat fluxes, nucleate boiling within the annular liquid film suppressed the effects of gravity. • The higher flow inertia, associated with the annular flow regime at high qualities, suppressed the effects of gravity even at low heat fluxes. • At high qualities, dryout-type CHF values (q''_{CHF}) were similar in μg_e and $1g_e$. • Vapor production was higher in μg_e, resulting in larger bubble diameters and regime transition to annular flow at lower qualities.
Ma and Chung (1998) [8]	• Drop tower experiments • FC-72 • Flat square 25.4 × 25.4 mm^2 gold film heater • u_{in} = 0 – 30 cm/s • ΔT_{sub} = 26°C • p = 112 kPa • q''_w = 23.2 – 73.3 kW/m^2	• In μg_e, compared to pool boiling, the forced convective effects in flow boiling significantly reduced bubble sizes and sustained the nucleate boiling regime for higher heat fluxes. • Higher mass velocities reduced bubble sizes and lessened average surface superheats, thereby augmenting heat transfer coefficients. • A two-dimensional boiling map was drawn for in μg_e conditions as a function of Reynolds number and dimensionless heat flux. This showed stronger forced convective effects caused μg_e boiling to primarily occur within the nucleate/transition regime rather than film boiling, thereby yielding much higher heat transfer coefficients.
Ma and Chung (2001) [9]	• Drop tower experiments • FC-72 • Platinum wire of 0.01 inch diameter • u_{in} = 22 cm/s in μg_e and 0 – 30 cm/s in $1g_e$. • ΔT_{sub} = 26°C • p = 112 kPa	• At low mass velocities, bubble behavior was drastically different between μg_e and $1g_e$. Bubble significantly coalesced in μg_e, while they typically departed the nucleation site in $1g_e$. • q''_{CHF} was significantly degraded in μg_e, easily transitioning boiling to the transition/film boiling regime. • In both μg_e and $1g_e$, higher mass velocities ameliorated q''_{CHF} and 'raised' the boiling curves to higher heat fluxes. • Sufficiently high mass velocities completely suppressed the effects of gravity on CHF and flow behavior.
Zhang *et al*. (2005) [10]	• Parabolic flight experiments • FC-72 • Rectangular channel of 101.6 mm	• At high heat fluxes, bubbles coalesced into large patches on the heated wall, and close to CHF, these patches lengthened to form a wavy vapor layer. The only liquid to the heated wall was through the wave troughs.

	length and 5 × 2.5 mm^2 cross section with one narrow wall heated • u_{in} = 0.14 – 1.5 m/s • $\Delta T_{sub,out}$ = 2 – 23°C • p_{out} = 138 – 152 kPa	• The wavy vapor became thinner at higher inlet subcooling and mass velocities due to higher subcooling promoting bulk fluid condensation and high flow rates increasing drag force. • CHF was triggered when intense boiling within the wave troughs completely lifted the wavy layer off the wall, which was consistent with the *Interfacial Lift-Off Model* CHF mechanism. • At low velocities, q''_{CHF} in μg_e was significantly smaller than in $1g_e$. The difference became smaller upon increasing velocity, and at velocities higher than 1.5 m/s, the values converged.
Luciani *et al*. (2008) [11]	• Parabolic flight experiments • HFE-7100 • Mini-channels of 6 × 0.254, 6 × 0.454, and 6 × 0.654 mm^2 cross sections • $\dot{m}$ = 1 – 4 g/s • $\Delta T_{sub,in}$ = 2°C • p = 0.82 bar • q''_w = 33 kW/m^2	• Inverse heat conduction techniques were couples with experimental data to determine local heat fluxes and local surface temperatures at several locations. However, the large noise/disturbances in the sensors led to large uncertainties in determining the local values. Proposed solutions to rectify this issue were to use X-ray tomography to determine precise locations of thermocouples and heating wires and implement infrared measurements. • μg_e generated large vapor structures, which filled the entire width of the channels, resulting in locally high heat transfer coefficients. • Analysis of surface temperature profiles revealed exceedingly small temperature variations (<1°C) between hypergravity and μg_e.
Luciani *et al*. (2009) [12]	• Parabolic flight experiments • HFE-7100 • Micro-channel of 50 mm length and 6 × 0.254 mm^2 cross section • $\Delta T_{sub,in}$ = 2°C	• To address to shortcoming in their prior study [11], X-ray tomography was used to perform a tomography of 20 μm resolution of their cement rods, which houses thermocouples and heating wires. Once again, temperature measurement noise resulted in large uncertainties and errors in their calculations. Moreover, the profiles did not attain steady state when transitioning between gravity levels in the parabolic flight. • Heat transfer coefficient was ~30% higher in μg_e than both $1g_e$ and $2g_e$.
Baltis *et al*. (2012) [13]	• Parabolic flight experiments • FC-72 • Tubes of 2.0, 4.0, and 6.0 mm diameters • G = 47.5 – 570.0 kg/m^{2}s • $\Delta T_{sub,in}$ = 9 – 30°C • p = 1.2 – 1.8 bar • $x_{e,out} < 0.4$ • $q''_w < 10$ W/cm^2	• Heat transfer was significantly enhanced in μg_e, particularly near the tube entrance, due to larger bubbles enhancing mixing and turbulence. The corresponding flow patterns were bubbly flow in $1g_e$ and intermittent flow in μg_e. • At high qualities, the differences in heat transfer between $1g_e$ and μg_e were minimal. • Higher mass velocities suppressed the effects of gravity. For the 6 mm diameter tube, gravity affects heat transfer only for mass velocities lower than 425 kg/m^{2}s. • Smaller diameter tubes had narrower operating conditions where the effects of gravity on flow boiling were prominent. • The 2 mm diameter tube was most prone, for most operating conditions, to produce severe flow instabilities and CHF occurrence in μg_e.

Brutin *et al.* (2013) [14]	• Parabolic flight experiments • HFE-7100 • Mini-channel of 6 × 0.454 mm^2 cross section • G = 30 – 248 kg/m^2s • q''_w = 15 – 55 kW/m^2	• This study focused on local void fraction estimation and frictional pressure drop measurements and complements their heat transfer study in [12]. • Typically, frictional pressure drops in μg_e and $1.8g_e$ were respectively ~0.5× and 1.3× than that in $1g_e$. • Bubbles grew quicker in μg_e than $1.8g_e$, typically producing bubbles of relatively smaller diameters in $1.8g_e$ and bigger slugs in μg_e. • Larger bubbles growth and larger bubble departure diameters in μg_e produced thinner films, increasing heat transfer rates, and smaller effective liquid cross-sectional areas, reducing frictional pressure drop.
Narcy *et al.* (2014) [15]	• Parabolic flight experiments • HFE-7000 • Sapphire tube of 6 mm diameter and coated with indium tin oxide for uniform heating • G = 120 – 1200 kg/m^2s • p = 1 – 2 bar • $x_{e,in} < 0.8$ • q''_w = 4.5 W/cm^2 • $x_{e,out} < 0.9$	• At low mass velocities, bubbles were larger in μg_e. At the same time, heat transfer coefficients were lower in μg_e due to less frequent bubble nucleation and detachment. • For mass velocities higher than 400 kg/m^2s, gravity level had negligible influence on flow, irrespective of the flow pattern. • Flow pattern regime transition from slug to annular flows occurs at lower qualities in μg_e. • The liquid film in annular flow was much thinner in μg_e than $1g_e$ due to momentum balance of the liquid. Despite this, for saturated boiling and annular flow regime, heat transfer coefficients were similar in both μg_e and $1g_e$ due to the dominance of shear forces, especially for mass velocities of 100 – 400 kg/m^2s.
Konishi *et al.* (2015) [16]	• Parabolic flight experiments • FC-72 • Rectangular channel of 114.6 mm length and 5 × 2.5 mm^2 cross section with one and two narrow walls heated • u_{in} = 0.1 – 1.9 m/s • G = 224.2 – 3347.5 kg/m^2s • $\Delta T_{sub,in}$ = 2.8 – 8.1°C • p_{out} = 118.2 – 148.3 kPa	• The heated wall temperatures are slightly lower in hypergravity and slightly higher in μg_e, implying heat transfer enhancement and degradation in the respective environments. • Similar to Zhang *et al.* [10], a wavy vapor layer was produced at high heat fluxes, and CHF is a result of the liquid-vapor interface being lifted off the wall. • The wavy vapor layer was thicker at higher heat fluxes or smaller mass velocities. • For double-sided heating, the two vapor layers grew thicker and completely merged in the downstream part of the channel. • At similar heat fluxes, heat transfer was higher for double-sided heating than single-sided due to higher vapor production and faster moving bulk fluid.
Zhang *et al.* (2018) [17]	• Drop tower experiments • Air-dissolved FC-72 • Rectangular heater of 40 × 10 mm^2 area placed in a rectangular channel of 12 × 3 mm^2 cross-section	• Heat transfer was slightly enhanced in μg_e than $1g_e$, evident by the lower wall temperature profiles. • Bubbles were larger in μg_e than $1g_e$ due to the absence of buoyancy. • As heat flux increased, even though void fraction increasingly differed between the gravity levels, heat transfer performance was unaffected. • In μg_e, CHF occurred at the downstream end of the heater as soon as void fraction

	• u_{in} = 0.5 m/s • G = 815.7 kg/m^{2}s • $\Delta T_{sub,in} \approx$ 15°C • p = 1 atm • q''_w = 7.2 – 21.3 W/cm^2	became unity. • q''_{CHF} in μg_e was ~78-92% of q''_{CHF} in $1g_e$.
Lebon *et al*. (2019) [18]	• Parabolic flight experiments • HFE-7000 • Sapphire tube of 6 mm diameter, attached with a carbon-nanobud-coated polyethylene terephthalate film • g = -1.8 – 1.8 g_e • G = 40 – 120 kg/m^{2}s • $\Delta T_{sub,in} \approx$ 4, 10°C	• Average heat transfer coefficient typically increased upon increasing mass velocity, heat flux, and absolute gravity level. • At low heat fluxes, heat transfer coefficient in μg_e was lower than for both vertically upward and downward flows in Earth gravity due to reduction in natural convection, bubble slip velocity, and turbulent mixing. • Increasing mass velocity and heat flux suppressed the effects of gravity on heat transfer coefficient due to the respective effects of high flow inertia and annular flow liquid film evaporation. • The only deviation to these trends occurred when, for similar operating conditions, nucleate boiling sustained in μg_e whereas in $1g_e$, the flow transition to single-phase due to deactivation of nucleation sites.
Iceri *et al*. (2020) [19]	• Parabolic flight experiments • FC-72 • Aluminum tube of 3.75 mm diameter • G = 133 – 428 kg/m^{2}s • $p_{in} \approx$ 160 kPa • $q''_w <$ 106 kW/m^2 • $x_{e,out}$ = -0.25 – 0.65	• In μg_e, the smaller bubbles are circular, and the elongated bubbles have round fronts and flat rears, relative to other gravity levels. This is due to the dominance of surface tension over other forces. • Hypergravity environment yielded the highest heat transfer coefficients for lower mass velocities, saturated boiling conditions, and annular vertical flow, due to thinner liquid films and easier bubble detachment. On the other hand, μg_e had thicker films and the lowest heat transfer coefficients. • The effects of gravity on heat transfer coefficient were negligible for mass velocities higher than 428 kg/m^{2}s or vapor qualities lower than -0.2.
Liu *et al*. (2020) [20]	• Drop tower experiments • FC-72 • Rectangular heaters of 10 mm width and 10, 20, and 40 mm lengths placed in rectangular channels of 12 mm width and 3 and 5 mm heights • u_{in} = 0.5, 1.0 m/s • $\Delta T_{sub,in}$ = 15°C • p = 1 atm	• The focus was on finding a simple method of approximation of q''_{CHF} in μg_e using Earth-gravity experiments. • By comparing the μg_e data to data collected at 0°, 135°, and 315° orientations in Earth gravity for just five cases, q''_{CHF} in μg_e was found to lie within the ranges of q''_{CHF} for 135° and 315° orientations.

To the best of the authors' knowledge, the only flow boiling experiments performed in long durations of μg_e are the present study and a concurrent effort led by researchers collaborating with the Japanese Aerospace eXploration Agency (JAXA). JAXA's experiments studied flow boiling of nPFH through copper and transparent glass heated tubes of inner diameter of 4 mm during 2017 – 2019. Their research objectives are outlined in [34], where the outlined ISS experimental conditions are a heater power supply of 300 W, metal heated tube length of 368 mm, mass velocity of 30 – 400 kg/m^{2}s, inlet subcooling of 0 – 30°C, outlet vapor quality of 0 – 1 and heat fluxes up to 1 MW/m^2. Recent articles from 2021 [35,36] report heat loss estimates for their ISS experimental system, but not actual flow boiling data. The actual experimental conditions reported include a pressure of ~0.1 MPa, mass velocity of 30 – 600 kg/m^{2}s, maximum inlet subcooling of 30°C, maximum outlet quality of 0.5, and heat flux of 0 – 30 kW/m^2 (except for CHF experiments) [35].

In 2023, researchers associated with the Institute of Fluid Mechanics of Toulouse and Airbus Defense and Space in Friedrichshaffen, Germany, and supported by ESA published an article [37] detailing an experimental setup design called CoSmo (compact small scale convection loop) for implementation on the ISS. The main objectives are to study the effects of gravity on flow patterns and heat transfer of nPFH flow boiling in a copper heated tube and borosilicate glass adiabatic tubing of diameter of 6 mm. However, compared to the present study, the parameter ranges attainable with CoSmo are smaller and different (mass velocity of 20 – 150 kg/m^{2}s, pressure of 0.5 – 1.5 bar, subcooling of 0 – 10 K).

At the time of drafting this article and to the best of the authors' knowledge, data from other flow boiling experiments in long duration, highly stable microgravity conditions are non-existent in the open literature.

1.3 Flow Boiling and Condensation Experiment (FBCE)

Since 2011, researchers at PU-BTPFL and the NASA Glenn Research Center (GRC) have been collaborating to study the effects of external gravitational field on several aspects of flow boiling and flow condensation. This massive research endeavor, termed the *Flow Boiling and Condensation Experiment* (*FBCE*), was initiated with an ultimate goal to build a facility to perform both flow boiling and flow condensation experiments on the ISS and collect long-duration μg_e data. FBCE is one of the most complex fluid physics experiments developed by NASA for two-phase flow and phase transition research.

During the initial years of FBCE, several preliminary experiments of flow boiling were performed at different flow orientations in Earth gravity (*e.g.*, [2]), and onboard parabolic flights which established short durations of μg_e [10,16]. The results of these experiments along with

further analyses and practical experience provided the team with the necessary expertise to design and build a final FBCE experimental system and determine its safe operating procedure. Prior to launching to the ISS, the final FBCE system underwent Mission Sequence Testing (MST) in early 2021, which was a set of flow boiling experiments conducted in the vertical upflow orientation in Earth gravity. The MST experiments were performed for a subset of the experimental matrix planned for the ISS, with an emphasis on testing the extremes of the parameter ranges, and their success and detailed results were recently published in [38–40]. Furthermore, the MST experimental runs were performed with flight software. Following the MST, large databases were formed by consolidating datapoints from all preliminary FBCE experiments. Based on these consolidated databases that spanned broad ranges of operating parameters, heating configurations, and gravitational fields, new correlations were developed for both subcooled flow boiling heat transfer in [41] and critical heat flux (CHF) in [42].

In August 2021, the FBCE system with the Flow Boiling Module (FBM) was carefully packaged into several transport containers and launched to the ISS on NG-16 mission. FBCE was later installed by astronauts into the Fluid Integrated Rack (FIR) on the ISS, after which it successfully passed several safety checks. From February 2022 to July 2022, a multitude of flow boiling experiments were performed and a large database was amassed, which covered broad ranges of operating parameters and heating configurations, with a goal to satisfy several research objectives.

The authors' first publication using the ISS data [24] reported the experimental results for flow boiling in a rectangular channel with subcooled inlet conditions and only one of the four walls heated. Single-sided heating helped understand the undisturbed evolution of the bubble boundary and vapor layers produced at the one heated wall as they thicken and fill the entire channel height. The effects of various parameters on heat transfer and interfacial flow physics were analyzed and conclusively established for μg_e environments.

1.4 Objectives of Study

This study is aimed at presenting the experimental flow visualization and heat transfer results of μg_e flow boiling with subcooled inlet conditions, but with two opposite walls heated. Double-sided heating is more complex than single-sided but helps understand the interactions between the vapor produced at both walls, changing the flow physics and potentially heat transfer along the channel length. Note that heating more than two walls would hamper flow visualization and is hence not considered. Flow patterns and temporal flow sequences are presented. Local velocities of vapor bubbles and interfaces are measured from flow sequences and compared with the respective volumetric bulk velocities to reveal the acceleration due to vapor production alone

(and not buoyancy). Operating conditions with two-phase flow instabilities are briefly discussed along with flow image sequences and temporal plots of mass flow rate and pressure. Heat transfer results are presented in the form of flow boiling curves, streamwise profiles of wall temperature and heat transfer coefficient, and parametric trends of both local and average heat transfer coefficient. Parametric effects of mass velocity, inlet subcooling, and inlet pressure on all presented results are elucidated. Heat transfer results are followed by a detailed comparison between single- and double-sided heating of rectangular channel with subcooled inlet, to assess the effects of heating configuration on both flow and heat transfer characteristics in μg_e.

Note that detailed analyses of CHF for μg_e flow boiling with subcooled inlet and both single- and double-sided heating (*i.e.*, just CHF for experimental conditions reported in [24] and the present study) including parametric trends of q''_{CHF} and flow behavior around CHF, non-dimensional group relationships, comparison with $1g_e$ data, and assessments of the predictive capabilities of seminal correlations and the *interfacial lift-off model* are covered in a separate study [43].

2. Experimental Methods

n-Perfluorohexane (nPFH, C_6F_{14}) is selected as the working fluid for its remarkable potential for thermal management in space missions [44]. For the most detailed version of experimental methods, the reader is referred to the authors' prior study [24].

2.1 Two-Phase Flow Loop

A schematic diagram of the FBCE's two-phase flow loop, showing all components paramount for the present flow boiling experiments, is illustrated in Fig. 1. The flow loop is responsible for both conditioning the nPFH to a state desired at the inlet of the Flow Boiling Module (FBM, the test module in this study) and to ensure safe experimentation. The paramount components include a pump, flow meter, filter, preheater, FBM, condenser, and static mixer connected in series in a closed loop. The internal gear pump moves the fluid through the loop, the Coriolis flow meter measures the mass flow rate and provides feedback to the pump through a mass flow controller, and the filter removes any possible impurities from the nPFH. A set of two relief valves are fitted across the ends of the pump for safety purposes, and they crack open if the pressure differential exceeds a certain value (199.95 and 206.84 kPa for the two valves) and permit liquid to flow from the high-pressure end to the low-pressure end. The preheater (termed the Bulk Heater Module, BHM) is equipped with a set of DC-powered cartridge heaters, and it heats up the subcooled liquid nPFH to the temperature desired for experimental inlet conditions to be established at the FBM inlet. The BHM is instrumented with thermocouples and Resistance

Temperature Detectors (RTDs) to provide feedback to shut the heaters down if either the BHM heating surface exceeds 130°C or the fluid temperature at the BHM outlet exceeds 100°C. The FBM further heats the fluid to an even hotter liquid or boils it to a two-phase mixture. The condenser is an nPFH-to-water stainless-steel tube-in-tube heat exchanger with a spiral-finned inner tube, and using cooling water from the ISS, it cools down the nPFH to a subcooled liquid state. The static mixer passively mixes the subcooled nPFH to ensure it is a subcooled liquid before it enters the pump.

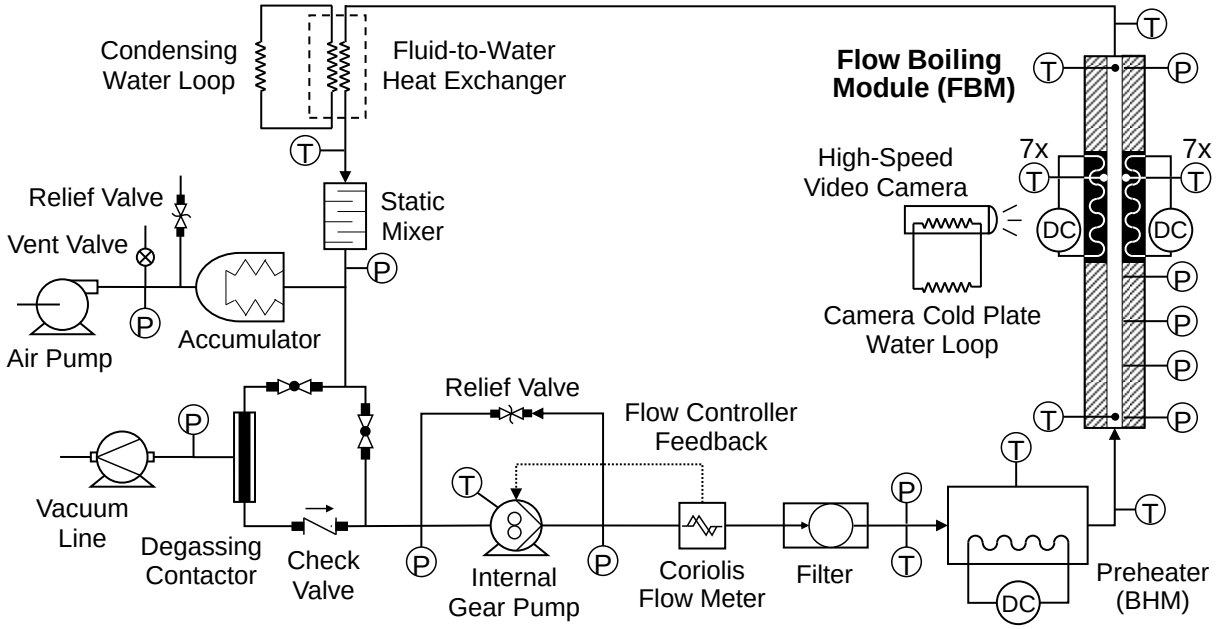

Fig. 1 Schematic diagram of FBCE's two-phase flow loop showing the components paramount for flow boiling experiments. Adapted from the authors' prior article [24].

An accumulator is connected to a T-junction immediately downstream of the static mixer, and it both maintains a constant desired pressure at the inlet to the FBM's heated section and helps avoid/dampen two-phase instabilities in the loop and within the FBM [45]. Stainless-steel bellows divide the accumulator's internal volume into two, one of which is occupied by nPFH and the other by pressurized air. The air side is equipped with an air pump, vent valve, and relief valve (which cracks open when the pressure differential between the air line and ISS environment exceeds 137.90 kPa). When boiling occurs and vapor is produced within the FBM, the accumulator's bellows lower to collect fluid from the flow loop into the accumulator. The accumulator bellows' travel/movement is monotonically related to the amount of vapor within the flow loop; for a particular set of inlet conditions, increasing the FBM heat flux monotonically lowers the bellows.

A degassing contactor is connected in parallel to the main loop between the accumulator's T-junction and the pump. A semi-permeable membrane divides the contactor's interior into two,

with nPFH flowing on one side at a low flow rate and vacuum applied to the other; this vacuum removes non-condensable gases dissolved in the nPFH. During regular experiments, the contactor is fully bypassed.

2.2 Practical Construction of FBCE's Experimental System

All the flow loop components already discussed, along with ancillary components and systems, are packaged into modular boxes as shown in Fig. 2. The six FBCE modules are:

(i) Bulk Heater Module (BHM),
(ii) Fluids System Module – Upper,
(iii) Fluids System Module – Lower,
(iv) Remote Data Acquisition Module 1 (RDAQM1),
(v) Remote Data Acquisition Module 2 (RDAQM2), and
(vi) Test Module Assembly, which denotes the FBM used in this study.

After delivery to the ISS, astronauts lay out these FBCE modules on the Optics Bench of the FIR and then, after assembly, rotate the Optics Bench to vertical upward orientation inside the FIR. The ISS Thermal Control System provides cooling water through the FIR's Water Interface Panel, and the ISS Vacuum Exhaust System provides vacuum for FBCE.

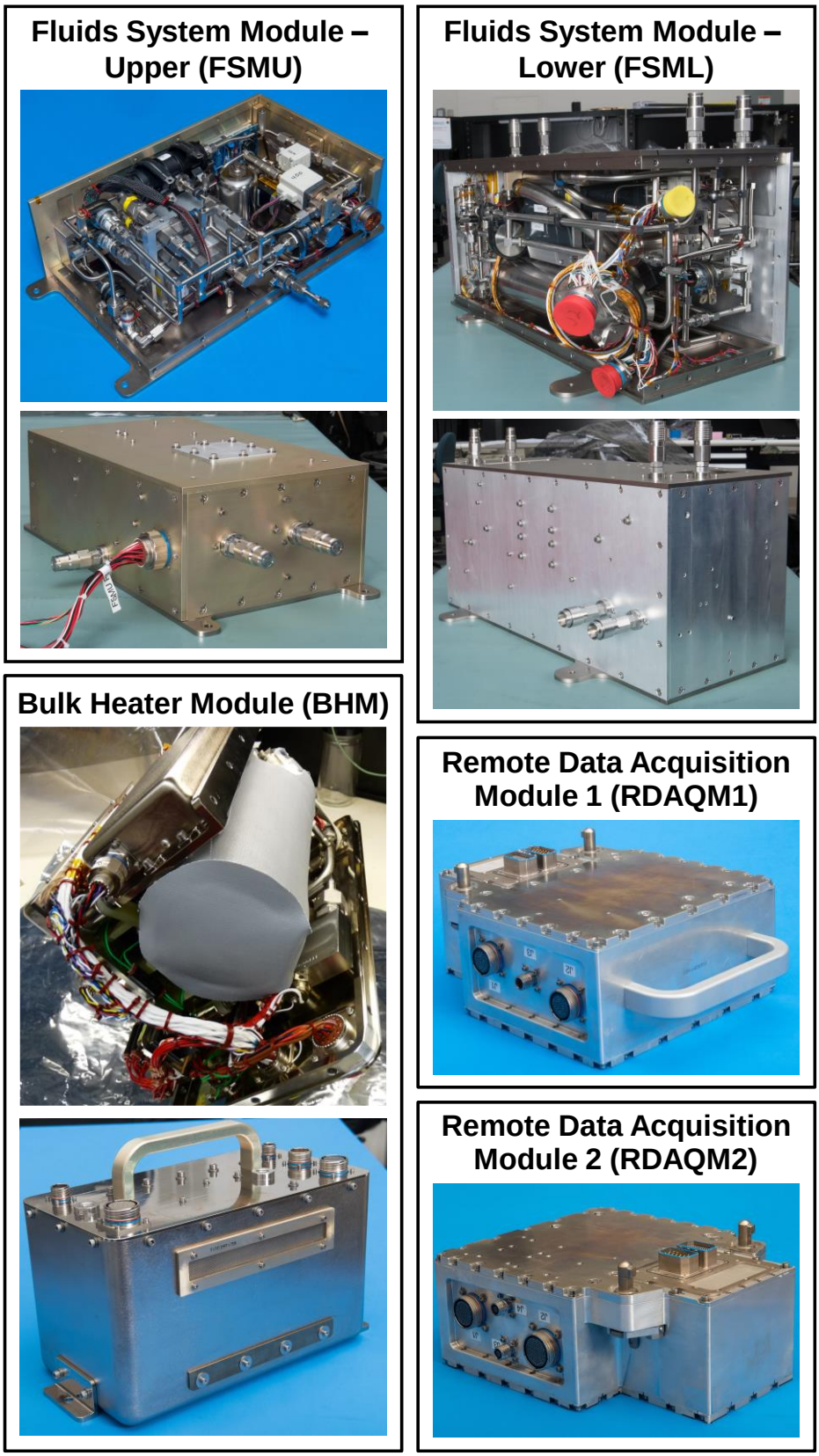

Fig. 2 Photographs of FBCE hardware before and after final packaging into discrete modules. The modules are assembled on the ISS to construct the flow loop shown in the schematics in Fig. 1.

2.3 Flow Boiling Module

Sectional schematics of the FBM's overall construction and a photograph of the final fabricated FBM are included in Figs. 3(a) and (b), respectively. Schematics of construction of heating strips and designation of heated walls and local wall temperatures are included in Figs. 3(c) and (d), respectively. As shown in Fig. 3(a), the FBM is comprised of three Zelux-W polycarbonate plates of thicknesses 25.15, 5.0, and 25.15 mm (in order), clamped together between two aluminum-7075 support plates of thickness of 13.72 mm (anodized black to reduce stray light reflections for imaging purposes). A rectangular slot of 5.0 mm depth and 2.5 mm width is milled into the middle polycarbonate plate to form the flow channel of hydraulic diameter, D_h = 3.33 mm. Two thin slots are milled on either side of the flow channel to each house an oxygen-free copper heating strip of 114.6 mm length, 15.5 mm width, and 1.04 mm thickness (see Fig. 3(c)). All solid-solid interfaces within the FBM are made leak proof by using O-rings. Note that the heating strips are wider than the flow channel so they can be effectively embedded within the polycarbonate plates and then sealed using O-rings.

As shown in Fig. 3(a), the flow channel itself can be demarcated into three lengths: an upstream development length of 327.7 mm, middle heated length of 114.6 mm, and downstream exit length of 60.7 mm. The development length, along with an aluminum 5052 honeycomb insert of thickness of 12.19 mm affixed within it close to the inlet, help break down any large eddies and straighten out flow streamlines. The flow enters and exits the FBM perpendicular to the flow within, but this negligibly affects the heated length due to the development and exit length design.

As shown in Fig. 3(c), each heating strip has a flat heating surface, and the required heat is provided by a set of six thick-film resistive heaters soldered in series within a milled-out portion on the opposite side, so that the distance between the heaters and the heated wall is 0.56 mm. Both the copper strips and the heaters are thoroughly cleaned with 190 proof propanol before soldering, so contact resistance between the heater and copper strip is negligible. Each heater is 16.4 mm long, 4.5 mm wide, and 0.56 mm thick, and consists of an Al_2O_3 substrate upon which a 188 Ω resistive layer is stretched between two solder pads. A minuscule 0.9 mm gap is provided between each successive heater to enable thermocouple access to the strip. For a uniform heat flux distribution, the resistance of all heaters is ensured to be equal, and electrical wiring is done in parallel. A maximum DC power of 175 W can be supplied independently to each heating strip. This heating-strip design has proven to allow fast temperature response and reliable and accurate CHF measurement [10,16]. The copper surfaces have a surface roughness of 20 to 63 Ra.

Key dimensions of the FBM are summarized in Table 2.

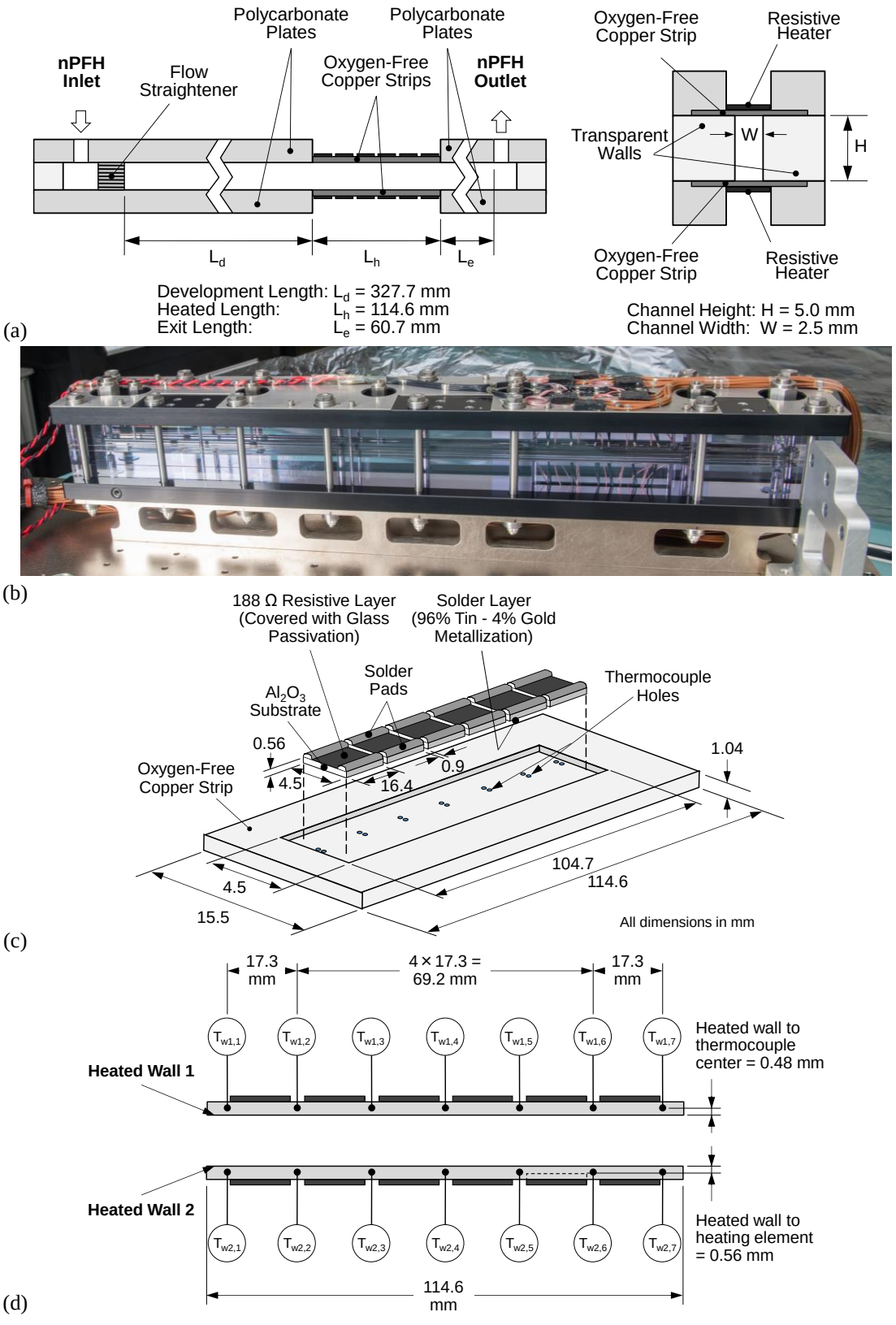

Fig. 3 (a) Sectional schematics of Flow Boiling Module (FBM). (b) Photograph of final assembled FBM. (c) Construction of heating strips. (d) Designation of heated walls and local wall temperatures. Adapted from the authors' prior article [24].

Table 2 Key dimensions of test module (FBM).

Upstream development length, L_d	327.7 mm
Heated length, L_h	114.6 mm
Downstream exit length, L_e	60.7 mm
Thermocouple locations (7) from heated section start, z_{tc}	5.4, 22.7, 40.0, 57.3, 74.6, 91.9, 109.2 mm
Channel height (unheated), H	5.0 mm
Channel width (heated), W	2.5 mm

2.4 Camera System and Flow Visualization

The inherent transparency of the polycarbonate plates, complemented by thorough vapor polishing, enables excellent visual access to the flow channel. A high-speed video camera is pointed at one of the two unheated channel walls (5.0 mm), while the opposite wall is backlit with blue light emitting diodes (LEDs) through a light-shaping diffuser fitted with an intermediate Teflon sheet (this is necessary to address the extremely short transmission distance). High-speed-video images are continuously captured for all heat increments, including CHF, but only the latest 1 s period is recorded for each steady heat increment and the latest 7 s period prior to heater shutdown is recorded for the CHF increment. Before including in this paper, all recorded images are uniformly post-processed to make the liquid-vapor interfaces visually distinct.

Some technical specifications of the high-speed video camera are as follows: lens specification of F#0.95/25 mm, image resolution of 2040×164 pixels, high frame rate of 2000 frames per second, low exposure time of 10 μs, image sensor of the Complementary Metal Oxide Semiconductor (CMOS) type, square pixel size of 5.5 μm × 5.5 μm, and CMOS sensor fill factor of 100%. The camera system yields a spatial resolution of at least ~90 μm (measured via spatial resolution tests conducted using the Ronchi ruling; the camera read ~180 μm using the line-pair-per-mm criteria at 50% dynamic range, which is equivalent to ~90 μm spatial resolution per Rayleigh criteria). Thermal management of the camera system is made possible by a dedicated cold plate receiving cooling water from the ISS Thermal Control System.

An additional analog camera, operating at around 30 frames per second and outputting an analog (RS-170) gray scale video signal, is used to view the heated section and monitor the experiments live.

2.5 Instrumentation and Measurement Accuracy

Local pressures and temperatures are measured at several locations in the FBCE flow loop by a combination of absolute pressure transducers and thermocouples and RTDs (some are shown

in Fig. 1). Local pressures are measured within the FBM via absolute pressure transducers connected at five locations, of which one each is next to the inlet and outlet and three are at intermediary locations within the FBM's development length. The pressure measurements immediately upstream and downstream of the FBM's heated length are denoted as p_{in} and p_{out}, respectively. The bulk fluid temperature at the FBM's inlet and outlet are measured using type-E thermocouples and are respectively denoted as T_{in} and T_{out}. Local temperatures of each of the FBM' heating strips are measured using seven type-E thermocouples with their tips placed in shallow hemispherical indentations made into the strips, such that the conduction distance between heating surface and thermocouple tip center is 0.48 mm. Note that another set of seven type-E thermocouples is provided to each copper strip in a similar fashion, and this is part of a hardware safety circuitry used to shut the heaters down in case any local temperature exceeds 132°C.

Mass flow rate of nPFH is measured using the Coriolis flow meter. The output signals from all sensors are collected within the two data acquisition systems (RDAQM1 and RDAQM2) for continuous temporal measurement. Voltages and currents of DC power supplied to each heating strip are internally measured within the second data acquisition system, RDAQM2. Data is recorded at a sampling rate of 5 Hz during active experimentation and 1 Hz whenever the FBCE system is turned on. The entire FBCE system, including both the data acquisition systems (RDAQM1 and RDAQM2), are controlled using in-house FBCE flight software. The maximum uncertainties in the measurements of these important parameters are reported in Table 3.

Table 3 Measurement uncertainties.

Measured Parameters	**Maximum Uncertainty**
Temperature (thermocouples)	±0.5°C
Temperature (RTDs)	±0.5°C
Pressure	±0.7 kPa
FBM heater power	±0.3% reading
Preheater power	±0.6% reading
Mass flow rate	±0.6% reading

2.6 Experiment Test Matrix

A summary of ISS experiments for double-sided heating with subcooled inlet is presented in Table 4, with the experiment reference numbers indicated for each case. The naming convection followed is the latter three digits of a 4-digit number denote the actual predetermined case number and the first digit denotes the trial/repetition number (for instance, Expt.# 3001 means the third trial of case 1, and Expt.# 21 means the very first trial of case 21). The Expt.# are included in all

subsequent figures corresponding to the data included in them, so that readers can later cross-reference to the databases, which will be openly posted to a NASA repository at a future date.

The experiments reported in this study are loosely demarcated based on their inlet subcooling, and termed highly subcooled inlet when roughly $\Delta T_{sub,in} > 10^{\circ}$C and near-saturated inlet when roughly $0 < \Delta T_{sub,in} \leq 10^{\circ}$C.

Table 4 Summary of ISS experiments for subcooled inlet with double-sided heating.

Experiment Reference Number (Expt.#)	G [kg/m^{2}s]	p_{in} [kPa]	$\Delta T_{sub,in}$ [$^{\circ}$C]
3001	199.93	138.34	6.02
2002	319.94	138.71	5.51
2003	479.96	139.98	5.74
4004	639.95	139.86	5.67
2005	799.96	142.30	5.84
2006	1279.93	136.83	5.17
2007	1599.94	139.75	5.18
2008	2079.93	141.12	6.54
5009	2400.00	138.44	5.76
2010	3199.96	143.22	7.37
2011	199.96	154.52	5.88
2012	319.95	156.27	7.66
2013	479.98	159.56	5.21
3014	639.94	161.33	5.91
2015	799.94	160.23	4.82
2016	1279.94	162.22	5.41
2017	1599.93	160.19	5.67
2018	2079.93	162.27	6.23
2019	2399.99	159.52	5.72
2020	2695.96	159.82	5.69
21	199.94	133.60	15.65
22	319.93	134.51	15.43
23	799.98	132.38	14.91
24	1279.93	130.95	14.78
25	1599.93	130.37	14.40
26	2399.99	129.34	13.44
27	3199.96	126.17	12.69
28	199.94	154.11	16.20
29	319.94	157.32	13.63
30	799.98	154.78	13.37

31	1279.95	155.22	13.29
3032	1599.93	151.86	14.82
3033	2399.99	149.56	14.00
4034	3199.95	147.67	13.92
3035	199.98	133.57	31.34
3036	319.95	131.13	29.17
3037	801.48	131.66	29.69
2038	1279.92	131.47	29.54
3039	1599.78	129.55	28.76
2040	2399.99	127.13	27.60
2041	3199.96	125.70	27.49
3042	199.96	151.35	28.90
2043	319.91	149.48	30.48
3044	801.19	151.28	29.53
2045	1279.95	151.34	29.53
2046	1599.83	152.28	29.22
4047	2399.97	150.30	28.40
4048	3199.96	147.53	27.69
201	200.32	148.61	43.89
202	200.10	149.29	39.66
203	200.16	149.39	33.04
204	200.01	151.43	24.68
205	199.96	152.53	19.70
206	199.94	154.49	10.33
207	199.95	155.54	9.26
3208	199.95	150.14	11.07
209	200.03	158.33	0.36
210	803.52	150.38	44.67
211	800.62	150.41	38.99
212	801.13	151.29	34.41
213	800.03	150.18	24.48
214	800.05	150.32	19.78
3215	799.99	155.70	10.28
216	799.97	154.93	8.85
2217	799.95	155.36	7.28
2218	799.96	158.09	3.68
219	2399.99	149.64	44.65
220	2399.99	148.18	38.52
221	2399.99	150.89	33.78
222	2399.97	147.73	24.30
2223	2399.98	149.23	19.28

2224	2399.99	150.57	10.06
225	2399.99	151.05	8.33
226	2399.99	155.80	7.13
227	2399.99	165.01	5.32
255	320.02	156.20	2.83
256	480.00	156.79	4.14
257	639.92	158.69	2.92
258	1279.95	165.23	3.91
259	1600.05	162.60	4.55
260	2079.93	168.52	5.43
261	2695.96	164.37	4.37

2.7 Experiment Procedure

After the FBCE system was installed onboard the ISS's FIR, the present experiments were remotely executed by personnel at the Telescience Center (TSC) of GRC with no astronaut involvement. The experiments were monitored in real time via a low-data-rate stream transmitted back to the personnel at GRC's TSC, but the large numerical and photography data files were transmitted at regular dedicated intervals. The entirety of the FBM experiments took ~5 months to complete, of which the experimental cases presented in this study are a subset.

The nPFH is regularly degassed both for a few hours at the start of each experiment day and up to 12 hours whenever deemed necessary by *degas check* or ONB data. Degas check is performed by comparing the measured pressure at the FBM inlet and the saturation pressure at equilibrium conditions; if the difference is greater than 2 kPa, a consequence of the presence of non-condensable gases in the nPFH, degassing is performed.

To test each experimental case from the predetermined matrix in Table 4, the corresponding FBM inlet conditions (mass velocity, inlet pressure, and inlet subcooling) and other calculated parameters are entered into the software and transmitted to the ISS. The flow loop is given sufficient time to attain steady state conditions. For double-sided heating, DC power is supplied to both heating strips starting from a minimum predetermined power level to CHF. The first 12 heater power increments are loaded into the software (these are roughly estimated based on the MST experiments and other predictive models), and if CHF is not reached by the 12th increment, finer increments of 1.25 W are automatically implemented to accurately capture CHF. Each increment continues for a regular period of 120 – 180 s, which is sufficient to reach steady state for flow boiling [38,40]. For both safety and automation purposes, CHF is said to occur when at least one local heating-strip data-thermocouple temperature reading exceeds 122°C, at which point, the FBCE software executes a software reset of the heater power levels to a minimum. In case the software reset fails and one of the strip safety-circuitry thermocouples detect temperatures

exceeding 132°C, a hardware shutdown of all FBM and BHM heaters is done; however, this never occurred in actual operations.

The last increment in heat flux that triggers CHF is an average of 1.1 W/cm^2, however it was larger for a few cases. Since the exact value of CHF, q''_{CHF}, lies in-between the heat flux increment that last reached steady state and that which caused the 122°C escalation, the average of these two heat fluxes is reported as q''_{CHF} in this paper. The error associated with q''_{CHF} being between the last two heat fluxes is called CHF isolation error and is 0.6 W/cm^2. The uncertainty in reported q''_{CHF} is a combination of the heat flux measurement uncertainty and the CHF isolation error. This is an average of 2.2% for all experimental cases and a maximum of 8.8% (amounting to 4.6 W/cm^2) for a case with an observed q''_{CHF} = 52.1 W/cm^2.

2.8 Temporal Records for a Representative Experimental Case

Fig. 4(a) shows, for a representative experimental case (Expt.# 3035), temporal records of fluid inlet (T_{in}), fluid outlet (T_{out}), and heating-strip (T_{tc}) temperatures for wall heat flux, q''_w, ranging from a minimum up until q''_{CHF}. The temperatures correspond to the left-side axis and the heat fluxes to the right-side axis. For this plot and all following plots in this paper, the exact operating conditions for the presented datapoints are stated within an inset legend in the respective figure as "parameter = average value ± standard deviation". At time t = 0 s, q''_w is increased from a minimum to the first increment value, and after every 120 s, q''_w is incremented further. Note how both the walls almost have the same q''_w at each increment. At t = 0 s, all the temperatures are roughly the same, and soon after the first heat increment is made, the strip temperature increases sharply. For the first two increments, heat transfer is by pure liquid convection, and the strip temperatures never reach a steady state within the 120 s periods.

As soon as the third increment is made, a sharp spike in T_{tc} is observed for both walls due to the superheat required for onset of nucleate boiling (ONB) being larger than the superheat required to sustain boiling, and this is termed as *transient temperature overshoot* or *incipient boiling superheat*. This mechanism can be confirmed from the flow visualization images shown in Fig. 4(b) for time instants t_1 and t_2, which respectively correspond to the last second (when photos were recorded) of the second and third heat increments. The flow within the channel is upwards while microgravity acts in all directions. For clarity, enlarged half-channel-width images are included for the inlet, middle, and outlet of the channel. At t_1, not a single bubble is seen within the channel, but at t_2, bubbles are seen in all three enlarged images, with the bubble sizes and numbers getting larger at the channel downstream, meaning bubbles are nucleating all along the channel. This proves ONB indeed occurs at the third heat increment.

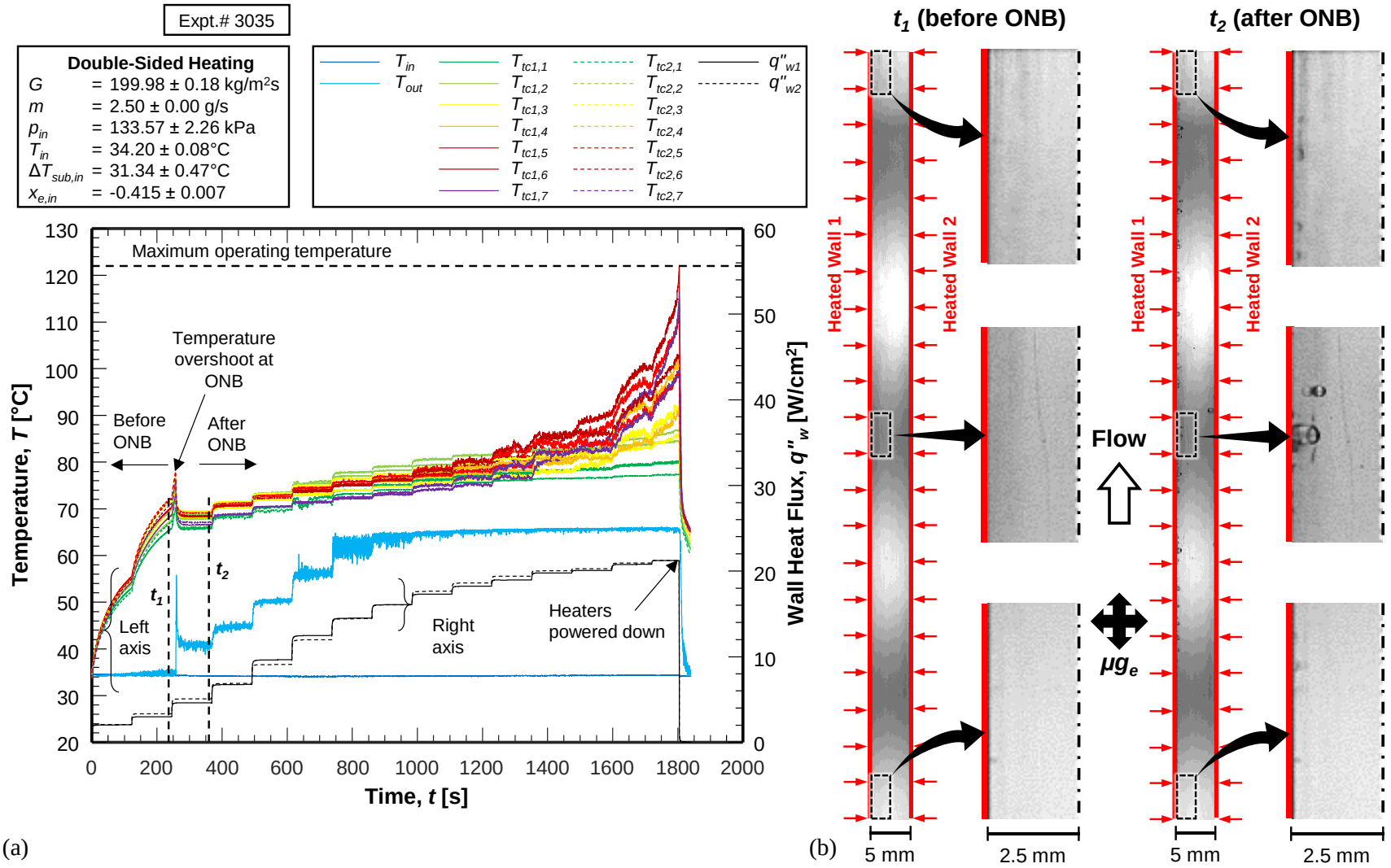

Fig. 4 (a) Temporal records of fluid inlet, fluid outlet, and heated-strip temperatures for heat flux increments from a minimum to CHF for a typical subcooled-inlet experimental case with double-sided heating. The mass velocity is 200 kg/m^{2}s, mass flow rate is 2.50 g/s, inlet pressure is 133.6 kPa, inlet subcooling is 31.3°C, and inlet quality is -0.415. (b) Flow visualization of the entire FBM's heated section (the entire left and right walls are heated as shown in red) at time instants t_1 and t_2 (heat flux increments preceding and succeeding ONB, respectively). Channel width is 5 mm.

The strip temperatures do reach a steady state for all heat increments following ONB. Note how T_{out} increases in steps until about $t \approx 1000$ s, and thereafter remains almost a constant until CHF. This is because the inlet is highly subcooled and as long as only subcooled boiling occurs all along the channel and the fluid is subcooled at the channel exit, T_{out} is determined by a simple energy balance over the channel. But at the point when enough heat is supplied to the fluid to make it saturated at the channel exit, T_{out} is the saturation temperature at p_{out}, which is maintained fairly constant by the accumulator. During the final increment, at $t \approx 1800$ s, all strip temperatures spike upwards and $T_{tc1,6}$ reaches the 122°C safety limit, and all heaters are powered down. Note the nature of the spike, where the temperature curves take a concave-upward shape before it becomes almost vertical; this is a clear indication of CHF.

Overall, these temporal records corroborate that typically (i) all heat flux increments between ONB and CHF attain steady state (only these are reported in this study, and not the earlier increments), and (ii) CHF is the root cause for the 122°C strip-temperature escalation.

2.9 Data Processing and Experimental Ranges

The present experimental data is processed in a very similar way as described in much detail in the authors' prior ISS study [24] and the MST experiments [38], so a briefer description is provided here.

Each steady state datapoint is obtained by averaging the latest 20 s of temporal data of each steady state period. All thermophysical properties of nPFH are obtained from NIST-REFPROP database [46]. The fluid enthalpy at the FBM inlet, h_{in}, is directly obtained using T_{in} and p_{in}, and the enthalpy at the FBM outlet is calculated as

$$h_{out} = h_{in} + \frac{q''_w P_h L_h}{\dot{m}}, \tag{1}$$

which results from an energy balance over the FBM and q''_w is wall heat flux, $\dot{m}$ mass flow rate, and P_h heated perimeter. P_h is equal to channel width, W, for single-sided heating, and $2W$ for double-sided. q''_w is simply calculated as FBM heater power divided by the nPFH heating surface area. This is only possible because the net FBM heat loss is estimated to be negligible compared to the supplied heater power, the physical reasoning for which are as follows. The inherent design of the FBM has copper strips embedded within polycarbonate plates of low thermal conductivity of ~0.2 W/m.K. The underside of the copper strips, where heaters are soldered onto, is exposed to stagnant air of low thermal conductivity as well (note there is no natural convection in microgravity). This means the majority of electrical power supplied to the heaters is conducted through the copper, of high thermal conductivity of 391 W/m.K, into the nPFH within the channel. Moreover, in the early years of FBCE, a detailed heat loss modeling [47] concluded that, for both

single-phase and boiling flows, net heat losses were a maximum of 0.2% of electrical power supplied, which can be considered negligible.

Thermodynamic equilibrium qualities at both the FBM inlet and outlet are determined as

$$x_e = \frac{h - h_f\big|_p}{h_{fg}\big|_p}, \tag{2}$$

where h_f is saturated liquid enthalpy and h_{fg} latent heat of vaporization, both evaluated at local conditions.

As shown in Fig. 3(d), local wall temperatures are designated as $T_{wa,z}$, where *wa* is the heated wall (*w*1 or *w*2) and *z* the streamwise measurement location (1 upstream through 7 downstream). By assuming uniform heat flux and 1-D heat conduction, each measured strip temperature, T_{tc}, is translated into the corresponding T_w using

$$T_w = T_{tc} - \frac{q''_w H_{tc}}{k_s}, \tag{3}$$

where H_{tc} (= 0.48 mm) is conduction distance between the thermocouple center and heating wall, and k_s thermal conductivity of copper. Both local saturation temperature, $T_{sat,z}$, and local thermodynamic equilibrium quality, $x_{e,z}$, at these locations are determined by linear interpolation between values at the inlet and outlet. Per an energy balance, heated single-phase length is estimated as

$$L_{h,sp} = \frac{GA_c}{q''_w P_h}\left(h_f\big|_{p_{in}} - h_{in}\right), \tag{4}$$

where G is mass velocity, A_c channel's cross-sectional area and h_f is estimated at p_{in}. Saturation temperature at the location where $x_e = 0$ (*i.e.*, at the end of $L_{h,sp}$) is estimated by linear interpolation as

$$T_{sat,x=0} = T_{sat}\big|_{p_{in}} + \left(T_{sat}\big|_{p_{out}} - T_{sat}\big|_{p_{in}}\right)\frac{L_{h,sp}}{L_h}. \tag{5}$$

Local bulk fluid temperature is estimated based on the local fluid state as

$$T_{f,z} = \begin{cases} T_{in} + \left(T_{sat,x=0} - T_{in}\right)\dfrac{z}{L_{h,sp}}, & x_{e,z} < 0 \\ T_{sat,z}, & 0 \le x_{e,z} \le 1 \end{cases}. \tag{6}$$

Local heat transfer coefficient is defined as

$$h_{a,z} = \frac{q''_{wa}}{T_{wa,z} - T_{f,z}}. \tag{7}$$

For N_z = 7 streamwise measurement locations, averaged heat transfer coefficient for the entire heated wall is determined by an area-weighted average of local values as

$$\bar{h} = \frac{\sum_{N_z} h_{a,z} A_{h,z}}{A_h} = \frac{\sum_{N_z} h_{a,z} L_{h,z}}{L_h}, \quad (8)$$

where $A_{h,z}$ and $L_{h,z}$ are the heated surface area and length of each unit cell represented by the local value, respectively, and A_h and L_h are the net heated surface area and net heated length, respectively. Averaged wall temperature, $\overline{T_w}$, is also determined in a similar fashion.

A summary of key parameters of the ISS steady-state flow boiling database is included in Table 5 for subcooled inlet with double-sided heating, *i.e.*, the results first reported in this paper. The same for single-sided heating from [24] is included for reference.

Table 5 Summary of key parameters of ISS steady-state database for subcooled inlet with double-sided heating. The same for single-sided [24] is included for reference.

	Double-Sided Heating	**Single-Sided Heating** [24]
Mass velocity, G	199.43 – 3200.01 kg/m^{2}s	199.90 – 3200.13 kg/m^{2}s
Mass flow rate, $\dot{m}$	2.49 – 40.00 g/s	2.50 – 40.00 g/s
Inlet pressure, p_{in}	124.23 – 176.73 kPa	113.30 – 164.29 kPa
Inlet temperature, T_{in}	23.02 – 71.50˚C	23.11 – 70.96˚C
Inlet subcooling, $\Delta T_{sub,in}$	0.20 – 46.00˚C	0.10 – 45.76˚C
Inlet quality, $x_{e,in}$	-0.619 – -0.003	-0.610 – -0.001
Wall heat flux, q''_w	2.06 – 56.37 W/cm^2	2.03 – 56.46 W/cm^2
Outlet pressure, p_{out}	117.08 – 166.32 kPa	114.13 – 159.86 kPa
Outlet temperature, T_{out}	25.06 – 71.82˚C	23.16 – 70.61˚C
Outlet subcooling, $\Delta T_{sub,out}$	0.22 – 43.59˚C	0.30 – 44.87˚C
Outlet quality, $x_{e,out}$	-0.567 – 0.410	-0.593 – 0.149

3. Flow Visualization for Double-Sided Heating

Images of flow visualization of the FBM's heated length are presented in this section for double-sided heating. Two types of images are presented: (i) images capturing the evolution of typical flow patterns along the boiling curve, from after ONB until CHF, and (ii) time-sequential images capturing transient flow characteristics. Images corresponding to a broad range of operating conditions are portrayed to assess the parametric effects of mass velocity, inlet subcooling, and inlet pressure on flow patterns in μg_e. Takeaways from the images provide insight into the flow physics dictating experimental data trends presented in section 4. Listed with each set of images are the average steady-state operating conditions throughout the entire boiling curve. All figures included in this section conform to the schematics of double-sided heating

configuration illustrated in Fig. 5. Flow enters the channel from the bottom and exits at the top with both the left and right walls simultaneously heated. Only the heated section of the FBM is focused upon here, and the entire heated length of the channel (captured in the flow images) is uniformly heated. All reported heat flux percentages are calculated as $q''_w / q''_{CHF} \times 100\%$, where $q''_w = \left(q''_{w1} + q''_{w2}\right)/2$ is heat flux averaged between the two walls and $q''_{CHF} = \left(q''_{CHF1} + q''_{CHF2}\right)/2$ is heat flux averaged between the two walls at CHF; this is done for simplicity as the absolute difference in heat flux between the two walls was an average of 0.19 W/cm^2 with a few cases reaching a maximum of 2.59 W/cm^2.

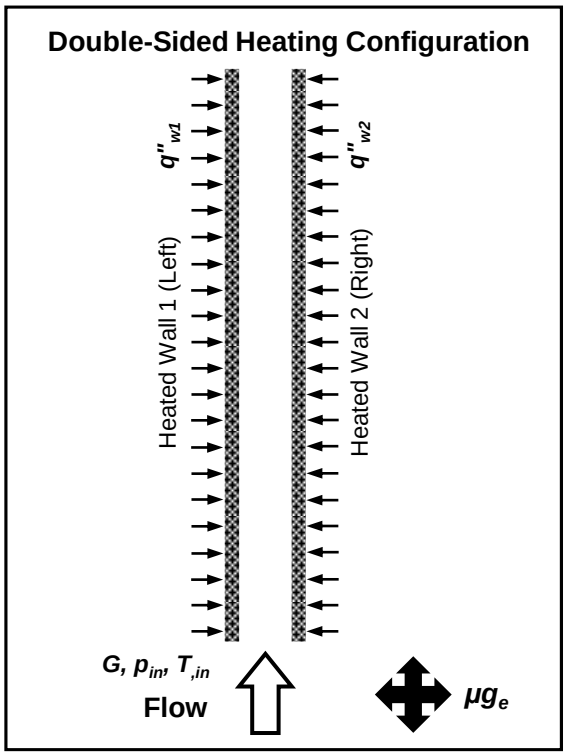

Fig. 5 Schematic representation of double-sided heating configuration. All subsequent flow images pertain to this geometry where only the heated section of the FBM is focused on and the entire length of both walls is heated.

3.1 Flow Patterns Along the Boiling Curve

3.1.1 Flow Patterns for Fixed Moderate Mass Velocity and High Inlet Pressure – Effects of Inlet Subcooling and Heat Flux

Fig. 6 depicts images for several q''_w increments along the boiling curve until CHF at a variety of inlet subcoolings, but with a fixed mass velocity of $G \approx 800$ kg/m^{2}s and double-sided heating.

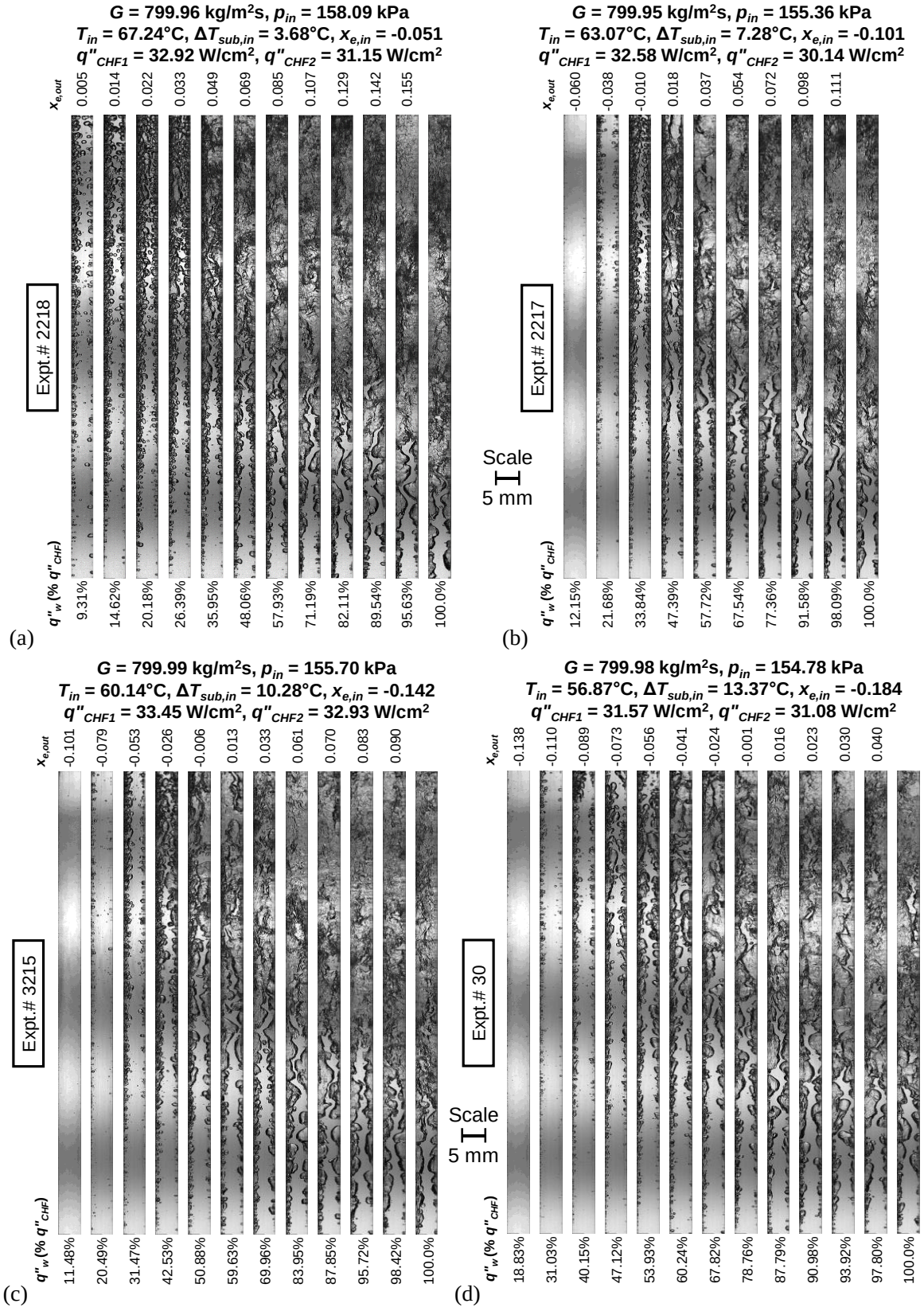

Fig. 6 Flow patterns along the boiling curve until CHF for different inlet subcoolings of $\Delta T_{sub,in}$ = (a) 3.68, (b) 7.28, (c) 10.28, (d) 13.37, (e) 19.78, (f) 29.53, and (g) 38.99°C. Mass velocity is maintained constant at a moderate $G \approx 800.25$ kg/m^{2}s. Inlet pressure is higher at $p_{in} \approx 153.71$ kPa with double-sided heating. Channel width is 5 mm.

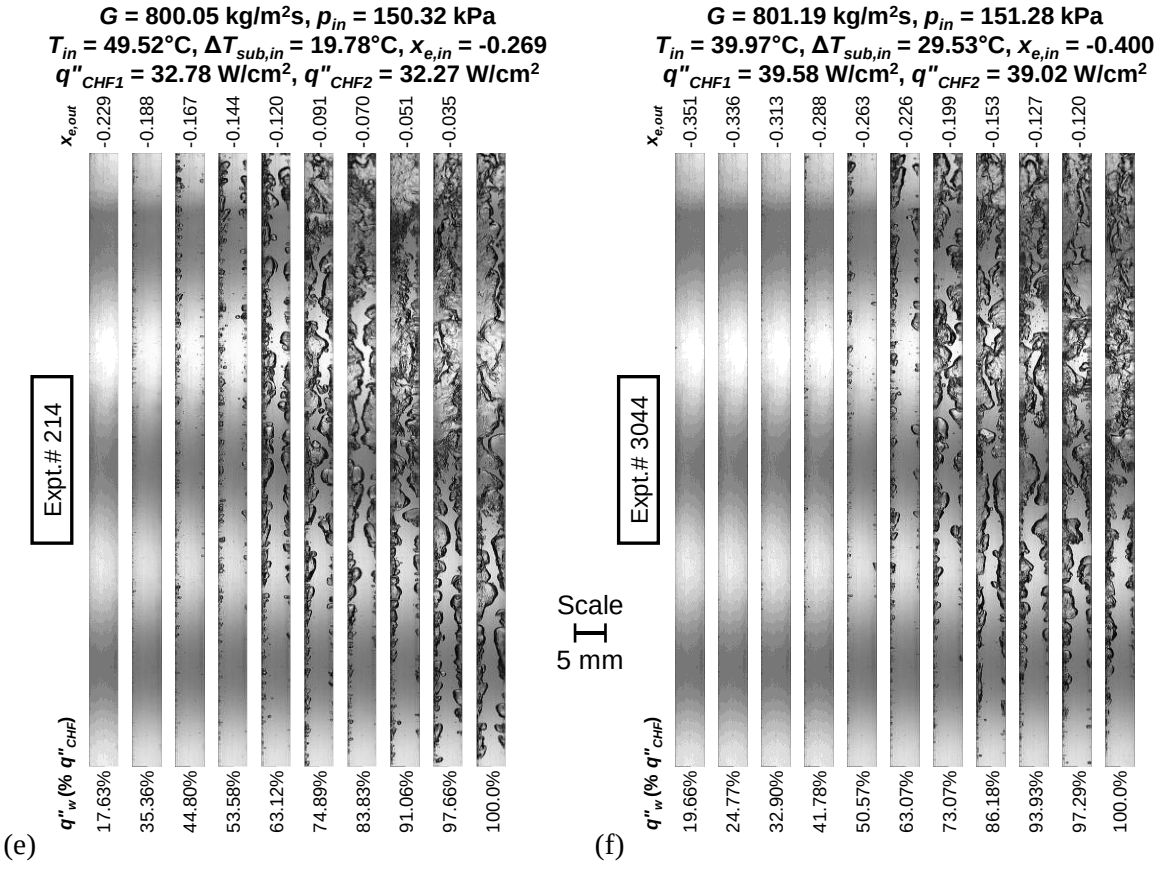

Fig. 6 (continued)

Fig. 6(a) contains images for a low inlet subcooling of $\Delta T_{sub,in}$ = 3.68°C. At q''_w = 9.31% q''_{CHF}, ONB occurs on both walls near the channel inlet. Moving downstream, the nucleated bubbles become larger and crowd the wall as the thermal boundary layer develops and the bulk liquid accumulates heat, lessening its subcooling. However, due to slight differences in heater power between the two walls, the bubble layer on the left wall grows more rapidly than that on the right wall. Increasing q''_w results in a thicker bubble layer that detaches from the wall as additional nucleation sites are activated along the heated walls, promoting bubble growth and coalescence. At 20.18% q''_{CHF}, bubble layers grow thick enough to merge downstream, and bubbles now occupy the entire cross section of the channel. At 35.95% q''_{CHF}, rapid bubble growth and coalescence generate a fairly continuous vapor layer along the heated walls. The liquid-vapor interface is wavy, with the crests characterized by vapor structures protruding from the heated walls, and the troughs by regions of liquid in contact, which allow for nucleate boiling at the wall between vapor patches, called *wetting fronts*. Wetting fronts are a key characteristic of the wavy-vapor-layer regime and provide cooling to the heated wall. In some cases, such as both 35.95 and 48.06% q''_{CHF}, bubble nucleation appears either underneath the vapor layer, within a residual liquid sublayer from the passing of the wetting front, or beside the vapor layer, as it grows radially within the channel. The merged vapor layers downstream now form a liquid-vapor mixture exiting the channel, as opposed to the conglomerate of discrete bubbles observed at lower heat fluxes. Increasing q''_w intensifies boiling within wetting fronts and causes them to lose contact with the heated walls downstream, thickening vapor layers, and advancing the merging point of the vapor layers further upstream. By 89.54% q''_{CHF}, the liquid sublayer is completely evaporated, and the onus of cooling the heated walls is primarily on the wetting fronts. At 100% q''_{CHF}, a single wetting front is observed upstream, and the heated walls are predominantly occupied by vapor. As the wetting front lifts off the heated walls, newly formed wetting fronts remain constrained to the upstream region. The chaotic liquid-vapor mixture carries some liquid to the downstream portion of the channel; however, it is insufficient to cool the heated wall and strip temperatures escalate to 122°C, indicating CHF.

Fig. 6(b) contains images with a slightly higher degree of subcooling, $\Delta T_{sub,in}$ = 7.28°C. ONB occurs at 12.15% q''_{CHF} and small bubbles can be seen sporadically on or close to both heated walls. At 21.68% q''_{CHF}, bubbles increase in size as they slide along the wall and eventually detach, indicating the point of net vapor generation (NVG) and transition to the fully developed boiling (FDB) regime. Increasing the heat flux thickens the bubble layer causing them to merge downstream. At 47.39% q''_{CHF}, the wavy vapor layer begins to develop, and bubble nucleation is still abundant along the wall, even within the vapor layer. Subsequent increases in q''_w push

wetting fronts further upstream until 100% q''_{CHF}, where limited liquid access to the heated walls results in CHF.

Flow patterns for $\Delta T_{sub,in}$ = 10.28°C are featured in Fig. 6(c), and closely resemble those shown in Fig. 6(b). ONB is captured at 11.48% q''_{CHF}, but the bubbles become clearer at 20.49% q''_{CHF}. Bubble nucleation appears more abundant on the left wall due to: (i) minute differences in heater power at the two walls, (ii) slight surface differences creating slightly more favorable nucleation sites, or (iii) a slight tilt of the camera preferentially capturing fine bubbles along the left wall. Fig. 6(d) contains images for $\Delta T_{sub,in}$ = 13.37°C. Vapor layers do not merge until 60.24% q''_{CHF}, after the wavy vapor layer regime has been entered. Increasing $\Delta T_{sub,in}$ increases the condensing capability of the liquid core, impeding bubbles from occupying the center of the channel. At lower $\Delta T_{sub,in}$, merging occurs during the bubbly flow regime as bubble layers grow away from the walls.

The effect of subcooling becomes even more noticeable in Fig. 6(e), $\Delta T_{sub,in}$ = 19.78°C. Temporal strip-temperature records indicate ONB occurred at 17.63% q''_{CHF}, with bubbles not being clearly visible due to the bulk liquid's relatively high subcooling immediately condensing the vapor produced at the heated walls. In the subsequent image, at 35.36% q''_{CHF}, bubble nucleation is observed some distance downstream of a short single-phase liquid region, within which the thermal boundary layer develops, and the liquid temperature rises, allowing for bubble growth. Due to high subcooling, bubbles do not detach from the heated walls and NVG is delayed until the downstream section at 44.80% q''_{CHF}. The wavy vapor layers begin to take shape at 63.12% q''_{CHF} and continue to grow with subsequent increases in q''_{w}. Similar to the previous sub-figures, vapor layers eventually grow thick enough to mesh with each other downstream. However, even at 100% q''_{CHF}, vapor layers do not completely merge, and a distinct vapor layer can be identified for each wall. The interface between the two vapor layers shows how the crests along one wall correspond to troughs along the other and vapor layers mesh together like gear teeth.

Figs. 6(f) and 6(g) show images for relatively high subcoolings of $\Delta T_{sub,in}$ = 29.53 and 38.99°C, respectively. Naturally, the bulk liquid maintains a higher degree of subcooling along the channel length when compared to lower $\Delta T_{sub,in}$, strengthening condensation at the liquid-vapor interface and resulting in thinner vapor layers. In Fig. 6(f), even at CHF, a short upstream region of nucleate boiling precedes the formation of the wavy vapor layer. Increasing $\Delta T_{sub,in}$ stretches the liquid core further downstream. In Fig. 6(g) containing the highest $\Delta T_{sub,in}$, at 100% q''_{CHF}, the liquid core reaches the channel exit, and wetting fronts still exist on both walls in the downstream region. Despite liquid presence, downstream thermocouples still escalate to 122°C, indicating CHF.

3.1.2 Flow Patterns for Fixed Low Inlet Subcooling and High Inlet Pressure – Effects of Mass Velocity and Heat Flux

While Fig. 6 demonstrated the effects of inlet subcooling and heat flux on flow patterns within the channel, Fig. 7 focuses on cases with a fixed low $\Delta T_{sub,in} \approx 5 - 6°C$ but a broad range of mass velocities. The lowest mass velocity of $G \approx 200$ kg/m^{2}s is shown in Fig. 7(a). ONB is captured at 18.25% q''_{CHF}, and nucleation occurs on both heated walls along the entire channel. At 39.34% q''_{CHF}, the bubble layers rapidly grow, and periodically, bubbles grow and overtake the liquid core. The wavy vapor layer begins to develop at 54.07% q''_{CHF}, primarily on the left wall due to a slight imbalance in q''_w at the two walls. In the downstream part of the channel, the wavy vapor layers occupy the entire cross section of the channel. However, the occurrence of additional boiling is observed within or around the wavy vapor layer. At 68.58% q''_{CHF}, the wavy vapor layer has developed on both walls, and the liquid sublayer has evaporated, resulting in a predominantly vapor region downstream in the channel. Further increasing the q''_w advances the wetting fronts upstream and lengthens the vapor dominant region. Within the vapor region, a periodic wave of residual liquid mixed with vapor passes through the channel and provides intermittent cooling downstream. At 100% q''_{CHF}, the predominantly vapor region occupies the majority of the channel, limiting wetting fronts and provoking CHF.

Fig. 7(b) shows images along the boiling curve for $G \approx 480$ kg/m^{2}s. Increasing q''_w both thickens and crowds the near-wall bubble layers, causing them to merge downstream at 24.38% q''_{CHF}. At 46.38% $q''_{CHF,}$ an upstream region of nucleate boiling along the wall is followed by a wavy vapor layer along each wall that merges downstream. The incipient and merging point of the wavy vapor layers move upstream as q''_w is increased, and the wavy vapor layers form at the channel inlet by 87.07% q''_{CHF}. The flow pattern at 100% q''_{CHF} closely resembles that for the lower G shown in Fig. 7(a). Flow patterns along the boiling curve for $G \approx 640$ kg/m^{2}s are shown in Fig. 7(c). ONB is captured at 10.18% q''_{CHF}. Consistent with the previous sub-figures, the wavy vapor layers become more defined upstream and merge earlier as CHF is approached. However, at 100% q''_{CHF}, the liquid core extends deeper into the channel than at lower G.

Images for $G \approx 1280$ and 1600 kg/m^{2}s are shown in Figs. 7(d) and 7(e), respectively. Higher flow rates amplify interfacial shear stress, which thins the vapor layers and delays their merging. After the vapor layers merge, the downstream section of the channel appears more chaotic than at lower G with an abundance of dark ripples due to turbulent mixing of residual liquid with the vapor layers. The highest G of 2400 kg/m^{2}s is shown in Fig. 7(f). Shear forces dominate at relatively low q''_w, preventing vapor layers from growing into each other until near the channel exit at 55.21% q''_{CHF}. Even at 100% q''_{CHF}, a short upstream region featuring distinct single bubbles exists, unlike at lower G where a continuous vapor layer begins at the channel inlet.

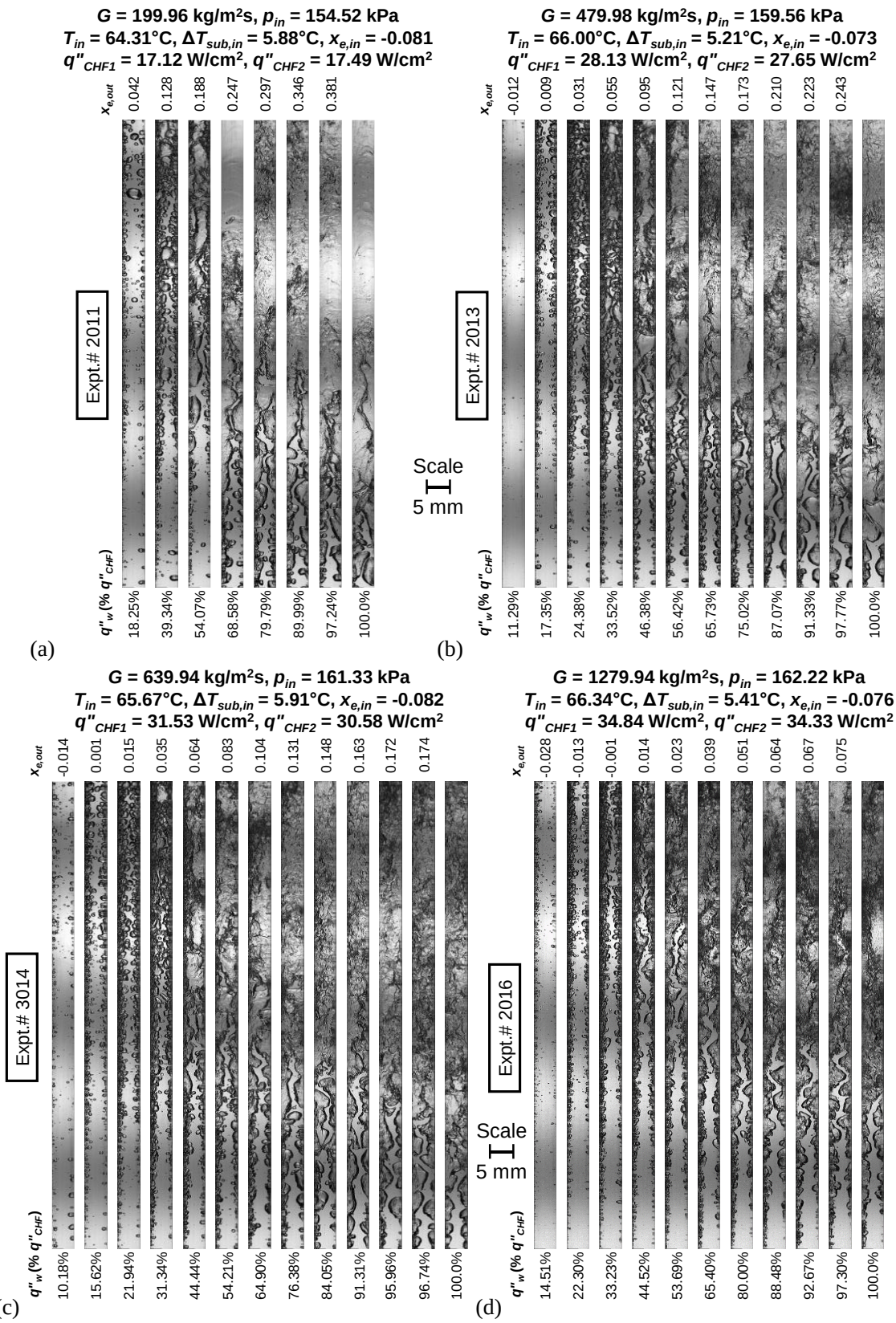

Fig. 7 Flow patterns along the boiling curve until CHF for different mass velocities of G = (a) 199.96, (b) 479.98, (c) 639.94, (d) 1279.94, (e) 1599.93, and (f) 2399.99 kg/m^{2}s. Inlet subcooling is maintained constant for near-saturated inlet at $\Delta T_{sub,in} \simeq$ 5.63°C. Inlet pressure is higher at $p_{in} \approx$ 159.56 kPa with double-sided heating. Channel width is 5 mm.

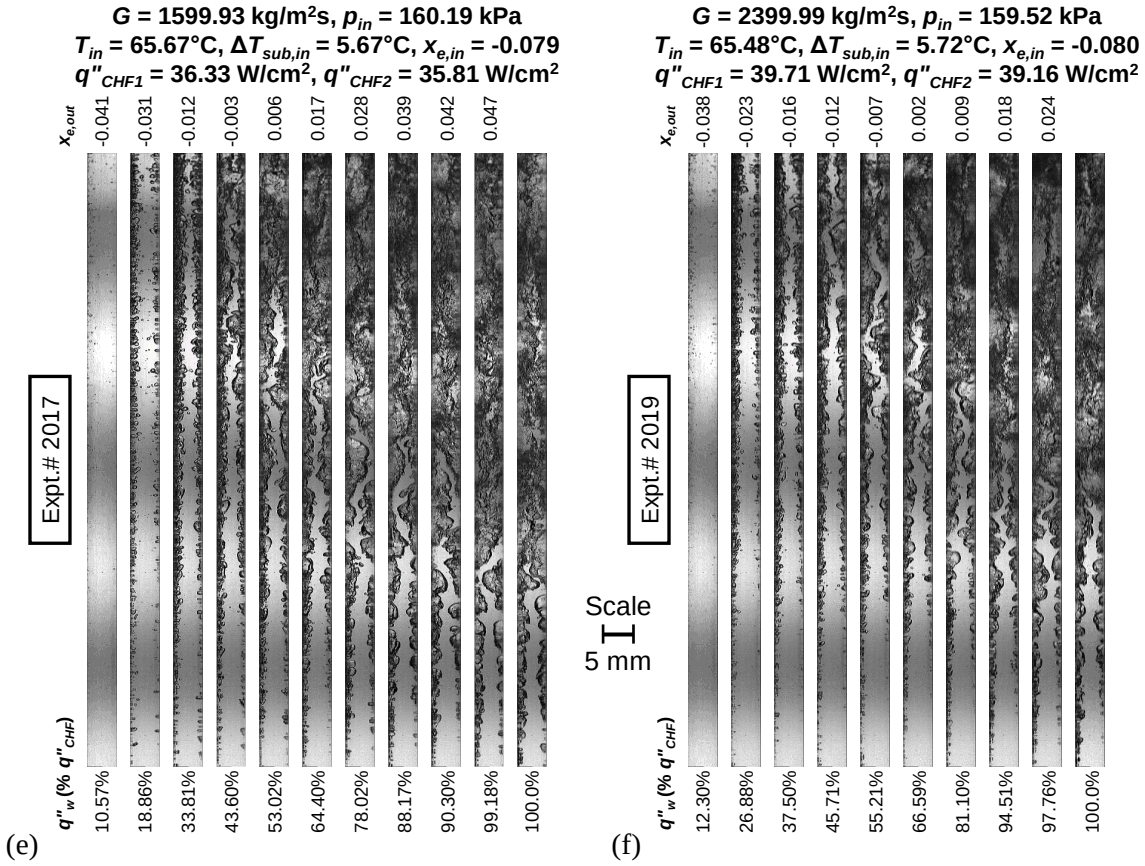

Fig. 7 (continued)

3.1.3 Flow Patterns for Fixed Low Inlet Subcooling and Low Inlet Pressure – Effects of Inlet Pressure

Fig. 8 shows additional images for a near-saturated inlet of $\Delta T_{sub,in} \approx 5 - 6$°C, but with a slightly lower inlet pressure of p_{in} = 136.83 – 142.30 kPa, compared to p_{in} = 154.52 – 162.22 kPa in Fig. 7. The effects of pressure on observed flow patterns are minor compared to that of G and $\Delta T_{sub,in}$ for the current range of operating conditions. For any given G, the images in Fig. 8 closely resemble the corresponding images in Fig. 7, and this is also reflected in their similar q''_{CHF}. For instance, the flow pattern evolution along the boiling curve for the lowest G of 200 kg/m^{2}s (shown in Fig. 8(a)) mimics that experienced in Fig. 7(a). ONB is observed at 17.34% q''_{CHF}, and the bubbly flow regime remains at relatively low q''_w, where bubbles grow, detach from the heated walls, and enter the liquid core. Due to the low degree of subcooling, minimal condensation occurs as bubbles drift through the channel. As heat flux is elevated, the increased wall superheat activates additional nucleation sites promoting bubble growth and coalescence, resulting in a thicker and denser bubble layer along each wall. Wavy vapor layers develop at 51.32% q''_{CHF} and create a predominantly downstream vapor region, once vapor layers merge. Its length grows with

increasing q''_w until 100% q''_{CHF}, where the abundance of vapor in the channel prevents sufficient wetting of the heated walls. Increasing G in subsequent sub-figures, Figs. 8(b-f), parallels the effects it had in Figs. 7(b-f), respectively, thinning the vapor layer and increasing the amount of liquid present downstream.

3.1.4 Flow Patterns for Fixed High Inlet Subcooling and Low Inlet Pressure – Effects of Mass Velocity and Heat Flux

Images along the boiling curve for a higher $\Delta T_{sub,in}$ of 27.60 – 31.34°C are shown in Fig. 9. Fig. 9(a) contains the lowest G of 200 kg/m^{2}s. At 23.05% q''_{CHF}, nucleation occurs sporadically along the heated walls, and bubbles are quickly condensed by the highly subcooled liquid. Both the number of activated nucleation sites and the size of bubbles increase with increasing q''_w, but strong condensation effects still hinder bubble growth. By 58.11% q''_{CHF}, a sufficient amount of heat is added to the working fluid, raising the temperature of the near-wall liquid, so that bubbles grow in the streamwise direction along both heated walls. At 68.76% q''_{CHF}, flow patterns transition to the wavy-vapor-layer regime downstream, where large bubbles periodically form and continue to grow as they slide downstream coalescing with other bubbles. Following the sliding vapor patches are stretches of highly subcooled liquid that suppress significant vapor production. Approaching CHF, at 87.51% q''_{CHF}, vapor layers become more distinct within the channel and merge further upstream. Even at 100% q''_{CHF}, nucleate boiling persists upstream, wherein the highly subcooled fluid entering the channel initially impedes the development of a vapor layer. However, liquid contact with the heated walls and boiling in the upstream section of the channel cannot prevent CHF manifestation in the channel's downstream due to the heated walls being mostly insulated by vapor.

Fig. 9(b) contains images for $G \approx 320$ kg/m^{2}s. Flow patterns at ONB appear similar to the previous sub-figure, where bubbles are prevented from substantial growth due to strong interfacial condensation. Increasing q''_w produces sustainable bubbles at 50.81% q''_{CHF} and initiates the wavy vapor layer downstream at 73.12% q''_{CHF}. The wavy vapor layer develops further upstream with increasing q''_w, and flow patterns both approaching CHF and at CHF are similar to those in Fig. 9(a).

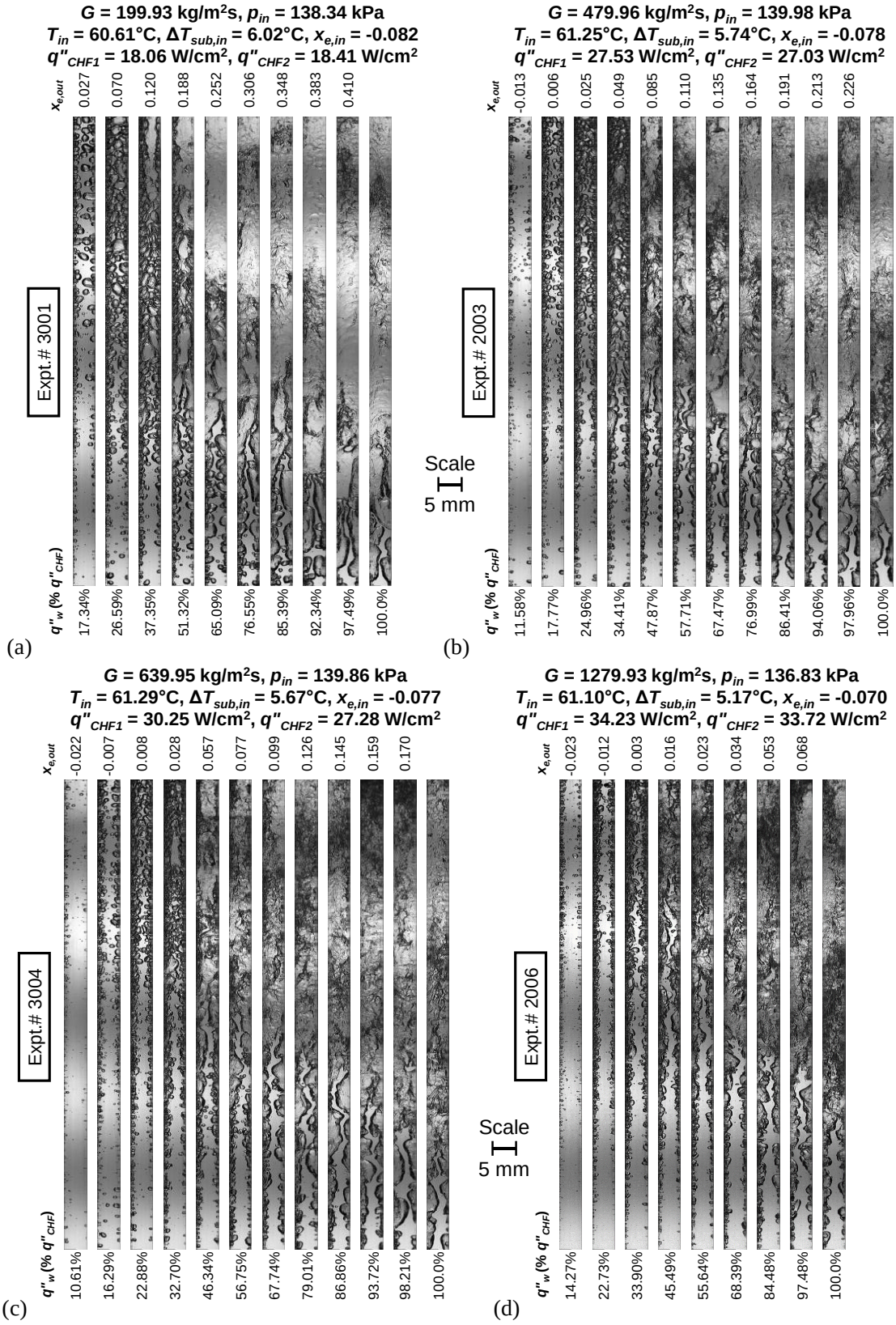

Fig. 8 Flow patterns along the boiling curve until CHF for different mass velocities of G = (a) 199.93, (b) 479.96, (c) 639.95, (d) 1279.93, (e) 1599.94, and (f) 2400.00 kg/m^{2}s. Inlet subcooling is maintained constant for near-saturated inlet at $\Delta T_{sub,in} \approx$ 5.59°C. Inlet pressure is lower at $p_{in} \approx$ 138.87 kPa with double-sided heating. Channel width is 5 mm.

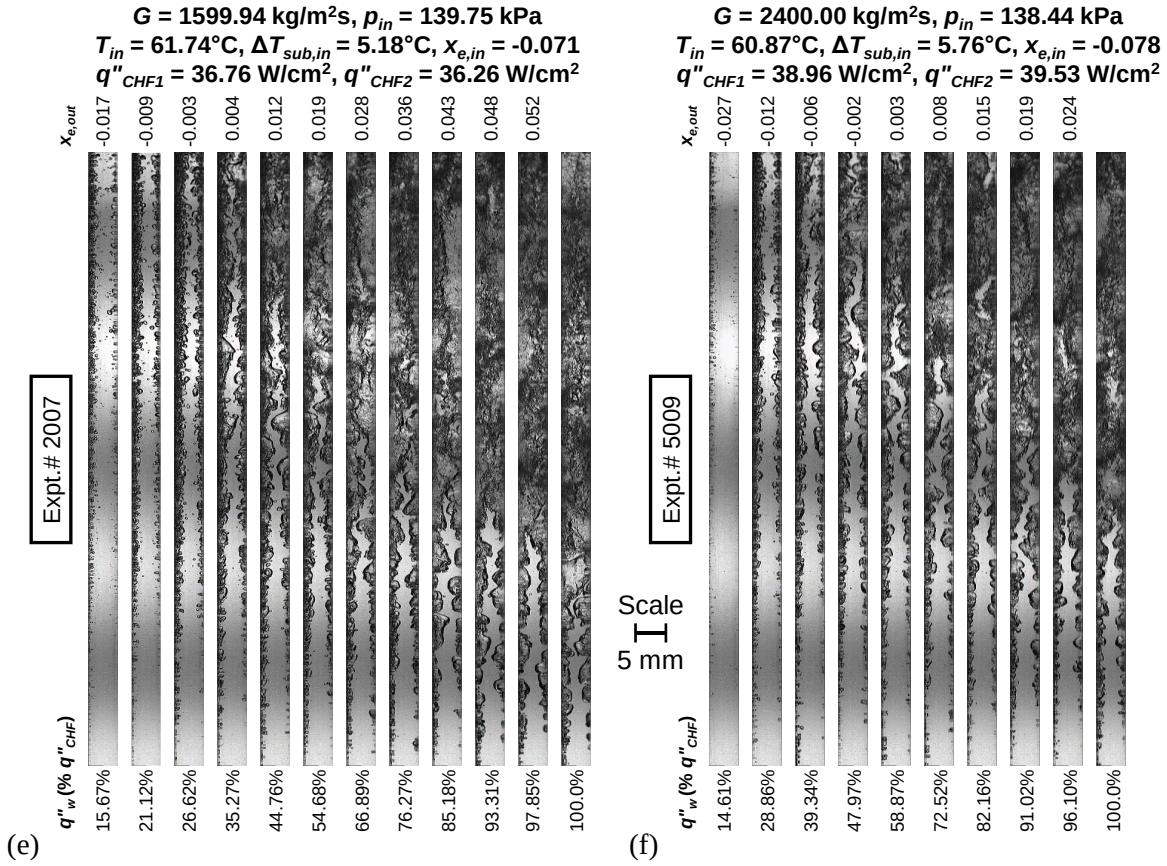

Fig. 8 (continued)

Boiling-curve images for $G \approx 800$ kg/m^{2}s are shown in Fig. 9(c). Temperature-time plots indicate ONB occurred at 16.92% q''_{CHF}, but vapor is immediately condensed at the wall and is not visible in the channel. The amount of vapor within the channel increases with increasing q''_w and, at 72.00% q''_{CHF}, a continuous wavy vapor layer develops along the left wall. The large discrepancy between the two walls is caused by an increased asymmetry between the wall heaters at the present heating increment. The supplied power difference between the walls is approximately 4 W, but by 83.69% q''_{CHF}, the disparity is less than 2 W. Vapor layers no longer merge and mix as they did at lower $\Delta T_{sub,in}$ or lower G, but they may still touch one another. This is attributed to condensation of the liquid-vapor interface away from the heated wall and the increasing interfacial shear at higher flow rates, thinning the vapor layers. As the vapor layers continue to grow with increasing q''_w, the most downstream wetting front is advanced further upstream until insufficient cooling causes CHF at $q''_{CHF} = 37.01$ W/cm^2.

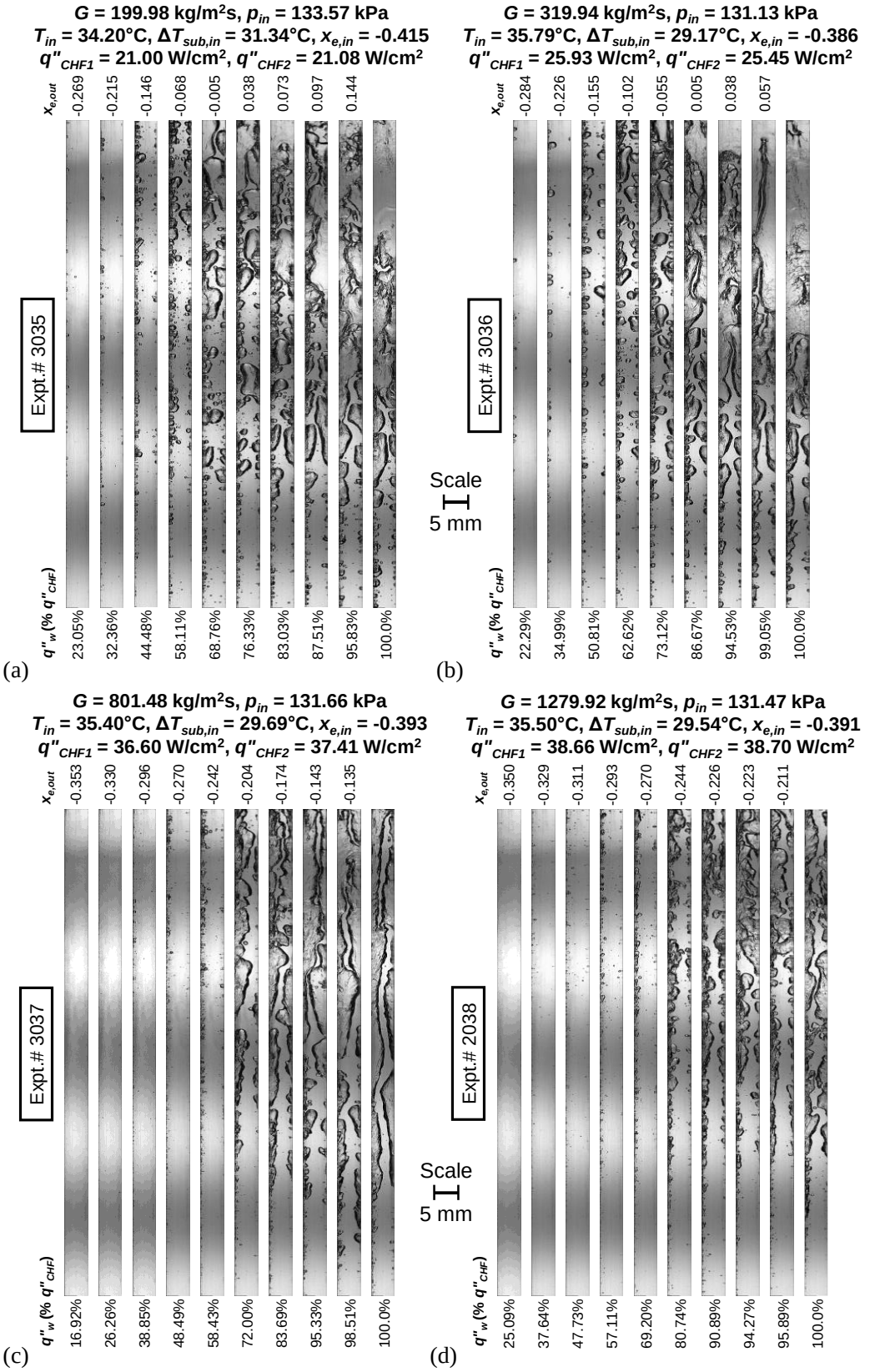

Fig. 9 Flow patterns along the boiling curve until CHF for different mass velocities of G = (a) 199.98, (b) 319.94, (c) 801.48, (d) 1279.92, (e) 1599.78, and (f) 2399.99 kg/m^{2}s. Inlet subcooling is maintained constant for highly subcooled inlet at $\Delta T_{sub,in} \simeq$ 29.35°C. Inlet pressure is lower at $p_{in} \simeq$ 130.75 kPa with double-sided heating. Channel width is 5 mm.

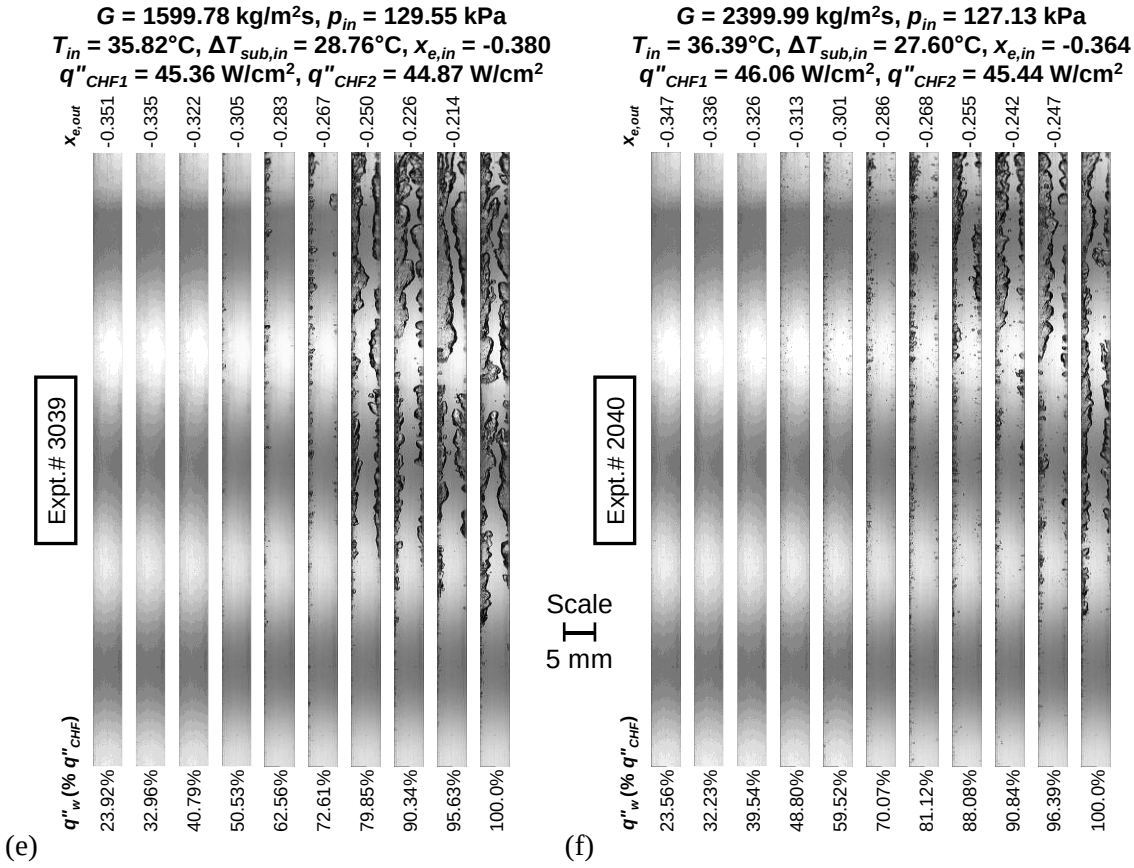

Fig. 9 (continued)

Similar trends are observed in Fig. 9(d) and Fig. 9(e), featuring $G \approx 1280$ and 1600 kg/m^{2}s, respectively. Visible bubble nucleation is suppressed at relatively low q''_w. At CHF, wetting fronts remain in the upstream region of the channel, while vapor layers shield the heated wall from the liquid core, downstream. The highest G of 2400 kg/m^{2}s is shown in Fig. 9(f). The combination of high G and high $\Delta T_{sub,in}$ maximizes condensation effects along the whole channel. Throughout most of the boiling curve, nucleate boiling, while not always visible, occurs sporadically along the heated wall. The presence of vapor in the channel increases and, at 88.08% q''_{CHF}, a vapor layer forms near the channel exit. The vapor layer moves upstream as heat flux increases, but it remains relatively thin. Even at 100% q''_{CHF}, due to the strong influence of shear stress and condensation, a relatively thick liquid core exists downstream.

3.2 Flow Visualization Image Sequences

3.2.1 Image Sequences for Fixed Moderate Mass Velocity and Low Inlet Pressure – Effects of Inlet Subcooling and Heat Flux

Temporal image sequences within the FBM for a moderate mass velocity of $G \approx 800$ kg/m^{2}s and higher inlet pressure of $p_{in} \approx 155$ kPa, but three different inlet subcoolings of $\Delta T_{sub,in}$ = 29.53, 10.28, and 3.68 are respectively shown in Figs. 10-12. In these figures, parts (a) and (b) portray image sequences for heat fluxes of $q''_w \sim 70\%$ and 95% q''_{CHF}, respectively. The time interval between successive images is mentioned below each sequence. Part (c) shows measured local flow velocities of bubbles or complex vapor structures at multiple locations within the channel for the flow in both parts (a) and (b). Each reported velocity denotes the temporal average over the entire image sequence shown in the paper. These velocity measurements make it possible to track flow acceleration through the length of the channel *only* due to vapor production (and not due to gravitational effects).

Fig. 10(a) depicts image sequences, with a spacing of 2.5 ms, for $\Delta T_{sub,in}$ = 29.53°C and q''_w = 73.07% q''_{CHF}. Highly subcooled liquid enters the channel, and sparse nucleation can be seen along the heated walls upstream. Bubbles formed near the channel entrance are condensed by the subcooled liquid, while those produced slightly further downstream grow into the wavy vapor layer. Vapor patches slide along the wall and continue to grow as boiling occurs within wetting fronts, accelerating flow downstream. Closer to CHF, at 92.56% q''_{CHF} shown in Fig. 10(b), the effect of condensation diminishes, and bubbles are better sustained, developing the wavy vapor layer further upstream. While the vapor layers are separated in the upstream region, interaction between the two occurs through the liquid core, resulting in crests of one interface aligning with troughs of the other, roughly resembling the meshing of mechanical gear teeth. Vapor structures grow towards the opposite wall as they traverse the channel and, in some cases, overtake wetting fronts on the opposite wall. Wetting fronts, if unimpeded, accelerate downstream at a quicker rate than at 73.07% q''_{CHF}. As wetting fronts exit the channel, they are replaced by new wetting fronts formed upstream, sustaining wall cooling. Fig. 10(c) shows, at 73.07% q''_{CHF}, bubbles and vapor patches accelerating through the channel with the local velocity almost tripling near the channel exit ($u \sim 1.5$ m/s) compared to that near the channel inlet ($u \sim 0.5$ m/s). This is due to the increased volume of the produced vapor compared to liquid. Note that the volumetric mean flow velocity of subcooled liquid, determined from mass velocity and inlet liquid density, is 0.49 m/s. Flow acceleration is more evident for the higher heat flux of 92.56% q''_{CHF}, where vapor accelerates more rapidly, raising the average velocity of vapor during the image sequence. This is observed tracked vapor all along the length of the channel.

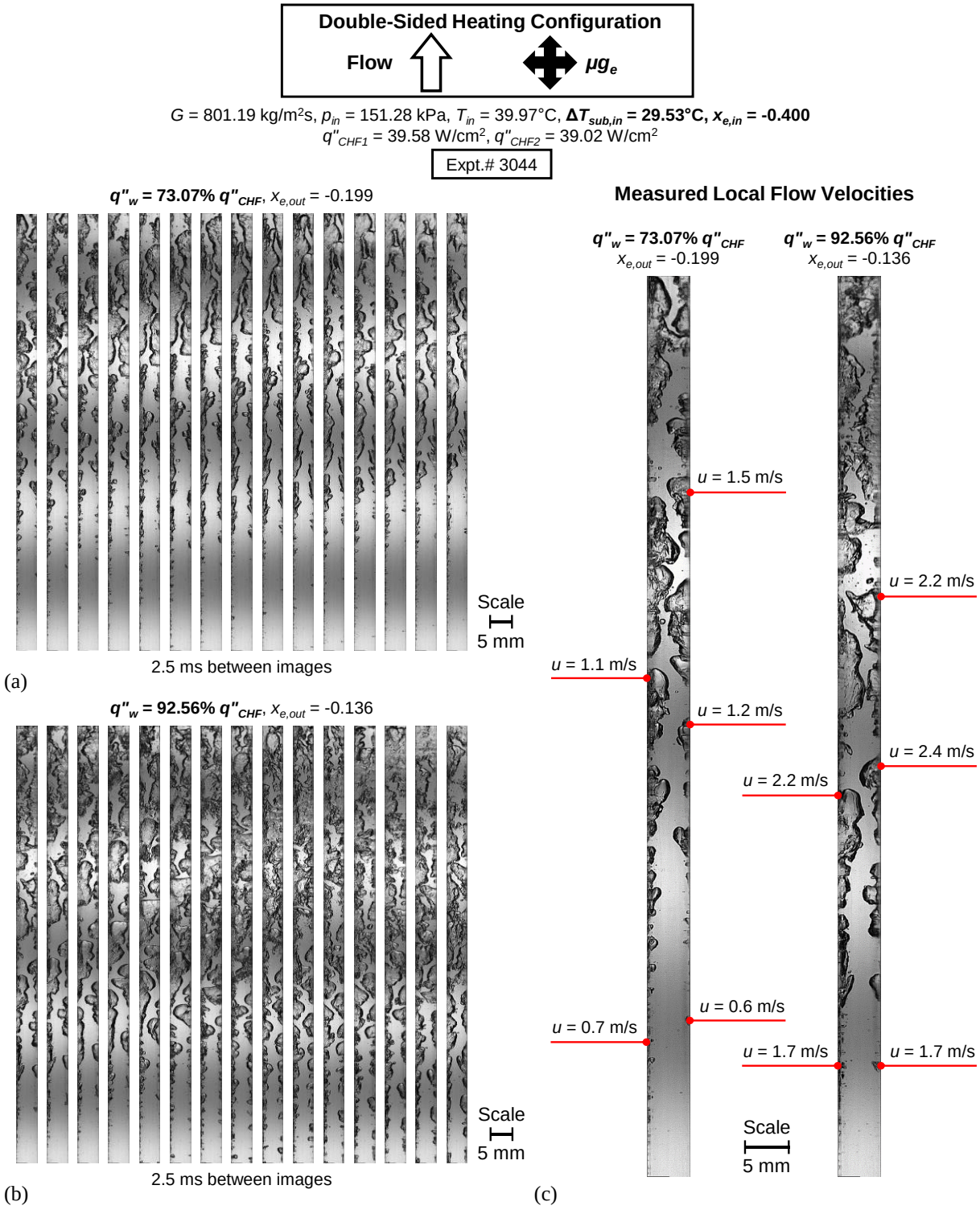

Fig. 10 Flow visualization image sequences for an inlet subcooling of $\Delta T_{sub,in}$ = 29.53°C at a moderate mass velocity of $G \approx$ 801 kg/m^{2}s and higher inlet pressure of $p_{in} \approx$ 151 kPa with double-sided heating at heat fluxes of $q''_w \approx$ (a) 73% and (b) 93% q''_{CHF}. Time interval between successive images is mentioned below each sequence. (c) Measured flow velocities at multiple locations within the channel at these operating conditions. Channel width is 5 mm.

Image sequences with a spacing of 2.5 ms between consecutive images for a lower $\Delta T_{sub,in}$ of 10.28°C are featured in Fig. 11. At 69.96% q''_{CHF} shown in Fig. 11(a), nucleation occurs close to the channel entrance and individual bubbles grow as they slide downstream, unlike the bubbles in Fig. 10(a), which were condensed by highly subcooled liquid. The same bubbles which develop at the entrance in the first image evolve into the most upstream part of wavy vapor layer at the end of the time sequence. Evolution of the downstream region is more chaotic than at higher subcooling. Observing the most downstream wetting front in the first image, as time advances, it lifts off the heated wall and adjacent upstream vapor merges into the abundant downstream vapor. At 95.72% q''_{CHF} shown in Fig. 11(b), vapor produced at the channel entrance quickly grows into the wavy vapor layer and travels downstream. Wetting fronts travel a short distance before lifting off the heated walls, merging with the highly turbulent downstream region. Owing to a lower subcooling, Fig. 11(c) shows the measured velocities at both heat fluxes to be higher than that observed in Fig. 10(c). The other trends in velocity still hold.

Fig. 12 features a near-saturated inlet with $\Delta T_{sub,in}$ = 3.68°C and an interval of 2.5 ms between consecutive images. At 71.19% q''_{CHF} shown in Fig. 12(a), nucleation commences at the entrance, and bubbles rapidly grow to form the wavy vapor layer. Images are similar to those shown in Fig. 11(a), but the vapor layers grow thicker at a faster rate, and wetting fronts are extinguished in the upstream region. Within the chaotic downstream section, distinct alternating lighter higher-quality low-density fronts (LDFs) and darker lower-quality high-density fronts (HDFs) are observed, similar to the MST experiments with two-phase inlet [40]. HDFs transmit residual liquid downstream, providing some cooling to the walls. At an elevated heat flux of 95.63% q''_{CHF} shown in Fig. 12(b), the wavy vapor layer develops quicker, and wetting fronts slide a short distance before being extinguished. Wetting fronts are immediately replaced upstream by newly formed wetting fronts, but the majority of the channel is filled with churn-type liquid-vapor mixture. Greater flow acceleration for the near-saturated inlet in Fig. 12(c) results in the fastest moving vapor compared to higher inlet subcoolings in Figs. 10(c) and 11(c) evident by the attainment of $u \sim 3.0$ m/s just midway along the channel.

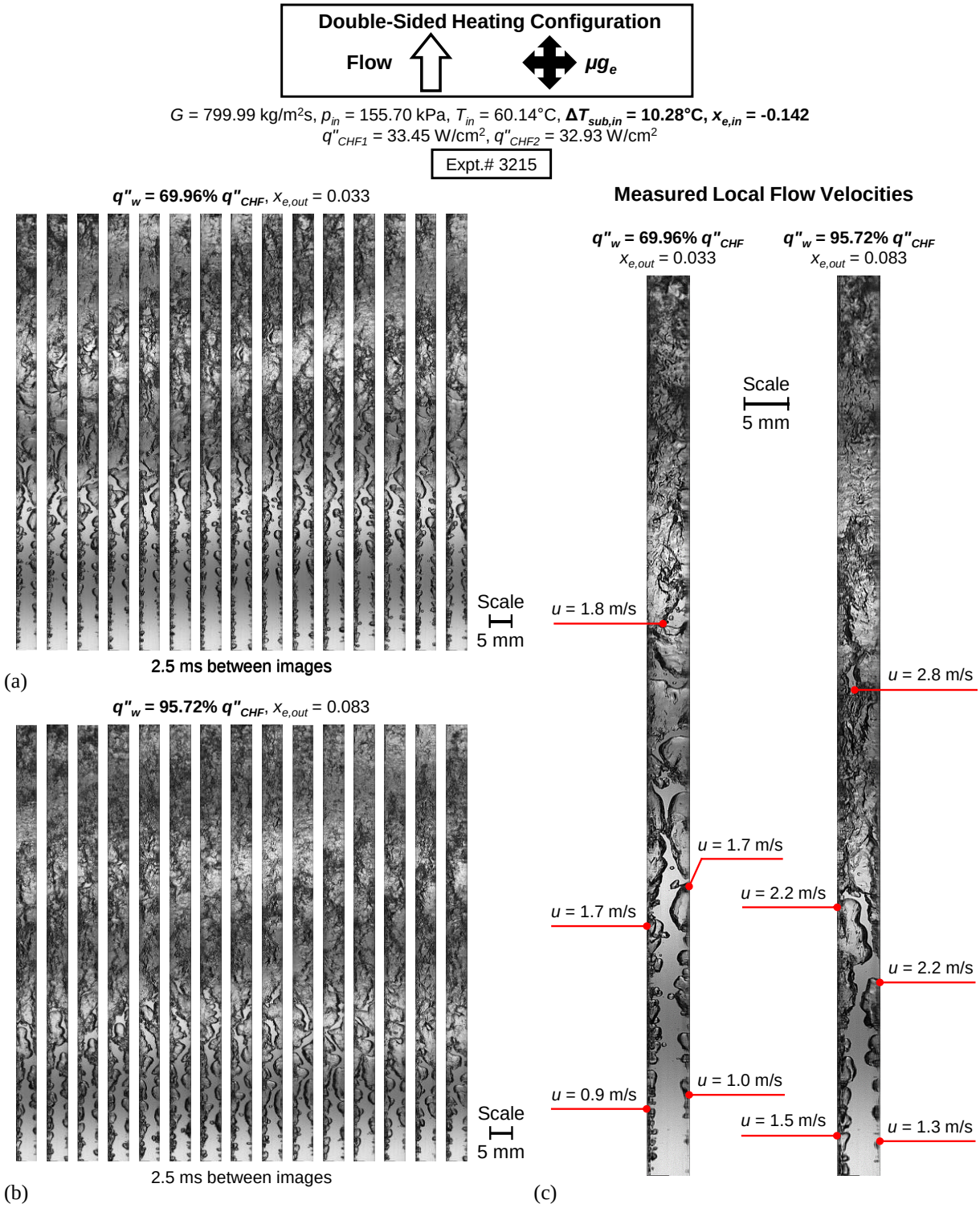

Fig. 11 Flow visualization image sequences for an inlet subcooling of $\Delta T_{sub,in}$ = 10.28°C at a moderate mass velocity of $G \approx$ 800 kg/m²s and higher inlet pressure of $p_{in} \approx$ 156 kPa with double-sided heating at heat fluxes of $q''_w \approx$ (a) 70% and (b) 96% q''_{CHF}. Time interval between successive images is mentioned below each sequence. (c) Measured flow velocities at multiple locations within the channel at these operating conditions. Channel width is 5 mm.

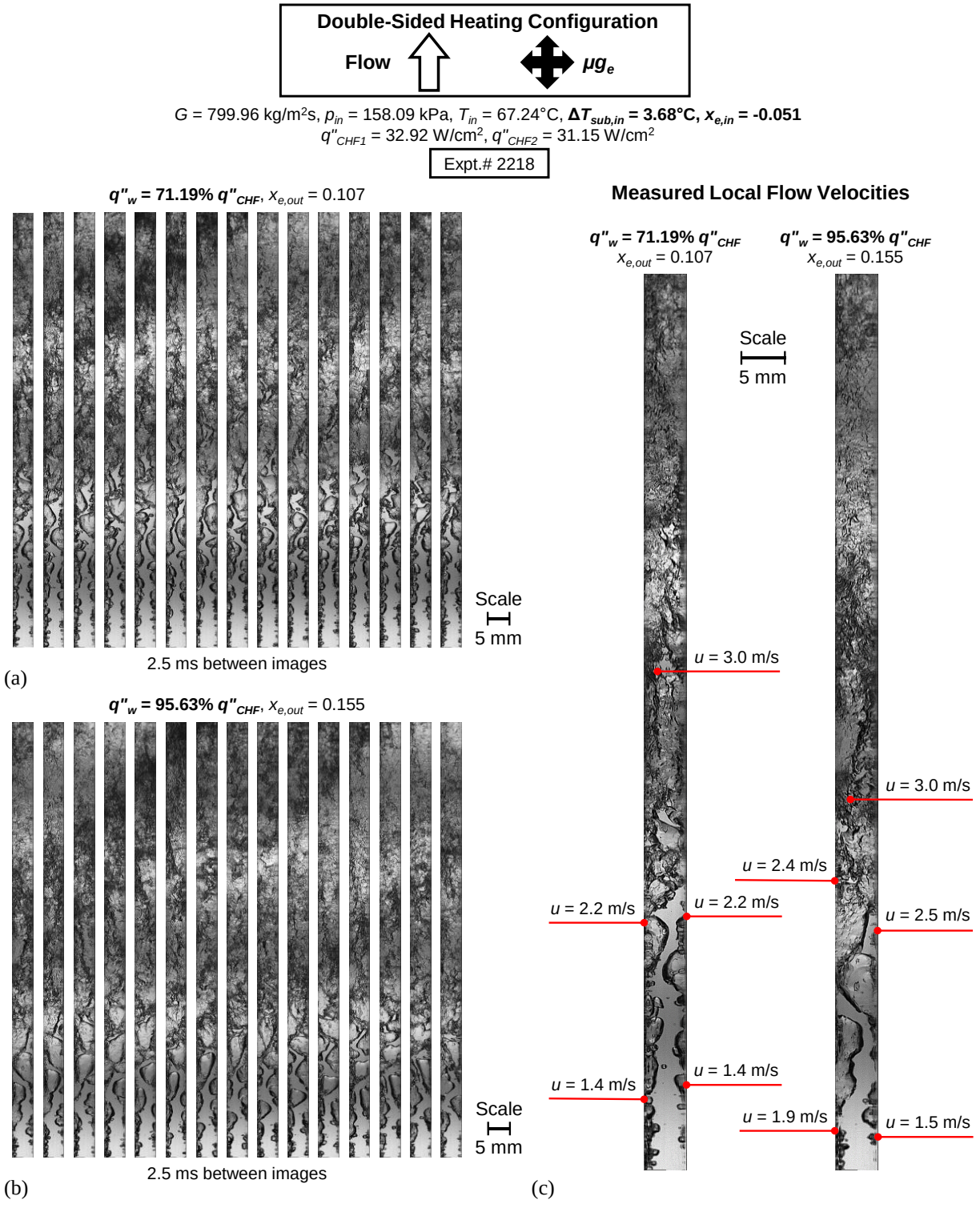

Fig. 12 Flow visualization image sequences for an inlet subcooling of $\Delta T_{sub,in}$ = 3.68°C at a moderate mass velocity of $G \approx 800$ kg/m^{2}s and higher inlet pressure of $p_{in} \approx 158$ kPa with double-sided heating at heat fluxes of $q''_w \approx$ (a) 71% and (b) 96% q''_{CHF}. Time interval between successive images is mentioned below each sequence. (c) Measured flow velocities at multiple locations within the channel at these operating conditions. Channel width is 5 mm.

3.2.2 Image Sequences for Fixed Moderate Inlet Subcooling and Low Inlet Pressure – Effects of Mass Velocity and Heat Flux

Figs. 13-15 show image sequences similar to Figs. 10-12, but for different G with a fixed moderate inlet subcooling of $\Delta T_{sub,in} \approx 14.5°C$ and higher inlet pressure of $p_{in} \approx 153$ kPa. In Fig. 13, containing image sequences with a spacing of 5 ms, liquid enters with the lowest G of 200 kg/m^{2}s. The flow pattern evolution in the upstream section of the channel resembles those in previous image sequences. At low G, the downstream section of the channel is almost completely vapor. This becomes more apparent at the higher q''_w of 95.86% q''_{CHF} shown in Fig. 13(b). However, HDFs are observed passing through the downstream portion of the channel. Their development is captured partway through the channel at 95.86% q''_{CHF}; see how in the first few images, a sliver of the liquid core is pinched off by merging vapor layers. In the latter images, evaporation continues at the liquid-vapor interface, shrinking the isolated liquid. The remaining liquid eventually mixes with the surrounding vapor and disperses throughout the channel cross section. The mixture continues to propagate downstream, continually evaporating.

Fig. 14 shows images with an interval of 2.5 ms and $G \approx 800$ kg/m^{2}s. The operating conditions in Fig. 14 are similar to those shown in Fig. 11, resulting in near-identical evolution of flow patterns. Transient flow patterns in the downstream section are more complex than in the previous sub-figure, Fig. 13. Vapor layers remain relatively thin upstream, causing them to merge further downstream than at lower G. At both heat fluxes, intense boiling occurs within wetting fronts, accelerating them downstream. Eventually, they lift off the wall and mix with the chaotic downstream region. Wetting fronts travel significantly further at 67.82% q''_{CHF} shown in Fig. 14(a), where boiling in the wetting front is relatively tame, compared to 93.92% q''_{CHF} shown in Fig. 14(b).

Image sequences with a spacing of 1.5 ms and a relatively high G of 2400 kg/m^{2}s are presented in Fig. 15. Similar to Figs. 13 and 14, nucleation occurs near the channel entrance at 68.74% q''_{CHF} shown in Fig. 15(a). Bubble growth is initially suppressed, and some bubbles condense as they slide along the wall. After a short distance downstream, bubbles continually grow and coalesce as they slide along the wall, leading to the formation of a wavy vapor layer along each heated wall. The wavy vapor layer is thinner for higher G, due to increased interfacial shear stress thinning the vapor layers. The liquid core is better preserved throughout the channel, and an abundance of wetting fronts propagate out of the channel. Minimal interaction occurs between vapor layers, with some contact in the downstream section where vapor layers are thickest. Increasing q''_w to 95.98% q''_{CHF} (see Fig. 15(b)) reduces the influence of condensation in the upstream section of the channel, and bubbles formed near the channel entrance grow and coalesce, resulting in the wavy vapor layer developing further upstream. Wetting fronts slide

downstream, until they lift off the wall, and vapor layers merge near the channel exit. Wetting fronts propagate further downstream than at lower *G*, delaying CHF.

Increasing *G* from 200 to 800 to 2400 kg/m^{2}s results in the calculated volumetric mean velocity of subcooled liquid entering the channel to increase from 0.13 to 0.51 to 1.51 m/s. The measured flow velocities in Figs. 13(c), 14(c), and 15(c) reveal the respective calculated velocities of vapor near the channel inlet to increase from ~0.1 to ~0.5 to ~1.9 m/s, which loosely matches with the volumetric calculations. As the flow's bulk velocity increases, the velocity of vapor produced within the channel also correspondingly increases. The trends observed for different $\Delta T_{sub,in}$ in the previous set of figures (Figs. 10(c)-12(c)) with respect to heat flux is mirrored here (Figs. 13(c)-15(c)) at different *G*; increasing q''_w increases vapor production and acceleration within the channel, resulting in greater average vapor velocity. As *G* increases, and the amount of vapor within the channel lessens, the relative increase in velocity is lessened. For the lowest flow rate, shown in Fig 13(c), at the higher heat flux of 95.86% q''_{CHF}, vapor production is largest, and the velocity of vapor in the channel's downstream is at least four-fold that in the upstream (1.2 m/s in the downstream compared to 0.3 m/s on the bottom wall upstream). However, at high *G*, the largest velocity increase is 73% and it occurs from 1.9 m/s along the bottom wall upstream to 3.3m/s downstream at 68.74% q''_{CHF}. However, the actual flow velocities are still much greater at high *G* than low *G*.

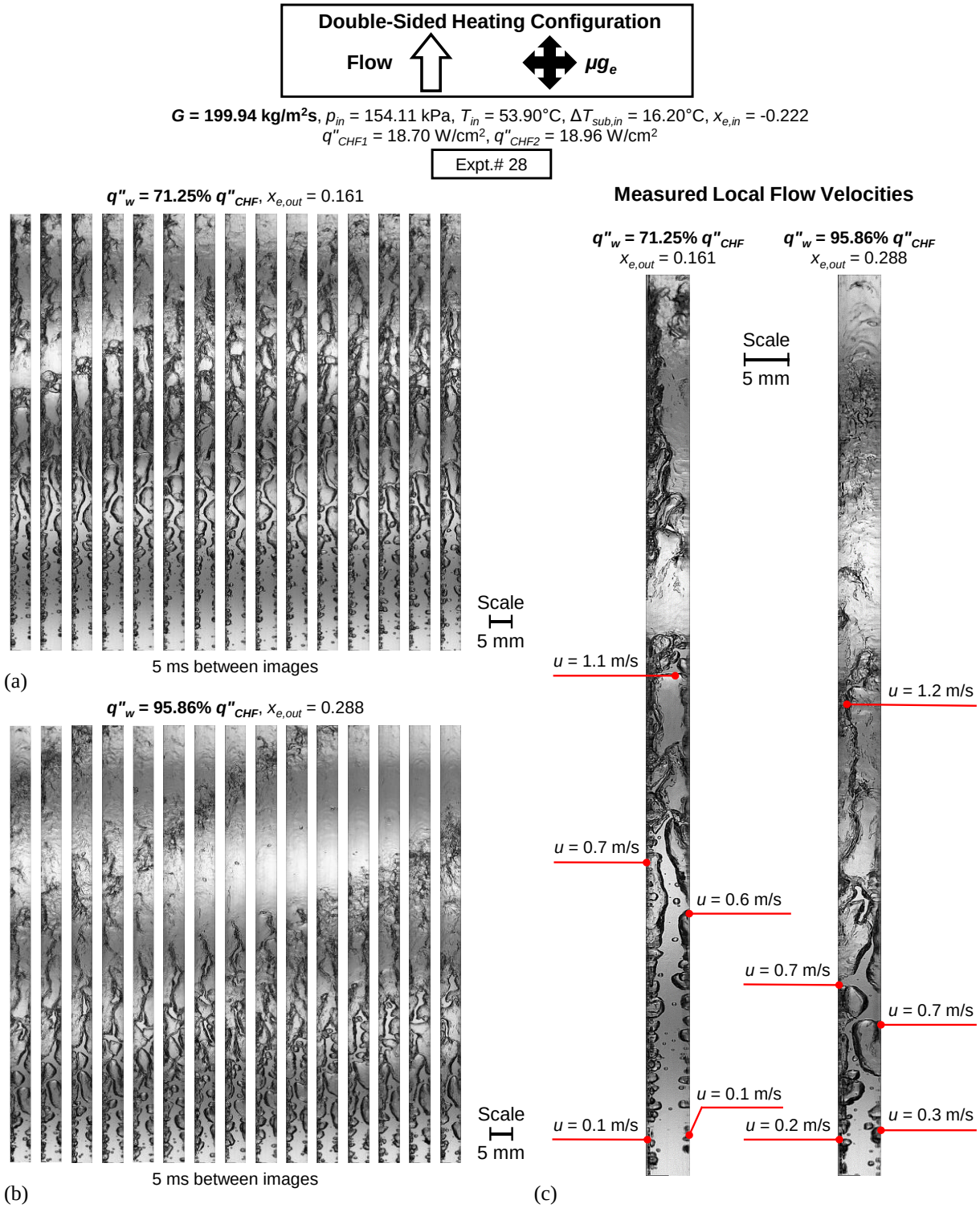

Fig. 13 Flow visualization image sequences for a mass velocity of $G \approx 200$ kg/m^{2}s at a moderate inlet subcooling of $\Delta T_{sub,in} \approx 16.2$°C and higher inlet pressure of $p_{in} \approx 154$ kPa with double-sided heating at heat fluxes of $q''_w \approx$ (a) 71% and (b) 96% q''_{CHF}. Time interval between successive images is mentioned below each sequence. (c) Measured flow velocities at multiple locations within the channel at these operating conditions. Channel width is 5 mm.

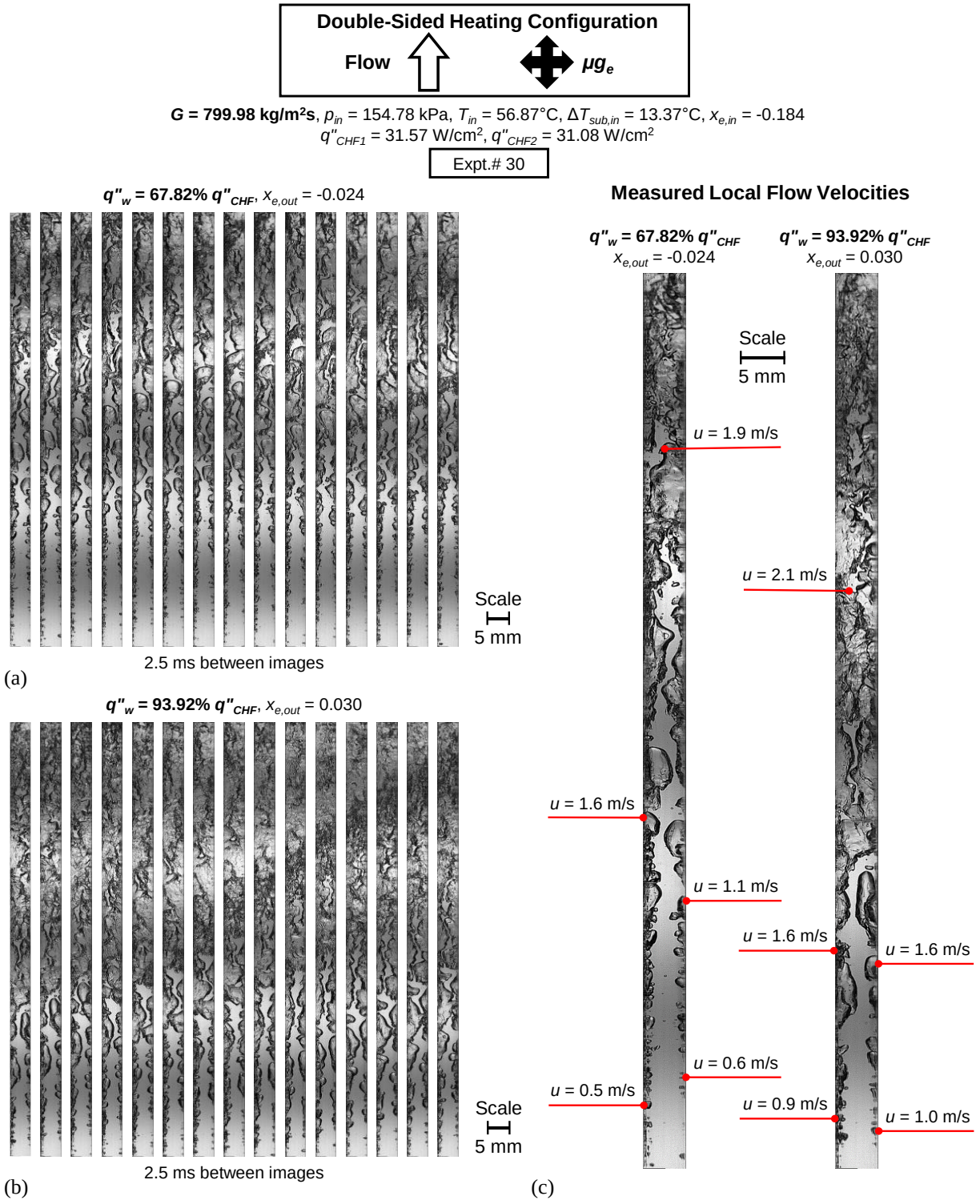

Fig. 14 Flow visualization image sequences for a mass velocity of $G \approx 800$ kg/m^{2}s at a moderate inlet subcooling of $\Delta T_{sub,in} \approx 13.4$°C and higher inlet pressure of $p_{in} \approx 155$ kPa with double-sided heating at heat fluxes of $q''_w \approx$ (a) 68% and (b) 94% q''_{CHF}. Time interval between successive images is mentioned below each sequence. (c) Measured flow velocities at multiple locations within the channel at these operating conditions. Channel width is 5 mm.

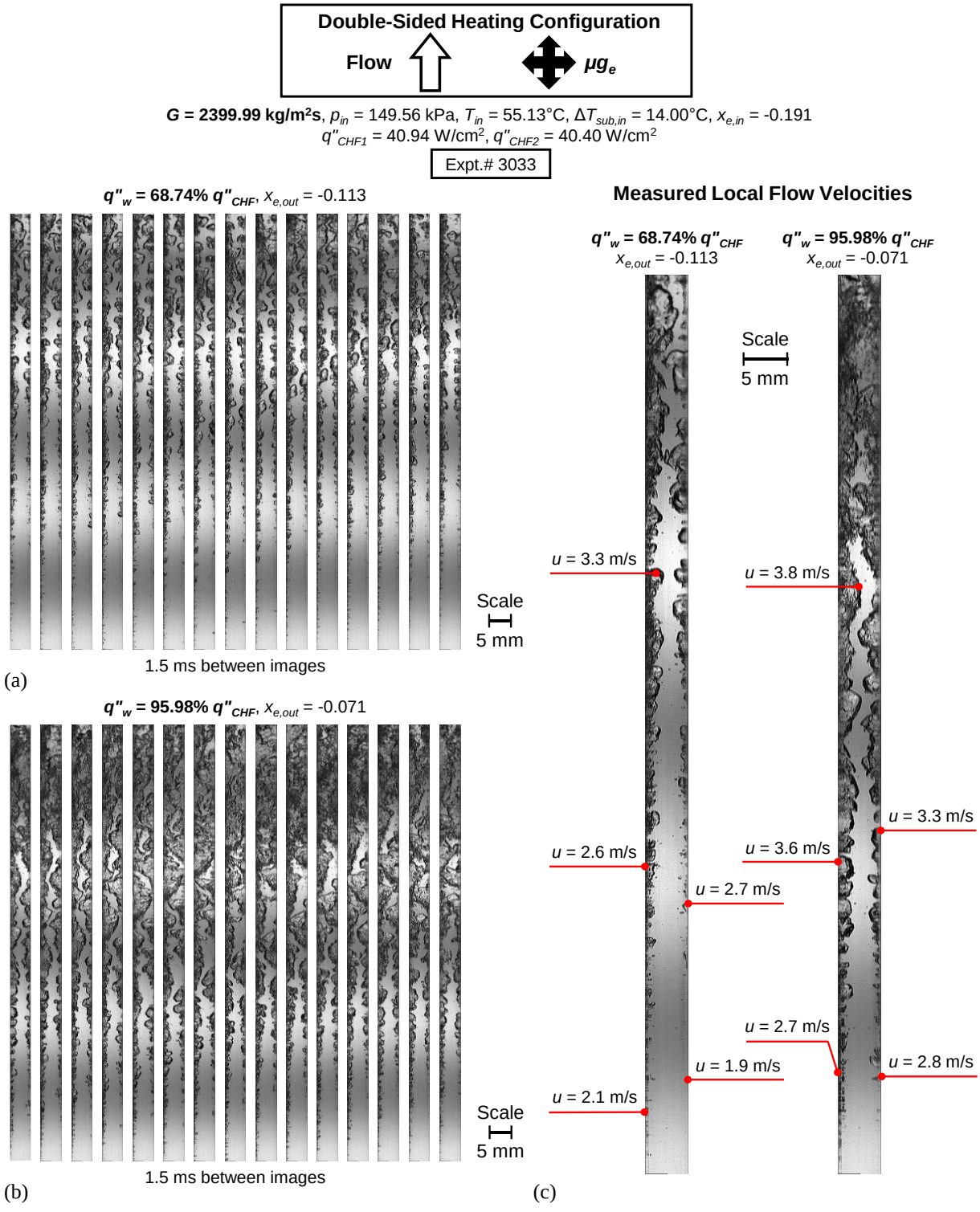

Fig. 15 Flow visualization image sequences for a mass velocity of $G \approx 2400$ kg/m^{2}s at a moderate inlet subcooling of $\Delta T_{sub,in} \approx 14.0$°C and higher inlet pressure of $p_{in} \approx 150$ kPa with double-sided heating at heat fluxes of $q''_w \approx$ (a) 69% and (b) 96% q''_{CHF}. Time interval between successive images is mentioned below each sequence. (c) Measured flow velocities at multiple locations within the channel at these operating conditions. Channel width is 5 mm.

3.3 Temporal Anomalies in Flow Behavior

Certain operating conditions, typically at high $\Delta T_{sub,in}$, produced flow instabilities that caused temporally anomalous flow patterns. Figs. 16-18 focus on three operating conditions during which flow instabilities were observed within the FBM. Flow sequences capturing linger periods of time and the corresponding temporal records of mass flow rate and inlet pressure are analyzed.

Fig. 16(a) features an image sequence with 10 ms between consecutive images, capturing a relatively severe flow instability. Routine flow patterns are present at the beginning of the image sequence until flow reversal of liquid from the outlet penetrates toward the inlet of the channel in image 8, destroying vapor structures within the channel. As the reversed flow propagates upstream, boiling resumes downstream, and the wavy vapor layers begin to redevelop in image 17. Normal flow resumes through the entire channel once forward inertia from the inlet overcomes the instability. The boiling boundary moves back towards the inlet and typical flow patterns redevelop throughout the channel by image 26. Towards the end of the time sequence, flow reversal is again observed from the outlet in image 35, restarting the cycle. Corresponding to the observed severe flow reversal, temporal records of mass flow rate and inlet pressure reveal signal fluctuations as shown in Fig. 16(b) and 16(c), respectively. Fig. 16(c) shows minor fluctuations in mass flow rate do exist, but they are more random in nature; however, it should be noted that mass flow rate is measured immediately downstream of the pump, where the instabilities might have a weaker effect. On the other hand, Fig. 16(c) shows exceptionally large pressure fluctuations at the FBM inlet and the periodic oscillations have a uniform amplitude and frequency. As already described in section 2.1, accumulator operation is controlled by pressure at the inlet of the FBM's heated section. The p_{in} fluctuations, as strong as they are, are accompanied by only insignificant oscillations in accumulator bellows' movement/travel.

Fig. 17(a) shows an image sequence with a spacing of 6 ms from a preceding heat increment of the same experimental case as Fig. 16. At this q''_w of 73.07% q''_{CHF}, flow reversal does not occur in the channel. However, a cyclic flow pattern resembling density wave oscillations (DWOs), a mild flow instability, is observed in the channel. The flow sequence begins with smooth waves of vapor covering a substantial portion of each heated wall downstream. As the long vapor structures exit the channel in image 13, a typical wavy-vapor-layer regime occurs in the channel. However, in image 32, another long, smooth vapor wave once again occupies each wall downstream. No flow reversal occurs from the outlet, and this results in relatively stable flow rate and pressure signals in Figs. 17(b) and 17(c). Small variations in inlet pressure are observed as the inconsistent amount of produced vapor and flow structures in the channel affect pressure drop.

Fig. 18(a) features an image sequence with a spacing of 18 ms and similar operating conditions as previous sub-figures but a higher G of 1280 kg/m^{2}s. The image sequence begins with large vapor patches in the downstream section, similar to those seen in Fig. 17(a). Flow reversal from the outlet begins in image 5 and flushes away vapor structures in the downstream section of the channel. Unlike Fig. 16(a), forward flow inertia prevents reversed flow from propagating through the entire channel before normal flow begins, and upstream vapor structures remain intact. Typical flow patterns resume in image 9 and continue until flow reversal occurs once again in image 33. Increased flow inertia prevents flow reversal from propagating upstream, resulting in a constant mass flow rate downstream of the pump, shown in Fig. 18(b). However, inlet pressure fluctuations are still observed in Fig. 18(c) but are relatively minor to those experienced with Fig. 16 with more severe flow reversal.

While the severity of the temporally anomalous flow patterns can be clearly seen to increase with increasing q''_w or decreasing G (*i.e.*, increasing Boiling number), trends regarding the frequency of cyclic flow anomalies are not as apparent. In some cases, the frequency of flow reversal is less than 1 Hz and is not captured in the one second of video recorded at the end of each heat increment. In other cases, flow transients are superimposed on one another, or they occur with non-uniform periods, complicating visually observed trends.

Further analysis of the instabilities, such as spectral analysis of the pressure signals to determine the frequency and amplitude of fluctuations, is currently limited by the data sampling frequency of 5 Hz.

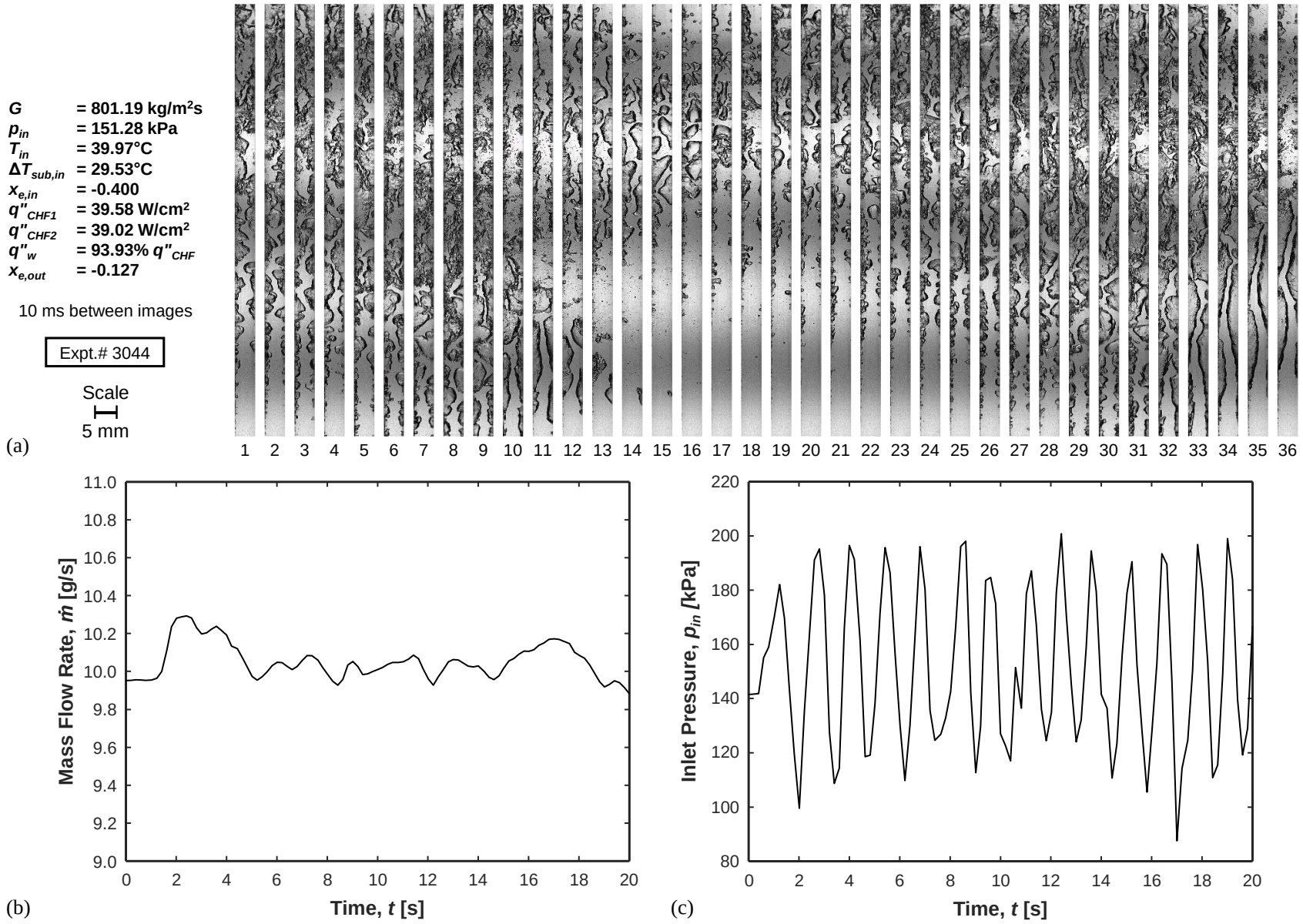

Fig. 16 Observed dynamic flow instabilities that are periodic in nature: (a) Flow visualization image sequences for highly subcooled inlet and mass velocity of $G \approx 801$ kg/m^{2}s with double-sided heating at heat flux of $q''_w \approx 94\%\ q''_{CHF}$. Time interval between successive images is 10 ms. Channel width is 5 mm. Corresponding temporal plots of (b) mass flow rate and (c) inlet pressure.

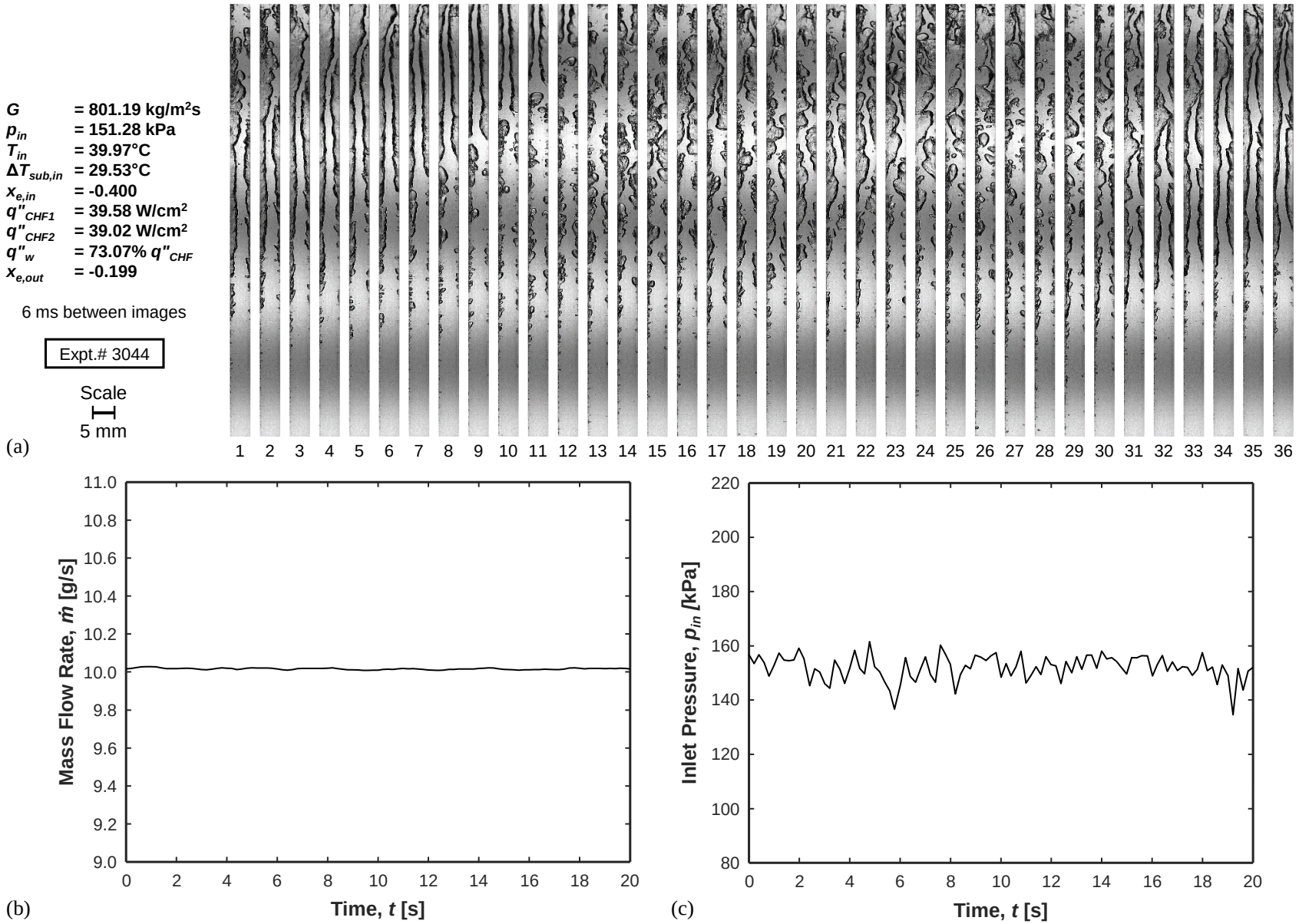

Fig. 17 Observed dynamic flow instabilities that are periodic in nature: (a) Flow visualization image sequences for highly subcooled inlet and mass velocity of $G \approx 801$ kg/m^{2}s with double-sided heating at heat flux of $q''_w \approx 73\%\ q''_{CHF}$. Time interval between successive images is 6 ms. Channel width is 5 mm. Corresponding temporal plots of (b) mass flow rate and (c) inlet pressure.

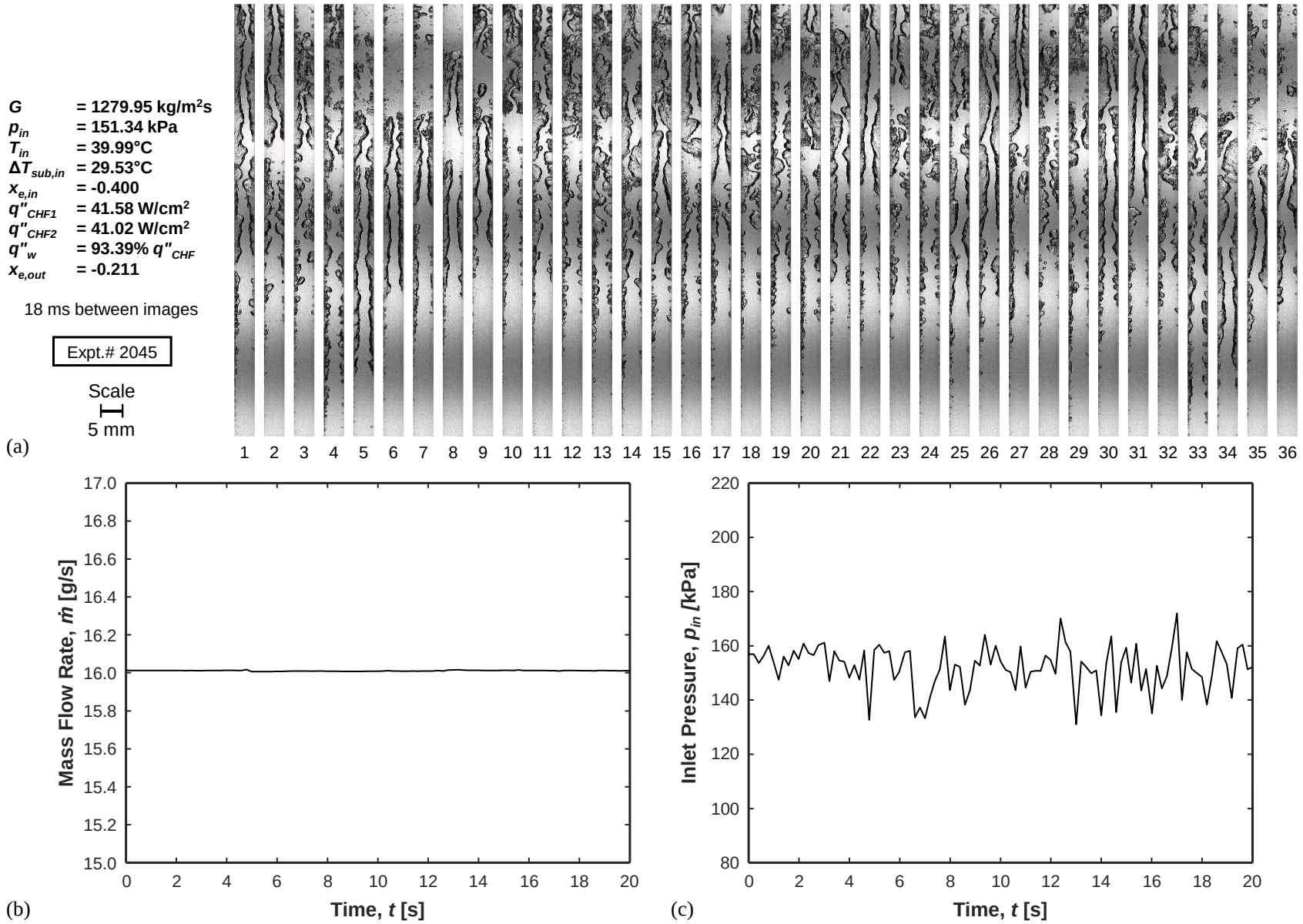

Fig. 18 Observed dynamic flow instabilities that are periodic in nature: (a) Flow visualization image sequences for highly subcooled inlet and mass velocity of $G \approx 1280$ kg/m^{2}s with double-sided heating at heat flux of $q''_w \approx 93\%\ q''_{CHF}$. Time interval between successive images is 10 ms. Channel width is 5 mm. Corresponding temporal plots of (b) mass flow rate and (c) inlet pressure.

4. Heat Transfer Results and Discussion for Double-Sided Heating

Heat transfer results in the form of averaged flow boiling curves, local wall temperatures, and local and average heat transfer coefficients are presented in this section for double-sided heating.

4.1 Flow Boiling Curves

All boiling curves presented in this study are plotted individually for each heated wall as a whole, as wall heat flux, q''_w, versus the average wall superheat, which is defined as average wall temperature, $\overline{T}_w$, minus saturation temperature at channel inlet, $T_{sat,in}$. They clearly portray both the heat transfer performance of each wall at various operating conditions and the various heat transfer regimes that constitute flow boiling.

Consider the boiling curves shown in Fig. 19. Recall that only heat increments with flow boiling are processed in this study, and not the lower q''_w where no boiling occurs. At the lower q''_w, the boiling curves have an exceedingly small slope, and this represents the heat transfer regime where single-phase liquid convection dominates over latent heat transfer offered by bubble nucleation. This typically occurs when the majority of the heated length undergoes liquid convection, while a small downstream portion of the wall undergoes boiling, or a few wall cavities are activated for bubbles incipience. The boiling regime at these heat fluxes is typically partially developed boiling (PDB) to a substantial extent, and maybe fully developed boiling (FDB) to a small extent. At a certain q''_w (~10 W/cm^2 in Fig. 19), the slope of the curves increases to a larger value. Although this transition point is typically denoted as ONB for a local curve, here it denotes the point where the net contribution of latent heat to overall heat transfer overshadows the effects of sensible heat; this occurs when the majority of the channel is occupied with the FDB regime. Past this ONB-like point, steady nucleate boiling renders the curves' slope constant at a high value. In this regime, large q''_w increases are associated with an exceedingly small rise in wall superheat. The FDB regime for this set of operating conditions is shown as a linear band in Fig. 19. At a certain higher q''_w ($\approx$ 24.25 – 28.91 W/cm^2 in Fig. 19), the curves' slope starts declining. This transition point denotes the onset of nucleate boiling degradation (ONBD), where the boiling performance is degraded due to a substantial portion of the heated wall being insulated with vapor, either in the form of dryout incipience at high outlet qualities or localized vapor patches at low outlet qualities. Beyond the ONBD point, the nucleate boiling degradation (NBD) regime lies, where although steady, the wall superheat rises for small q''_w increases. Finally, at a certain q''_w ($\approx$ 39.48 W/cm^2 in Fig. 19), the degradation becomes so severe that wall superheat sharply increases in an unsteady and uncontrolled fashion to 122°C. This transition point denotes the CHF, at which point the present experiments are terminated.

Note the significant difference between q''_{ONBD} and q''_{CHF} in Fig. 19, clearly indicating the importance in distinguishing between the two points. However, the present experiments were performed with a priority in accurately capturing CHF and not ONBD, so the heat increments are much coarser near ONBD, resulting in a low resolution in q''_{ONBD} and is hence not specified for each experiment.

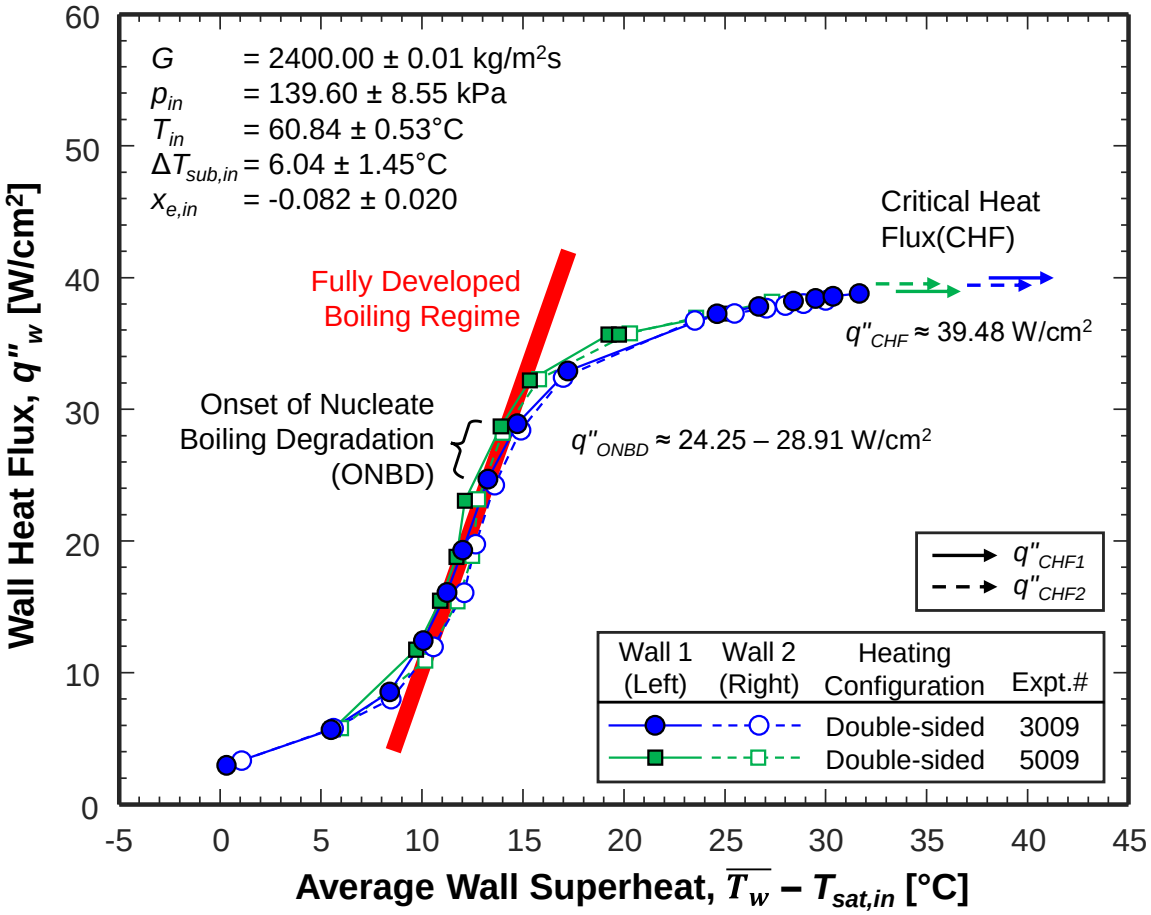

Fig. 19 Boiling curves confirming the repeatability of experiments and symmetry in boiling heat transfer at the two walls for double-sided heating at identical operating conditions of mass velocity of $G \approx 2400$ kg/m^{2}s, inlet pressure of $p_{in} \approx 140$ kPa, and inlet subcooling of $\Delta T_{sub,in} \approx 6$°C. The fully developed boiling regime is indicated as a red band. Note the ONBD and CHF transition points and associated heat fluxes.

4.1.1 Repeatability of Experiments and Symmetry in Boiling Heat Transfer at the Two Walls

The boiling curves in Fig. 19 help confirm both the repeatability of experiments and the symmetry in boiling heat transfer at the two walls for double-sided heating. Two experimental cases, 3009 and 5009, with near-identical operating conditions, are plotted for each wall. Experiment 3009 was performed on April 27, 2022, whereas 5009 was performed around three

weeks later on May 16, 2022. Between these two dates, several other experiments with vastly different operating conditions were performed. It is clear that the boiling curves for both experiments almost overlap with the same q''_{CHF}, proving that the present set of experiments are indeed repeatable.

Moreover, for both experiments, the curves for both the walls overlap with slight deviations, which could be attributed to minor differences in power supplied to each wall resulting in slightly different (i) heat fluxes, (ii) cavities activated for bubble nucleation, (iii) rate of vapor production, (iv) flow patterns, and finally, (v) heat transfer performance. One other likely reason could be experimental uncertainties. Nonetheless, the overlapping curves still prove symmetry in boiling at the two walls for the double-sided-heating experiments.

4.1.2 Effects of Mass Velocity

Boiling curves illustrating the effects of mass velocity for double-sided heating are included in Fig. 20 for six different combinations of inlet pressure and subcooling. Respectively shown on the left and right side are plots for low and high p_{in}, and from the top to bottom are plots for $\Delta T_{sub,in} \approx 4$, 15, and 30°C (as indicated to the right of the plots). Included in each plot are curves for different G ranging from 200 to 3200 kg/m^{2}s in small increments. Due to the large number of experimental cases presented in each plot, the curves represent averaged behavior for the two walls.

The top left plot in Fig. 20 shows boiling curves for all G overlapping from the lowest q''_w until ONBD. The outliers to this trend are $G \approx 2080$ and 3200 kg/m^{2}s, which have the lowest heat flux at slightly lower wall superheats compared to the other G. This could be attributed to a larger portion of heat transfer via single-phase convection and subcooled PDB, both of which are sustained for the majority of the channel length at high G. The heat flux required for ONBD, q''_{ONBD}, is highly dependent on G, and increases monotonically with increasing G. At the respective q''_{ONBD} for each G, the curves deviate from the nucleate-boiling cluster of curves and move toward CHF, with q''_{CHF} also monotonically increasing with increasing G.

Similar trends are observed in all the other five plots. Three new aspects are seen in the bottom plots for $\Delta T_{sub,in} \approx 30$°C. The nucleate boiling portions of the curves do not overlap, with the curves for high G lying towards the left with lower wall superheats. This is due to the stronger condensation effects of the bulk fluid at a combination of high $\Delta T_{sub,in}$ and high G sustaining subcooled boiling (both PDB and FDB) to the majority of the channel length, if not the whole, and subcooled boiling having a slightly smaller wall superheat when compared to saturated flow boiling. The second abnormal aspect is the $G \approx 800$ kg/m^{2}s curve in the bottom right plot showing a slight zig-zag trend in its NBD regime. This is a result of the temporal flow instabilities discussed

in section 3.3, causing severe oscillations in wall temperature and the 20 s steady-state averaging period being insufficient to smoothen out the oscillations. For instance, more oscillatory peaks could be included in the averaging when compared to troughs, resulting in a higher 'steady state' T_w value. The third aspect is the incomplete curves for $G \approx 3200$ kg/m^{2}s due to combinations of high G and high $\Delta T_{sub,in}$ resulting in large q''_{CHF} and the FBM heaters unable to reach those power levels.

4.1.3 Effects of Inlet Pressure

The effects of p_{in} can be deduced by comparing the left and right plots in each row of Fig. 20. Similar to the conclusion for flow patterns, there are no significant differences in the boiling curves obtained at the two p_{in} values, meaning p_{in} in the present range has a negligible effect on overall heat transfer. Note that a 30 kPa difference in p_{in} reflects a ~7°C difference in saturation temperature, so even if the wall superheats are identical for two p_{in} values, the walls for the higher p_{in} would be ~7°C hotter for the same q''_w dissipated.

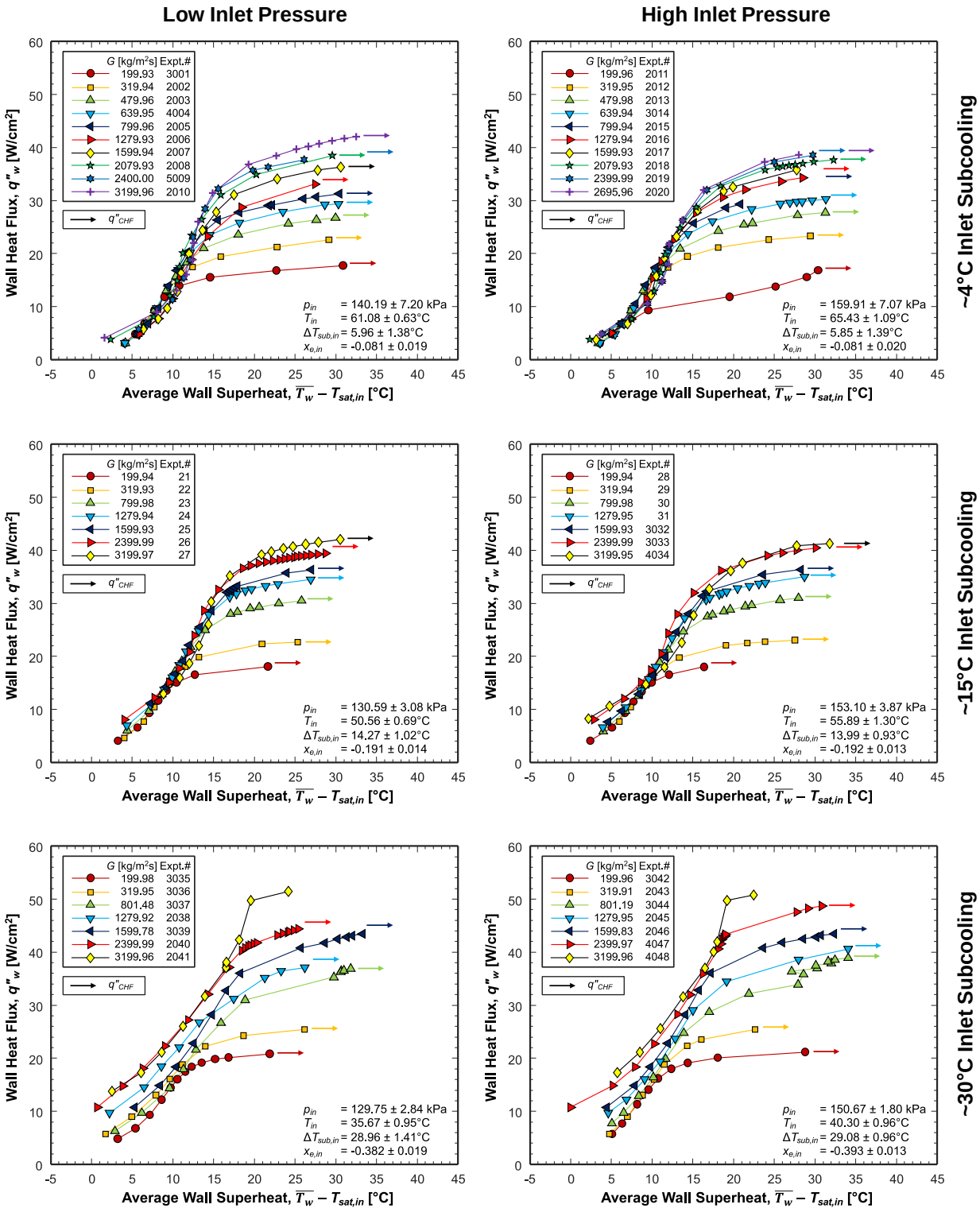

Fig. 20 Boiling curves illustrating the effects of mass velocity for double-sided heating at different combinations of inlet pressure (low and high) and inlet subcooling (4, 15, and 30°C). Exact operating conditions (inlet pressure, p_{in}, inlet temperature, T_{in}, inlet subcooling, $\Delta T_{sub,in}$, and inlet quality, $x_{e,in}$) for the data in each plot are included within the respective plot. Within each plot, each curve pertains to a mass velocity varied in the range of $G \approx 200 - 3200$ kg/m^{2}s.

4.1.4 Effects of Inlet Subcooling

Boiling curves illustrating the effects of $\Delta T_{sub,in}$ for double-sided heating are included in Fig. 21 for three mass velocities of $G \approx 200$, 800, and 2400 kg/m^{2}s at the higher p_{in}. Included in each plot are curves for a variety of subcoolings in the range of $\Delta T_{sub,in} \approx 2 - 45$°C (although the exact values are determined from the experimental data collected).

Fig. 21(a) shows all boiling curves superimposed on top of each other until the ONBD point, after which they diverge from the nucleate-boiling cluster. In general, both q''_{ONBD} and q''_{CHF} monotonically increase with increasing $\Delta T_{sub,in}$, although some trends are slightly interchanged if the differences in parameters lie within experimental uncertainty limits. This is especially noticeable for near-saturated inlet due to experiments performed for fine increments in $\Delta T_{sub,in}$, meaning the actual q''_{CHF} would be very close to each other but not accurately captured via the heat increments used.

The curves in Fig. 21(b) for the moderate G of 800 kg/m^{2}s follow the same general trends as Fig. 21(a), but the same abnormalities (zig-zag trend, incomplete curve at the higher q''_w) already discussed in section 4.1.2 are observed for some curves and the same reasoning is valid here too. The curves in Fig. 21(c) for the highest G of 2400 kg/m^{2}s also portray the same general trends and abnormalities as the top two sub-figures. Three aspects are obvious: (i) the much larger difference between q''_{ONBD} and q''_{CHF} for lower $\Delta T_{sub,in}$ and (ii) the almost no difference between q''_{ONBD} and q''_{CHF} for the highest $\Delta T_{sub,in}$, and (iii) movement of curves toward the left upon increasing $\Delta T_{sub,in}$. Aspect (i) is due to the majority of the channel undergoing locally saturated boiling, meaning nucleate boiling slowly degrades and the CHF mechanism is suspected to resemble the dryout type, which is characterized by a substantial amount of vapor content near the channel exit. This is verified from Fig. 8(f), where for $q''_w > \sim 50\%\ q''_{CHF}$, the channel exit is saturated, and CHF occurs via gradual extinguishing of wetting fronts. Aspect (ii) is due to the strong condensing potential of the incoming fluid forcing the majority of the channel to undergo locally subcooled boiling, meaning the CHF mechanism resembles the DNB (departure from nucleate boiling) type, which occurs due to localized vapor patches insulating the channel from fresh liquid access for boiling, even though there might be liquid away from the walls. This is seen in the flow patterns in Fig. 9(f), where at CHF, both a thick liquid core and several wetting fronts are still present due to the fluid being highly subcooled at the channel exit. Aspect (iii) is also observed in Fig. 20 and the same reasons discussed in section 4.1.2 are valid here.

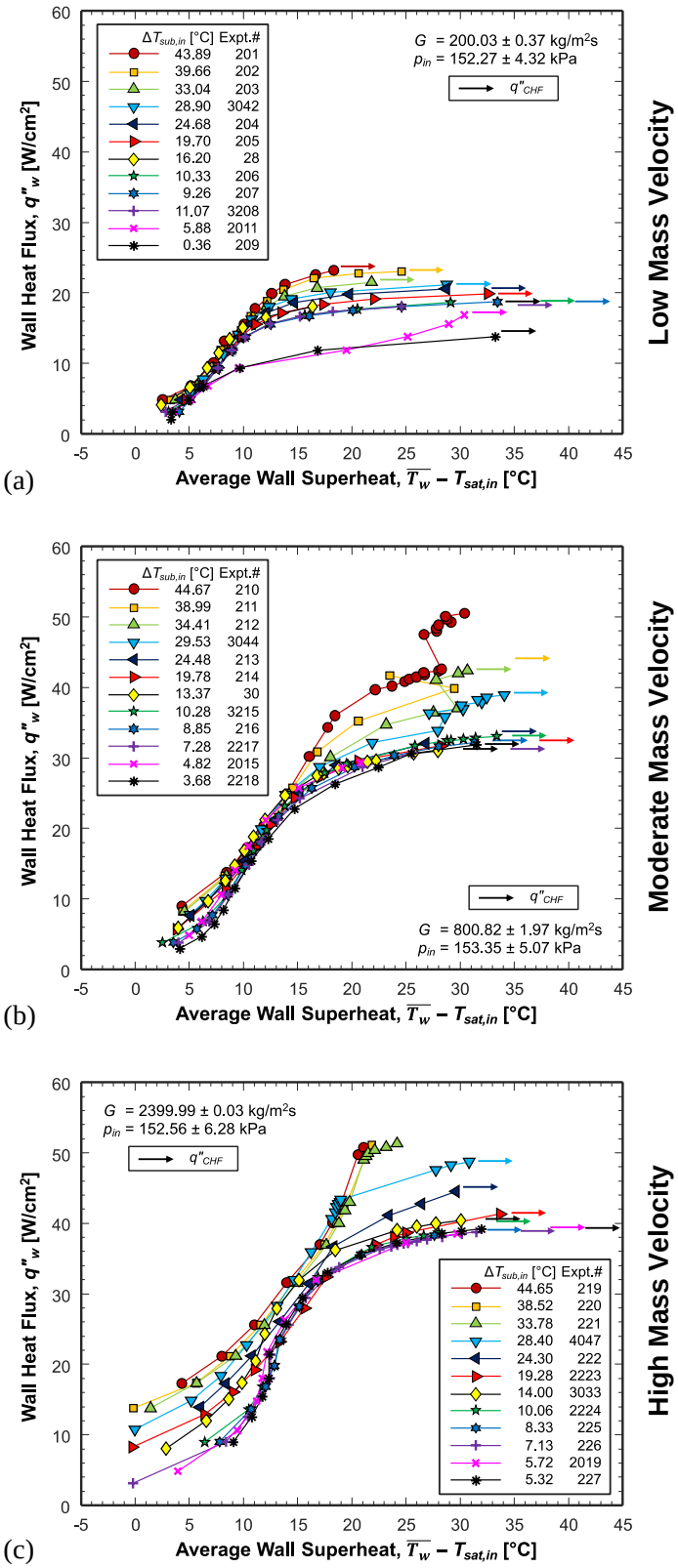

Fig. 21 Boiling curves illustrating the effects of inlet subcooling for different mass velocities of $G \approx$ (a) 200, (b) 801, and (c) 2400 kg/m^{2}s with double-sided heating. Exact operating conditions (mass velocity, G, and inlet pressure, p_{in}) for the data in each plot are included within the respective plot. Within each plot, each curve pertains to an inlet subcooling varied in the range of $\Delta T_{sub,in} \approx 0 - 45$°C.

4.2 Local Wall Temperature

Streamwise profiles of local temperature at both walls ($T_{w,z}$) for double-sided heating are presented in Fig. 22 for a variety of operating conditions. Eight plots constitute Fig. 22, and they are ordered in the following fashion: respectively arranged from the top to bottom are plots for combinations of low G and low p_{in}, moderate G and low p_{in}, high G and low p_{in}, and high G and high p_{in}, with the plots on the left and right columns respectively for highly subcooled and near-saturated inlet. Included in each plot are profiles for six intermediate heat fluxes between ONB and CHF (reported as average percentages of q''_{CHF} although the q''_{CHF} for both walls are slightly different).

The top left plot in Fig. 22 shows, at lower heat fluxes, the T_w profiles are rather flat and, as q''_w is increased, the profiles become increasingly curved with a concave-downward shape. At the lowest q''_w, single-phase convection and PDB regimes dominate the majority of the channel length, and the walls are rather isothermal. The concavity in the profiles for higher q''_w is due to:

(i) thermal-boundary-layer effects upstream in combination with the highest fluid subcooling leading to the lowest T_w at location 1 (see Fig. 3(d) for designation),

(ii) weakening of these upstream enhancement effects, the fluid's gradual heat gain, and formation of wavy vapor layer, all leading to gradual T_w increase as the flow progresses along the channel,

(iii) flow acceleration effects produced by significant vapor production enhancing convective effects and a gradual T_w decrease in the channel downstream near the channel exit, and

(iv) practical design of the FBM's heating strips being slightly longer and wider than the actual nPFH heating length and width (to effectively embed the heating strips within the polycarbonate plates and seal using O-rings) resulting in the heating elements at both ends serving slightly larger surface areas, providing slightly lower local q''_w and lower T_w at the strips' ends.

At all streamwise locations, T_w increases with increasing q''_w. The location of CHF manifestation is also evident from the T_w maxima close to CHF [24,38] in Fig. 22. For the low G plots in row 1, highly subcooled inlet shows CHF at around location 6 and near-saturated inlet at around location 5. For the moderate and high G plots in rows 2, 3, and 4, both highly subcooled and near-saturated inlets show CHF at around the middle of the channel, *i.e.*, locations 4 and 5.

With regards to p_{in}, both plots in row 3 have the same trends as those in row 4, however the higher p_{in} has the T_w profiles at ~4-7°C higher than the lower p_{in}, due to the corresponding T_{sat} as already discussed in section 4.1.3.

4.2.1 Deviations in Wall Temperature of Both Walls for Double-Sided Heating

For all operating conditions (including q''_w) in Fig. 22, the profiles for both walls are generally identical with the following deviations and associated reasons.

(i) The slight deviations of the entire profiles are due to differences in the actual q''_w supplied to each wall (see in Fig. 4 how q''_w at the two walls are not exactly identical for each heat increment) and the ensuing differences in vapor production and wall superheat.

(ii) The entire-profile deviations are smaller at lower q''_w, but larger at higher q''_w, especially close to CHF. These are because of NBD amplifying the superheat differences between ONBD and CHF.

(iii) The profile deviations do not show preference to a particular wall, with any of the two walls having a higher profile. For example, the top row in Fig. 22 shows, at the highest q''_w, the left-side highly-subcooled-inlet plot has T_{w1} entirely higher than T_{w2} and the right-side near-saturated-inlet plot has T_{w2} higher than T_{w1}.

(iv) The deviation between the two walls is most pronounced at streamwise location 1 (see Fig. 3(d) for designation). For example, all plots in rows 2, 3, and 4 of Fig. 22 show $T_{w1,1} >> T_{w2,1}$. This is possibly because of wall 1 suffering from NBD at location 1, increasing the local wall superheat, while wall 2 has unimpeded nucleate boiling at location 1.

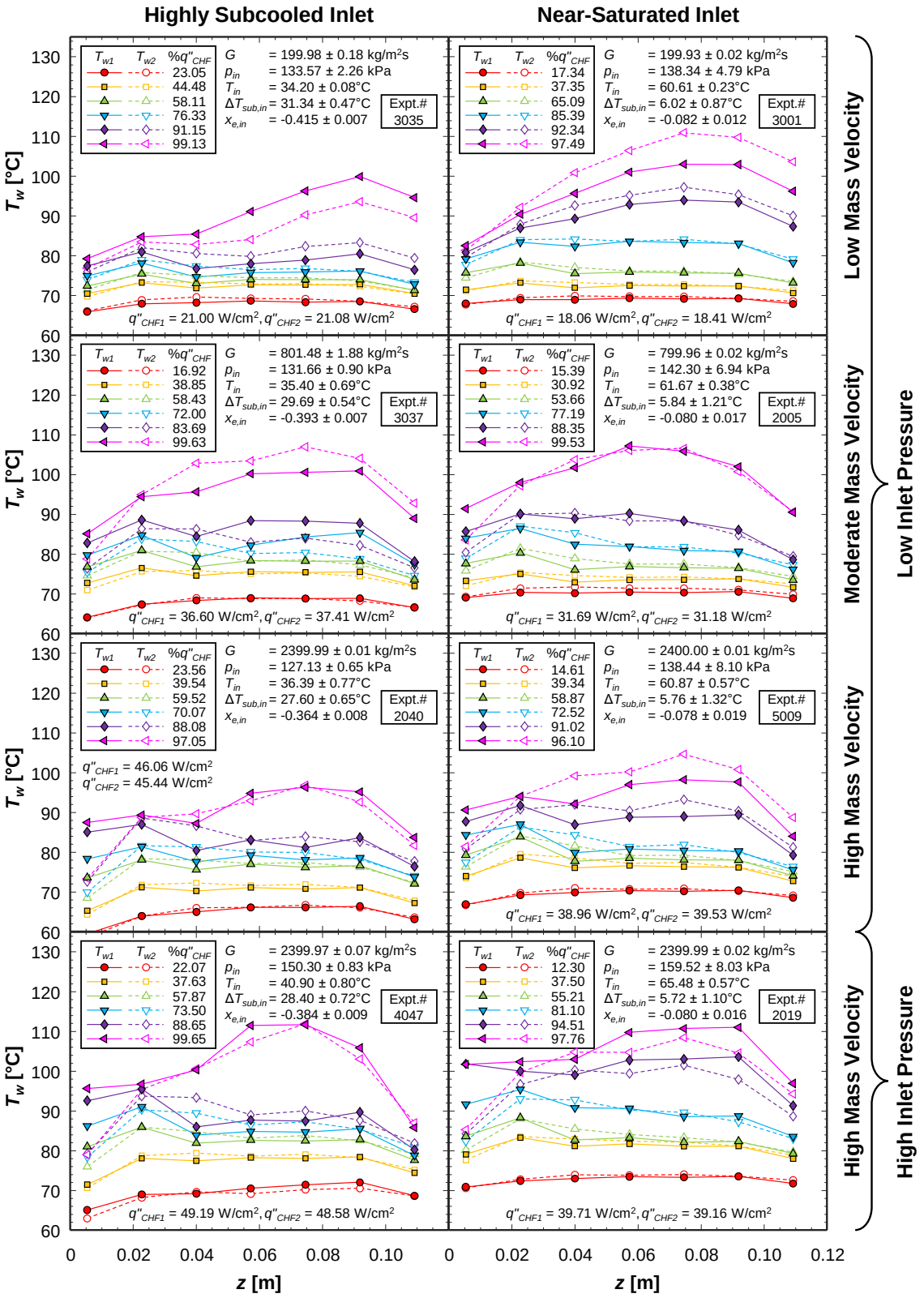

Fig. 22 Streamwise profiles of local temperature at both walls (double-sided heating) for different heat fluxes at a variety of operating conditions. Exact operating conditions (mass velocity, G, inlet pressure, p_{in}, inlet temperature, T_{in}, inlet subcooling, $\Delta T_{sub,in}$, and inlet quality, $x_{e,in}$) for the data in each plot are included within the respective plot. Within each plot, each curve pertains to a different heat flux, q''_w.

4.3 Local Heat Transfer Coefficient

4.3.1 Streamwise Profiles of Local Heat Transfer Coefficient

Streamwise profiles of local heat transfer coefficient (h_z) at both walls for double-sided heating are presented in Fig. 23 for a variety of operating conditions. The layout of this figure, including the chosen experimental cases, is identical to Fig. 22.

The top left plot shows the h profile for the lowest q''_w to be flat and lowest due to the dominant single-phase convection and PDB regimes yielding almost constant, low h all along the channel. As q''_w is increased, the profiles gradually move upwards until a certain limit, after which they degrade to a low value. This is because of the increased contribution of latent heat to total heat transfer until local ONBD, after which NBD degrades the heat transfer performance. All the h profiles for moderate q''_w (say until 91.15% q''_{CHF} in this plot) start from a minimum near the inlet and gradually grow towards the channel exit. This is due to strong acceleration effects benefitting convective boiling. However, remarkably close to CHF (at 99.13% q''_{CHF} in this plot), the h profile starts degrading after a certain downstream location, which marks the onset of dominance of NBD effects (*i.e.*, formation of thick wavy vapor layer along the heated wall and extinguishment of wetting fronts) over acceleration effects.

The other plots for highly subcooled inlet in the left column of Fig. 23 also show similar trends. The one new trend is the larger h at location 1 compared to location 2 due to the higher G having stronger thermal entrance effects.

The h profiles for near-saturated inlet in the right column of Fig. 23 are generally higher than those for highly subcooled inlet. This is because saturated boiling is sustained at a smaller temperature difference between the wall and the fluid when compared to subcooled boiling. In both boiling situations, the wall needs to have a positive superheat to sustain boiling, but the fluid is at T_{sat} for saturated boiling and significantly below T_{sat} for highly subcooled boiling.

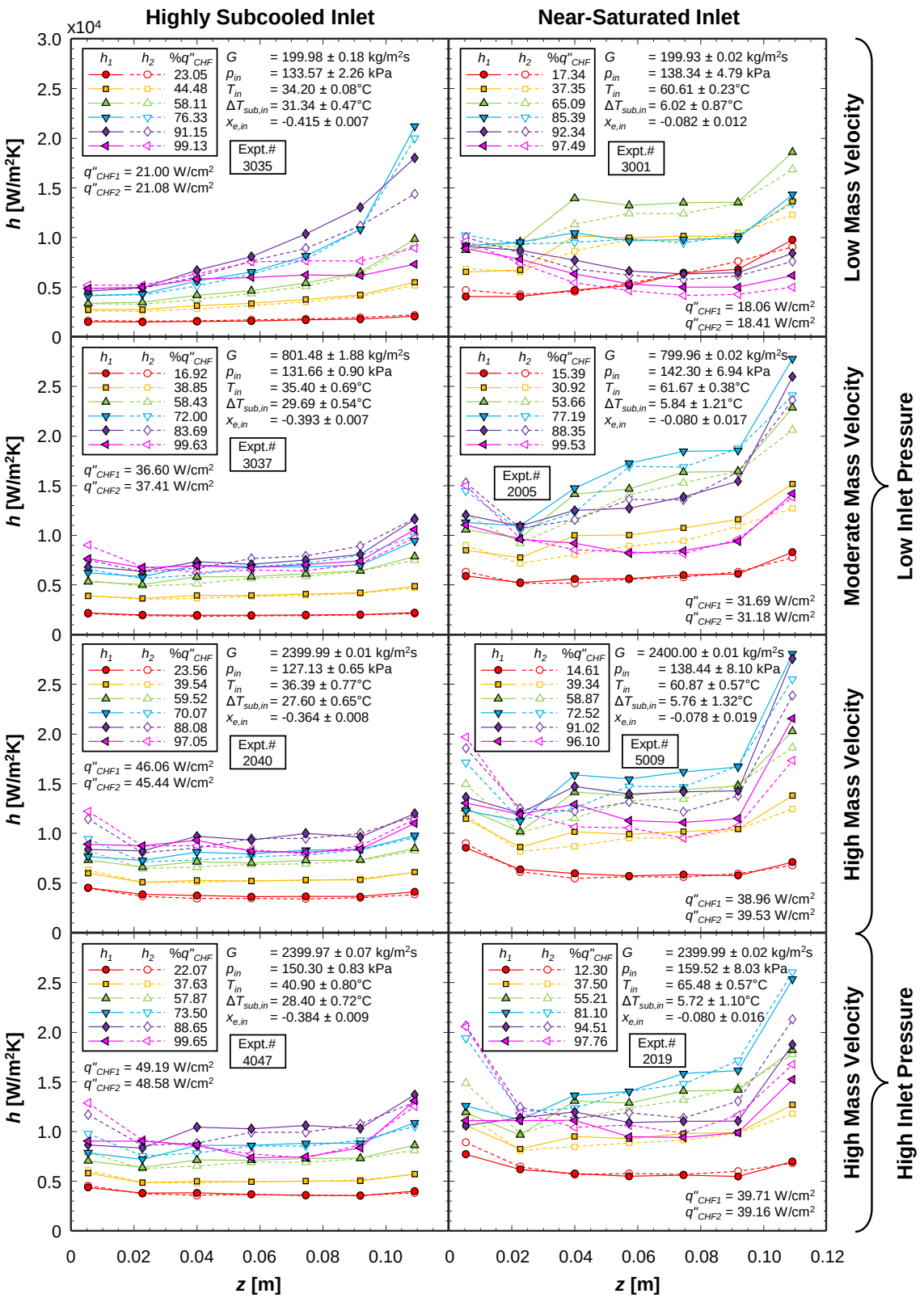

Fig. 23 Streamwise profiles of local heat transfer coefficient at both walls (double-sided heating) for different heat fluxes at a variety of operating conditions. Exact operating conditions (mass velocity, G, inlet pressure, p_{in}, inlet temperature, T_{in}, inlet subcooling, $\Delta T_{sub,in}$, and inlet quality, $x_{e,in}$) for the data in each plot are included within the respective plot. Within each plot, each curve pertains to a different heat flux, q''_w.

4.3.2 Variations of Local Heat Transfer Coefficient with Local Thermodynamic Equilibrium Quality

Plots of local heat transfer coefficient (h_z) at both walls for double-sided heating versus local thermodynamic equilibrium quality (x_e) are presented in Fig. 24 for a variety of operating conditions. Once again, the layout and choice of cases is identical to Figs. 22 and 23 for easy cross referencing, but the horizontal axes for x_e span different ranges in each plot. Typically, for saturated flow boiling, these plots help identify the local boiling mechanisms based on local flow quality, x. Note that $x \approx x_e$ only for saturated or near-saturated inlet. But in the present plots, it is difficult to make these connections due to the vastly different subcooled inlet conditions (especially $\Delta T_{sub,in}$) resulting in large thermodynamic non-equilibrium and significant differences between x_e and x. This means, for the same local x_e, the boiling mechanism could be different. Nonetheless, the plots here are used to roughly infer typical boiling behavior.

In all the plots, the curves span the narrowest x_e range for lower q''_w, and the span increases upon increasing q''_w due to the increased amount of total heat added to the fluid. Comparing the plots in the left and right columns, the x_e span is broader for highly subcooled inlet compared to near-saturated inlet because of fluid's ability to absorb more heat before CHF is achieved.

The highly-subcooled-inlet plots in the left column show for lower x_e, h_z is flat, but it increases with increasing q''_w, a key characteristic of nucleate boiling regime dominance. However, at higher x_e, the curves begin overlapping while still being almost flat, meaning an independence of h_z on q''_w, a key characteristic of onset of convective boiling dominance. Liquid-film evaporation (*i.e.*, evaporation of wetting fronts here) along with accelerated flow inertia causes h_z to increase with increasing x_e at the highest x_e range. However, at the highest q''_w values, extinguishment of wetting fronts and reduced liquid availability at the walls for boiling counteracts the enhancement effects of liquid-film evaporation.

The near-saturated plots seem to show similar trends but discerning them is difficult due to practical difficulties in maintaining a constant $x_{e,in}$ throughout the boiling curve (due to p_{in} increasing as q''_w is increased) and ($x_{e,in}$ - $x_{e,out}$) being smaller than the practical $x_{e,in}$ variations.

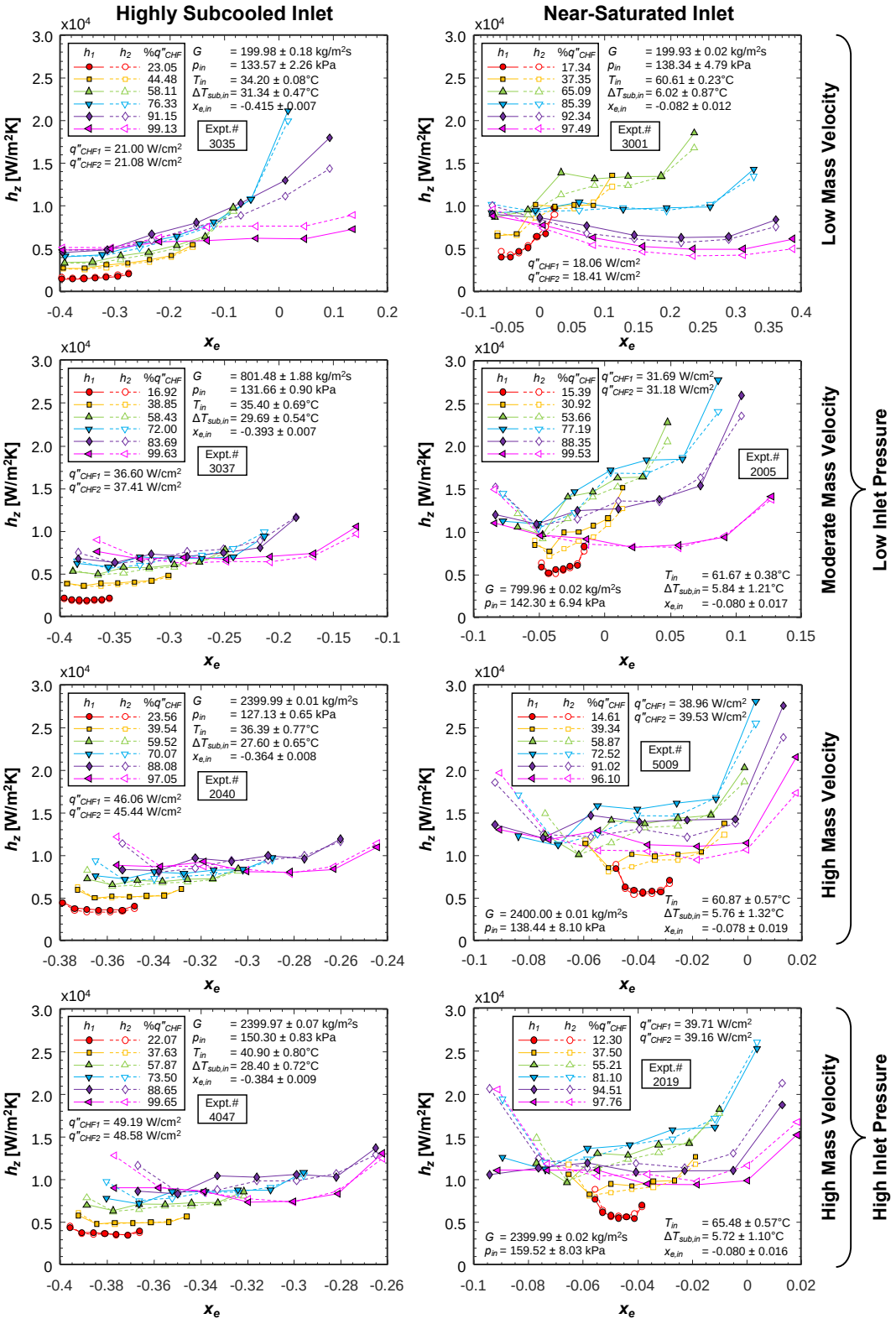

Fig. 24 Variations of local heat transfer coefficient, h_z, at both walls (double-sided heating) versus local thermodynamic equilibrium quality, x_e, for different heat fluxes at a variety of operating conditions. Exact operating conditions (mass velocity, G, inlet pressure, p_{in}, inlet temperature, T_{in}, inlet subcooling, $\Delta T_{sub,in}$, and inlet quality, $x_{e,in}$) for the data in each plot are included within the respective plot. Within each plot, each curve pertains to a different heat flux, q''_w.

4.4 Average Heat Transfer Coefficient

Plots depicting the variation of average heat transfer coefficient ($\bar{h}$) versus wall heat flux (q''_w) for each wall of double-sided heating are presented in Fig. 25 for six sets of operating conditions. The plots are laid out as follows: respectively arranged from the top to bottom are $\Delta T_{sub,in} \approx 30$, 15, and 4°C with the left and right columns respectively corresponding to low and high p_{in}. Included in each plot are curves for $G \approx 200$, 800, and 2400 kg/m^{2}s.

For all $\Delta T_{sub,in}$ and G, the curves are almost identical between the left and right plots, meaning p_{in} has no effect on these values or parametric trends. The general trend seen in all curves in Fig. 25 include: (i) starting from the lowest q''_w, $\bar{h}$ monotonically increases with increasing q''_w (ii) $\bar{h}$ reaches a peak value at a certain intermediate q''_w, and finally (iii) $\bar{h}$ monotonically decreases with increasing q''_w until a minima at CHF. The initial increase in $\bar{h}$ is due to unimpeded nucleate boiling gradually enabling additional latent heat exchange. This region is more broad and linear for high $\Delta T_{sub,in}$ and high G, where the bulk fluid offers strong condensation to the produced vapor, and nucleate boiling is unimpeded. However, at low G and/or high $\Delta T_{sub,in}$, this region is slightly less linear and narrow. The peak $\bar{h}$ corresponds to ONBD, beyond which nucleate boiling is degraded due to the avaialbility of fewer wetting fronts for boiling. The latter $\bar{h}$ decrease is due to NBD, and this region is more broad for near-saturated inlet, where the produced vapor significatly increases the void fraction within the channel due to insufficient condensation in the liquid core.

The peak value of $\bar{h}$ does not follow any fixed trend with respect to G. For $\Delta T_{sub,in} \approx 30$°C, peak $\bar{h}$ is highest at $G \approx 200$ kg/m^{2}s, whereas for $\Delta T_{sub,in} \approx 15$°C, peak $\bar{h}$ is the same for all G, and for $\Delta T_{sub,in} \approx 4$°C, peak $\bar{h}$ is highest for $G \approx 800$ and 2400 kg/m^{2}s. Between highly subcooled and near-saturated inlet, the latter yields higher peak $\bar{h}$ due to the fluid and wall temperatures being close to each other, as already discussed in section 4.3.1.

$G \approx 200$ kg/m^{2}s in the bottom right plot exhibits an anomalous S-shaped curve. The reason for the second inflection at higher heat fluxes is the very low Boiling number causing flow instabilities (as discussed in section 3.3) with large oscillations in wall temperature (and the steady-state averaging period being smaller than the oscillation period).

Overall, the general parametric trends of microgravity flow boiling for double-sided heating with subcooled inlet are similar to both single-sided heating in microgravity [24] and single- and double-sided heating of vertical upflow in Earth gravity [38].

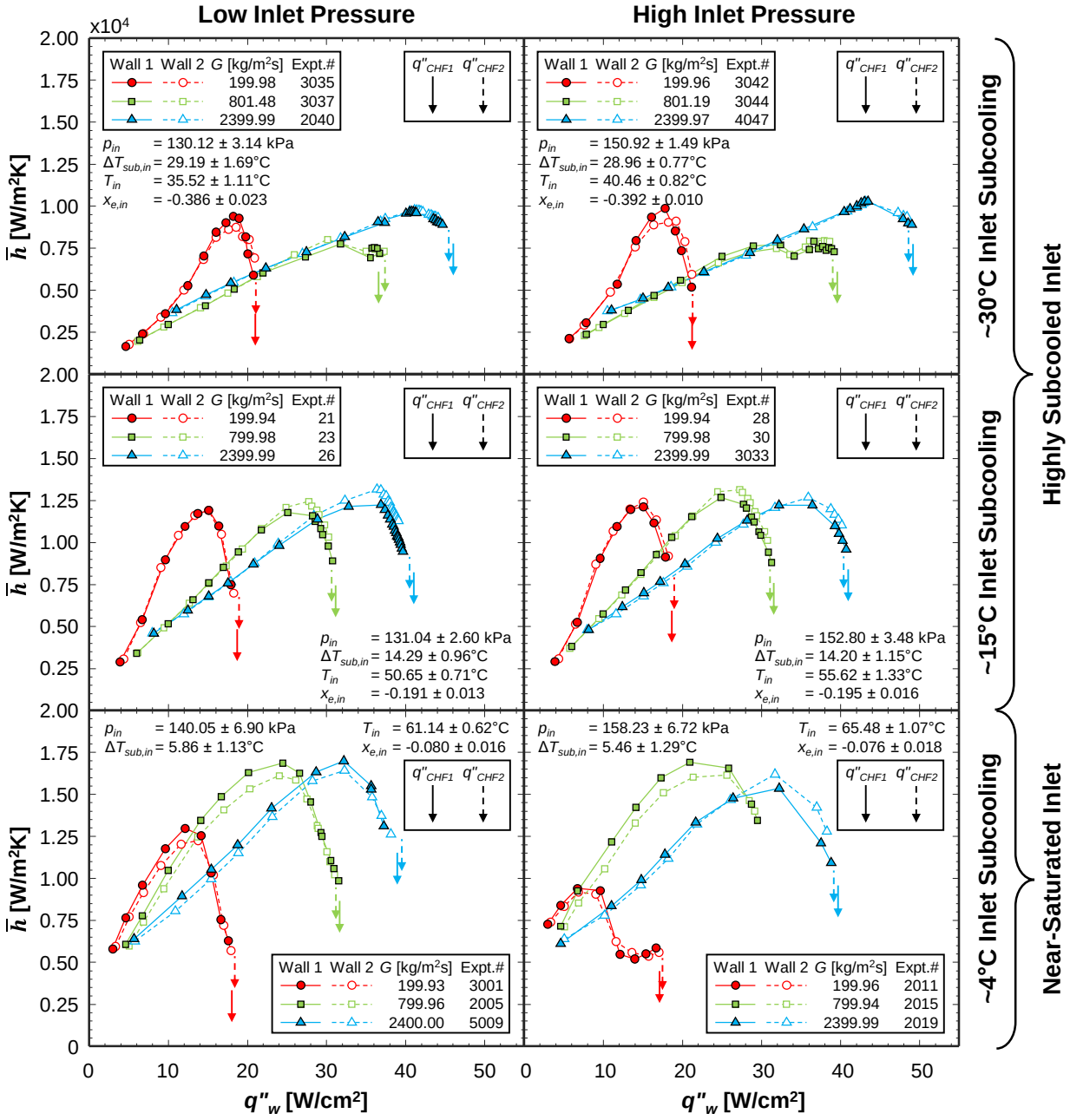

Fig. 25 Variations of average heat transfer coefficient, $\bar{h}$, along each wall (double-sided heating) with wall heat flux, q''_w, for three mass velocities at six different inlet conditions (three inlet subcoolings × two inlet pressures). Exact operating conditions (inlet pressure, p_{in}, inlet temperature, T_{in}, inlet subcooling, $\Delta T_{sub,in}$, and inlet quality, $x_{e,in}$) for the data in each plot are included within the respective plot. Within each plot, each curve pertains to a different mass velocity in the range of $G \approx 200 - 2400$ kg/m^{2}s.

5. Effects of Heating Configuration for Subcooled Inlet Conditions

The effects of heating configuration on both heat transfer and interfacial flow physics are elucidated in this section for subcooled inlet. To perform this, data from the double-sided-heating experiments presented in sections 2-4 of this study (see Table 4) are compared and contrasted against the single-sided-heating data reported in [24].

5.1 Flow Patterns

Fig. 26 presents flow-pattern images along the boiling curve for cases with a moderate G of ~800 kg/m^{2}s, in order to compare single-sided (which were presented in [24]) and double-sided heating.

Figs. 26(a) and 26(b) depict images with a relatively low $\Delta T_{sub,in}$ of ~6 – 7°C for single- and double-sided heating, respectively. At low subcooling, vapor production is abundant within the channel, and near 50% q''_{CHF}, vapor occupies the entire cross section of the channel's downstream in both heating configurations. In single-sided heating, there is no interaction of the vapor produced along the one heated wall with any other vapor structures, so the evolution is undisturbed and there is potential for the bubble boundary and vapor layer to occupy the entire cross section of the channel. See 54.17% q''_{CHF} in Fig. 26(a) where the vapor starts touching the opposite unheated wall at a downstream location. On the other hand, in double-sided heating, above a certain q''_w, the bubble boundary and/or vapor layers produced at the two heated walls interact with one another. See 33.84% q''_{CHF} in Fig. 26(b) where the vapor structures start touching each other near the channel exit, and at 47.39% q''_{CHF}, the two layers start *meshing* together like the teeth of two mechanical gears do, before completely *merging* together near the channel exit. The locations where, for single-sided heating, the vapor layer starts touching the opposite wall, and for double-sided heating, the gear-teeth-meshing and merging commence, all move upstream as q''_w is increased. Another aspect is, compared to single-sided, double-sided has significantly more vapor present within the channel all along the boiling curve, and flow patterns become more chaotic as vapor layers from opposite heated walls merge. Approaching CHF, additional vapor production in double-sided accelerates the flow, yielding a 24.2% larger q''_{CHF} than single-sided for near-saturated inlet.

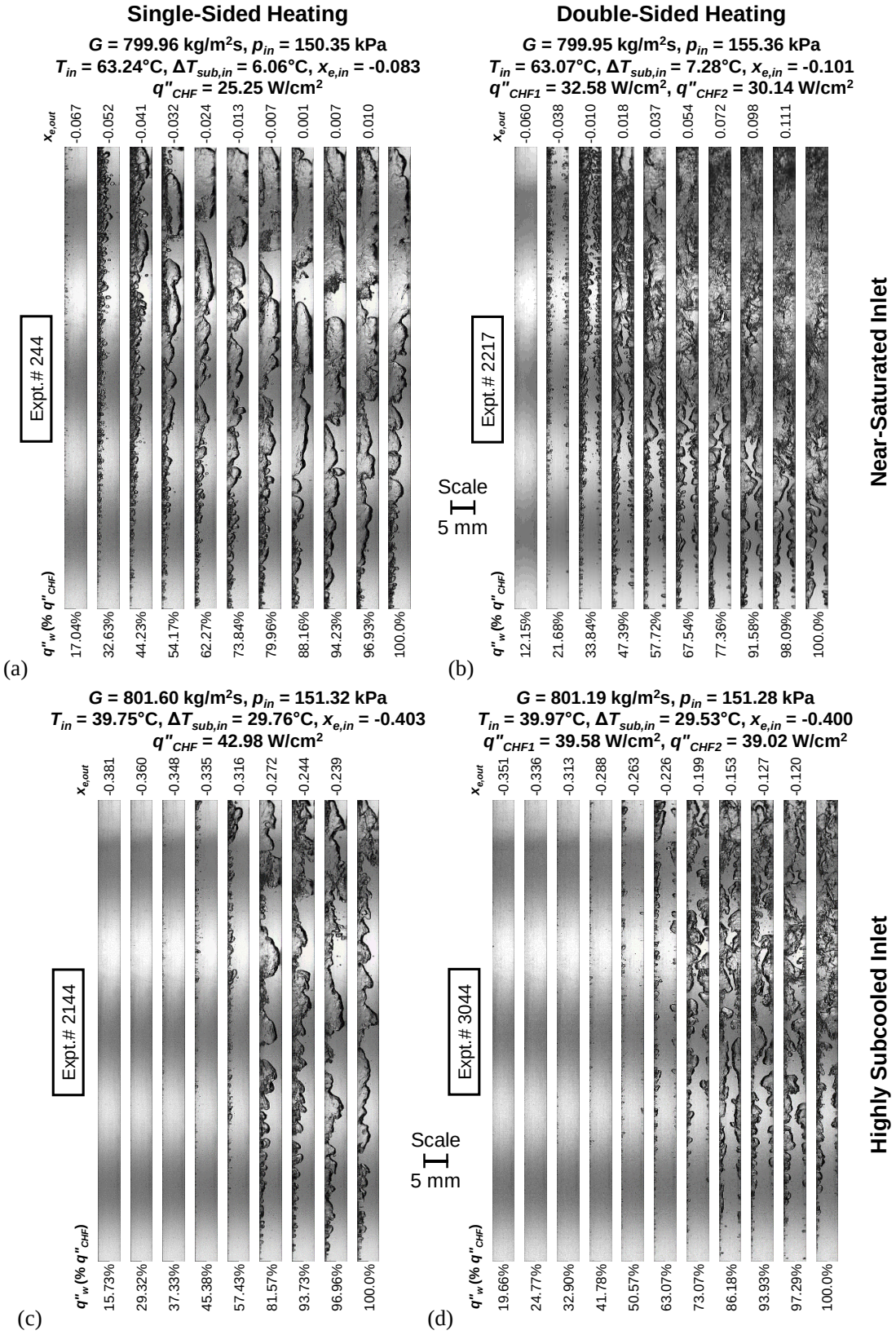

Fig. 26 Comparison of flow patterns for single- and double-sided heating at two representative operating conditions. (a) and (b) compare for near-saturated inlet, $\Delta T_{sub,in} \approx 6.7$°C, while (c) and (d) compare for highly subcooled inlet, $\Delta T_{sub,in} \approx 29.7$°C. Mass velocity is maintained constant at $G \approx 801$ kg/m^{2}s and inlet pressure at $p_{in} \approx 152$ kPa. Channel width is 5 mm.

Images along the boiling curve for single- and double-sided heating with a higher $\Delta T_{sub,in}$ of ~30°C, are respectively shown in Figs. 26(c) and 26(d). In both single- and double-sided heating, strong condensation effects limit vapor production, and vapor is not noticeable along the wall until approximately 40% q''_{CHF}. In fact, the vapor layers are so thin that, for single-sided, it barely touches the opposite wall even at CHF, and for double-sided, they barely merge together even at CHF. In double-sided heating, as CHF is approached, heat input from both heated walls more rapidly increases the equilibrium quality along the channel and decreases the effects of subcooling. During single-sided heating, the stronger effects of subcooling all along the channel result in a 9.4% larger q''_{CHF} than double-sided for highly subcooled inlet.

5.2 Heat Transfer Aspects – Flow Boiling Curves

Flow boiling curves comparing single- and double-sided heating are presented in Fig. 27 for $G \approx 200$ kg/m^{2}s. The figure has several plots presented in this layout: respectively arranged from the top to bottom row are $\Delta T_{sub,in} \approx 4$, 15, 20, 25, and 30°C (in an increasing order) with the left and right columns respectively corresponding to low and high p_{in}. Each plot contains one curve for single-sided and two curves for double-sided.

In general, for the entire operating ranges in the present study, the lower portions of the single- and double-sided curves overlap (almost perfectly in most cases); this corresponds to the nucleate boiling regime. At the ONBD point, both curves deviate from the slope established in the nucleate boiling regime. This deviation is easily noticeable for the heating configuration which has the lower q''_{ONBD} of the two. For example, see the top 2 rows in Fig. 27; single-sided has the lower q''_{ONBD} and the respective boiling curve is seen deviating early from the double-sided curve. Clearly, at lower $\Delta T_{sub,in}$, single-sided has lower q''_{ONBD} and q''_{CHF} compared to double-sided. When the fluid subcooling is lower, the bulk fluid's condensing potential is lower, and most of the produced vapor remains intact, increasing the void fraction and flow acceleration, which aids effective convection of produced vapor from the channel, delaying CHF to higher heat fluxes. For the same q''_w, compared to single-sided, double-sided supplies twice the heat into the fluid due to twice the heating surface area. So, for the same q''_w, double-sided produces almost twice the vapor than single-sided, and this greatly enhances flow acceleration and q''_{ONBD} and q''_{CHF}.

On the other hand, at higher $\Delta T_{sub,in}$, single-sided has higher q''_{ONBD} and q''_{CHF} than double-sided, and this is seen in the bottom row of Fig. 27. At high subcoolings, the bulk fluid promotes rapid condensation of the produced vapor, so more liquid is available to resupply the surface for continued boiling, delaying ONBD and CHF to higher heat fluxes. Here, the void fraction does not increase to an extent to offer significant flow acceleration to delay CHF. For the same q''_w,

compared to double-sided, single-sided preserves the condensation potential by not letting the fluid subcooling to quickly increase.

5.3 Identification of Threshold Inlet Subcooling/Quality for Heating Configuration Effects on Heat Transfer

Clearly, there exists a $\Delta T_{sub,in}$ threshold at which the acceleration effects balance condensation effects in removing the produced vapor, resulting in independence of heating configuration on heat transfer. Above this threshold, condensation effects dominate and single-sided sustains nucleate boiling to larger heat fluxes, and below which, acceleration effects dominate and double-sided better sustains boiling. This behavior seems independent of p_{in} (compare the left and right columns in Fig. 27).

An attempt is made to verify this behavior and identify this threshold by performing ISS experiments for small increments of $\Delta T_{sub,in} \approx$ 2, 4, 6, 8, 10, 15, 20, 25, 30, 35, 40, 45.6°C at high p_{in}; of these 12 subcoolings, only 5 are presented in Fig. 27 for discussion, and the other subcoolings did conform to these trends. For $G \approx 200$ kg/m^{2}s, the threshold $\Delta T_{sub,in}$ value lies in the range 19.73 – 28.98°C (or threshold $x_{e,in}$ within -0.27 – -0.39), but practical limitations prohibited the precise determination of this threshold. For instance, in row 4 of Fig. 27, the single-sided experiment was terminated halfway due to severe flow instabilities resulting in a ‘low tach’ warning from the pump and similar operating conditions were not tested for single-sided to safeguard the facility [24].

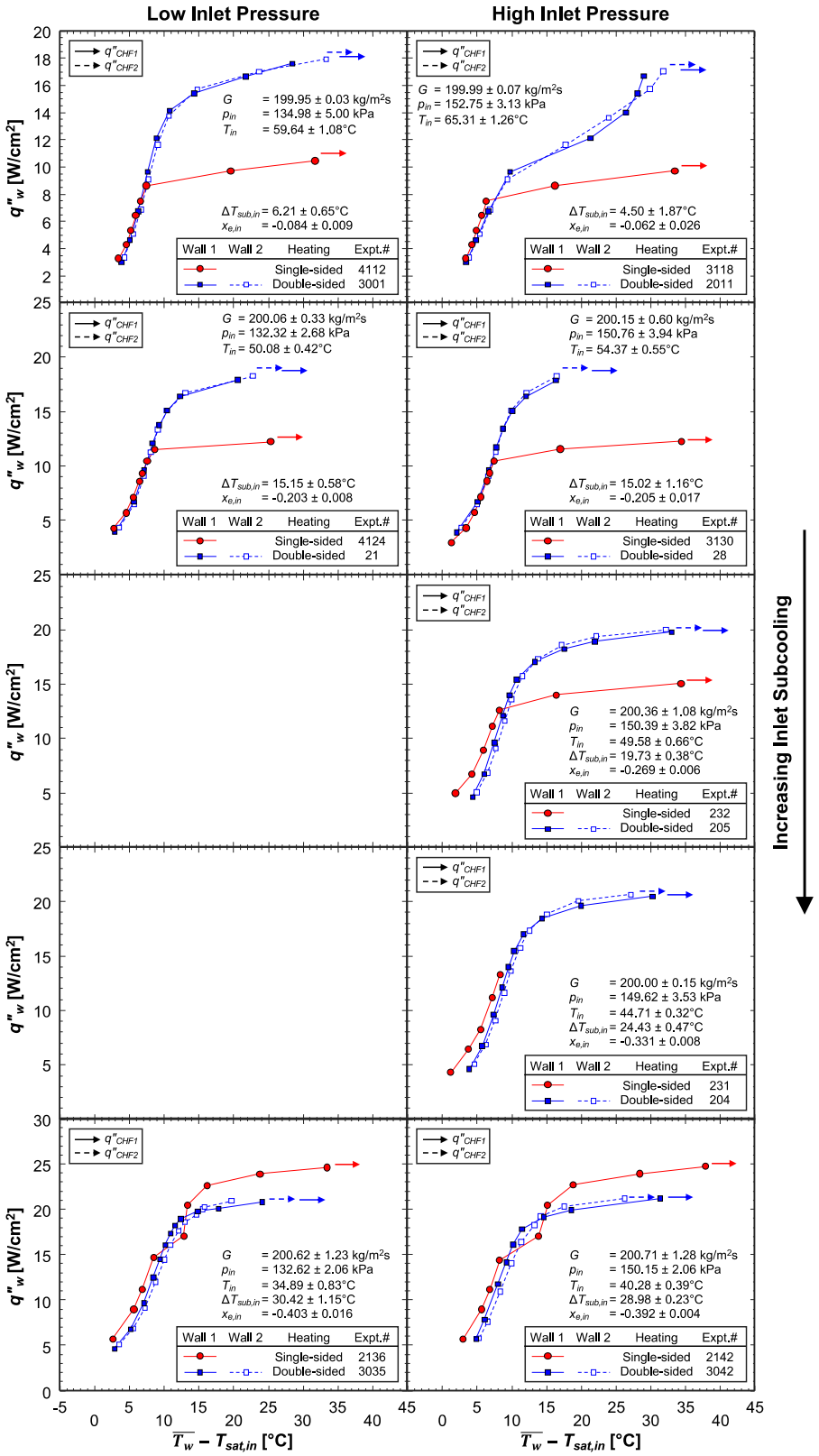

Fig. 27 Flow boiling curves comparing single- and double-sided heating for the lowest mass velocity of $G \approx 200$ kg/m^{2}s at a variety of inlet conditions (five inlet subcoolings at two inlet pressures). Exact operating conditions (mass velocity, G, inlet pressure, p_{in}, inlet temperature, T_{in}, inlet subcooling, $\Delta T_{sub,in}$, and inlet quality, $x_{e,in}$) for the data in each plot are included within the respective plot. Within each plot, each curve pertains to a different heating configuration.

5.4 Dependence of Threshold Inlet Subcooling/Quality upon Mass Velocity

There still lies the question of whether all G yield the same behavior and threshold $\Delta T_{sub,in}$. So, the aforementioned (fine) $\Delta T_{sub,in}$ increments were experimented at a moderate G of ~800 and a high G of ~2400 kg/m^{2}s, which are respectively shown in Figs. 28 and 29. Fig. 28 shows, for $G \approx 800$ kg/m^{2}s, similar behavior with the threshold $\Delta T_{sub,in}$ lying in the range 24.45 – 29.63°C (or threshold $x_{e,in}$ within -0.33 – -0.40). Note that the flow behavior above and below this threshold for $G \approx 800$ kg/m^{2}s is already presented in Fig. 26 for reference. Fig. 29 shows similar behavior for $G \approx 2400$ kg/m^{2}s, but the exact value of threshold $\Delta T_{sub,in}$ is captured as a wide range of 19.48 – 28.41°C (or threshold $x_{e,in}$ of -0.38 – -0.20) since the single- and double-sided curves fully overlap with the same q''_{CHF}. The combination of high G and high $\Delta T_{sub,in}$ results in very strong effects of condensation by the bulk liquid, which acts as a buffer in between the vapor layers produced at both walls and minimizes interaction between them (see Fig. 9(f) for example). This results in boiling and vapor layer growth on each wall to be isolated from each other. Note that in an authors' prior study [41], it was shown how the heat transfer coefficient for locally subcooled flow boiling is insignificantly affected by both heating configuration and gravitational field effects, especially when condensation effects are strong. Below this threshold, double-sided has higher q''_{CHF}. This is due to weak condensation effects resulting in vapor layer interaction after the fluid attains saturation conditions after a certain heat flux (for example, see Fig. 8(f), where for heat fluxes > 59% q''_{CHF}, $x_{e,out} > 0$ and the vapor layers merge). However, above this threshold, experiments could not be completed due to q''_{CHF} being large and the heaters practically reaching its upper power limit. Overall, it is concluded that the threshold $\Delta T_{sub,in}$ (or threshold $x_{e,in}$) is dependent on G, albeit to a minor extent.

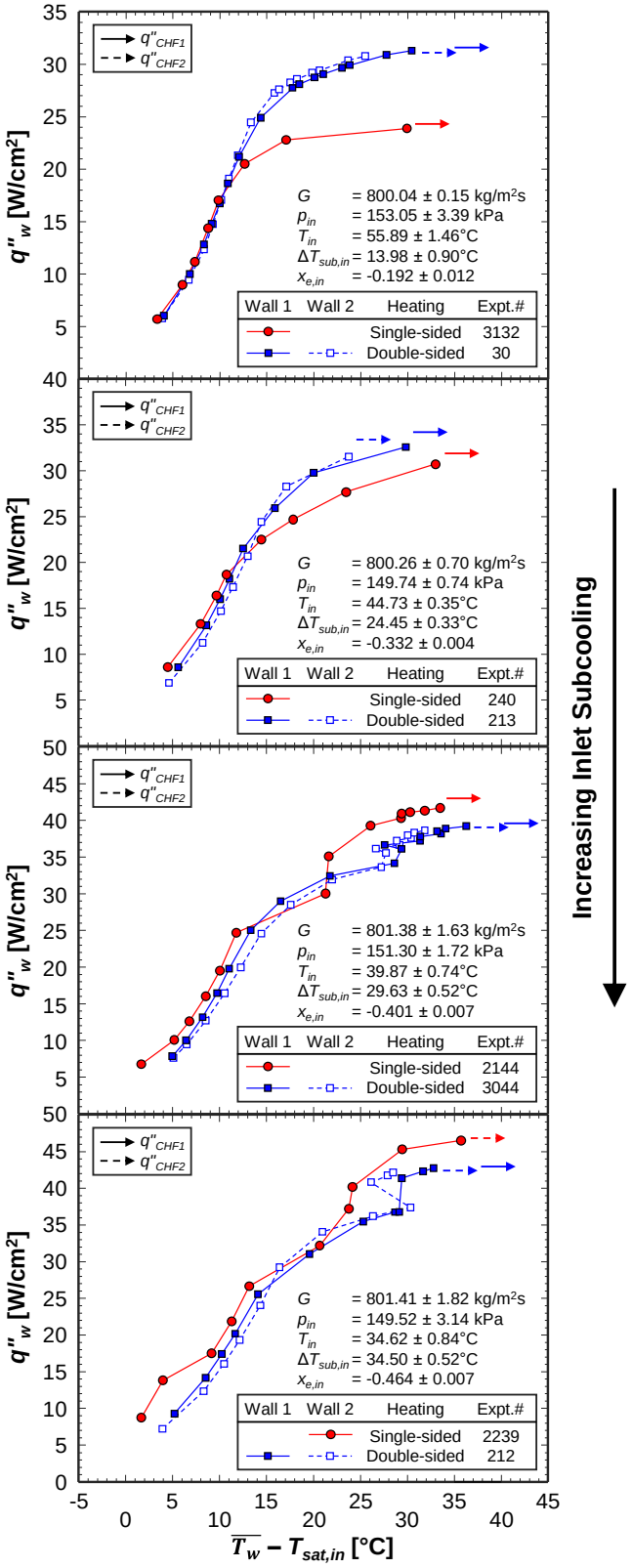

Fig. 28 Flow boiling curves comparing single- and double-sided heating for a moderate mass velocity of $G \approx 800$ kg/m^{2}s at a variety of inlet subcoolings. Exact operating conditions (mass velocity, G, inlet pressure, p_{in}, inlet temperature, T_{in}, inlet subcooling, $\Delta T_{sub,in}$, and inlet quality, $x_{e,in}$) for the data in each plot are included within the respective plot. Within each plot, each curve pertains to a different heating configuration.

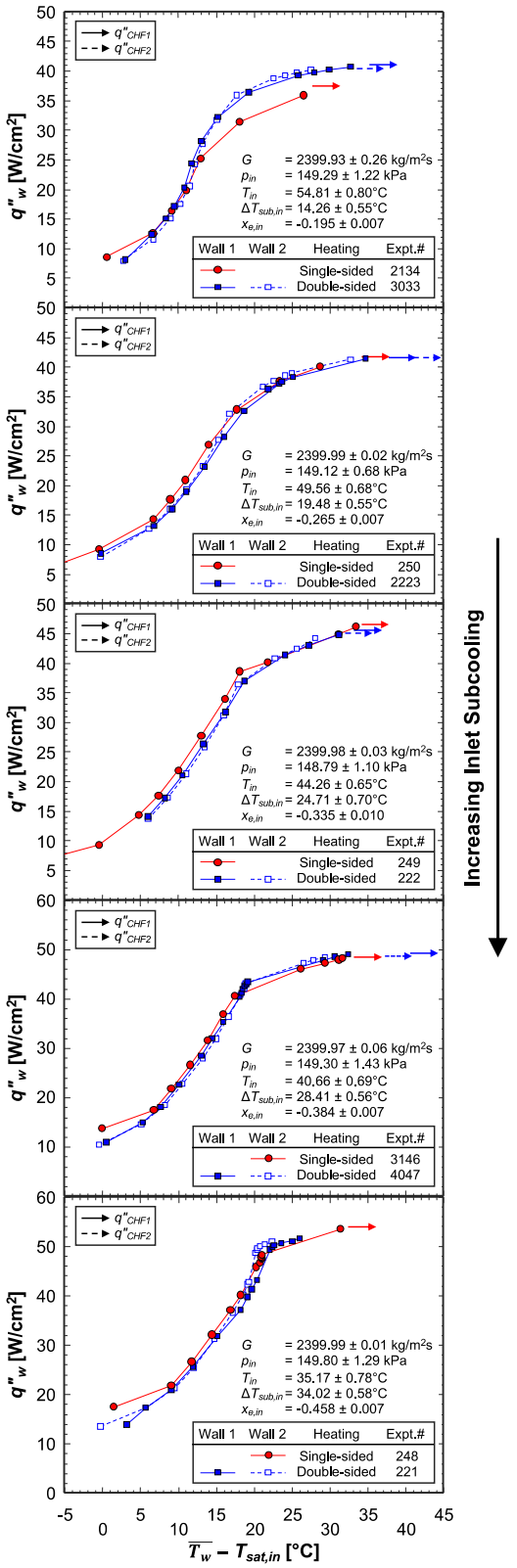

Fig. 29 Flow boiling curves comparing single- and double-sided heating for a high mass velocity of $G \approx 2400$ kg/m^{2}s at a variety of inlet subcoolings. Exact operating conditions (mass velocity, G, inlet pressure, p_{in}, inlet temperature, T_{in}, inlet subcooling, $\Delta T_{sub,in}$, and inlet quality, $x_{e,in}$) for the data in each plot are included within the respective plot. Within each plot, each curve pertains to a different heating configuration.

5.5 Heating Configuration Effects on Local Heat Transfer Performance

The local heat transfer performance of single- and double-sided heating is compared via Fig. 30, which contains plots depicting variations of local h (h_z) versus local x_e. Respectively arranged from the top to bottom are plots for combinations of high G and high $\Delta T_{sub,in}$, high G and low $\Delta T_{sub,in}$, low G and high $\Delta T_{sub,in}$, and low G and low $\Delta T_{sub,in}$, with the plots on the left and right columns respectively for single- and double-sided. Discussions on the parametric effects for double-sided is already done in section 4.3.2 and single-sided in [24], and they are similar and valid here. Focusing on the heating configuration effects, the top-row plots in Fig. 30 show the left and right plots being qualitatively similar, meaning the curves for each heat flux percentage are similar in shape and the trends are similar. The only significant difference seems to be the double-sided curves spanning a broader x_e range due to heat addition from two walls. This trend is also seen in the plots in rows 2, 3, and 4.

Row 3 shows, for moderate heat fluxes, a significantly different h_z versus x_e trend for single- and double-sided heating. This is due to the different fluid temperature used in the definitions for h, where the bulk fluid temperature is used as the fluid temperature for subcooled boiling conditions and saturation temperature at local pressure is used for saturated boiling conditions. However, the wall temperature does not show much difference between the two boiling regimes due to the necessity to attain a certain superheat for bubble nucleation. With subcooled bulk fluid temperatures always lower than the respective saturation temperatures, h is higher for saturated boiling than subcooled boiling. Now, refer to row 3, all the curves for single-sided heating remain within the subcooled regime with low h_z, however, the broader x_e range for double-sided heating results in operation within the saturated boiling regime with high h_z for $x_e \geq 0$. The same reasoning applies for the differences in row 2, albeit to a lesser extent.

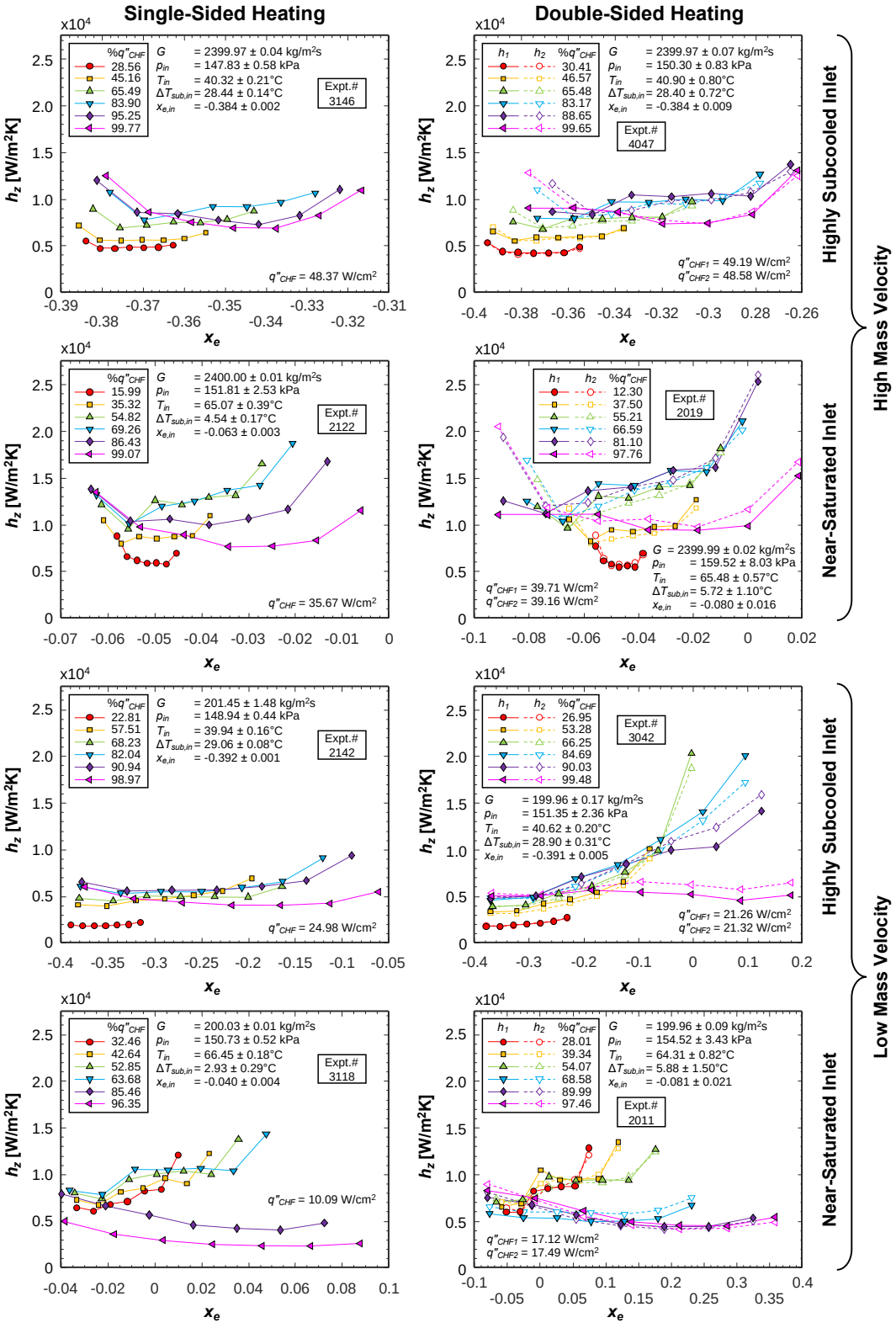

Fig. 30 Comparison of local heat transfer for single- and double-sided heating: Variations of local heat transfer coefficient variations, h_z, versus local thermodynamic equilibrium quality, x_e, for different heat flux percentages at a variety of operating conditions. Exact operating conditions (mass velocity, G, inlet pressure, p_{in}, inlet temperature, T_{in}, inlet subcooling, $\Delta T_{sub,in}$, and inlet quality, $x_{e,in}$) for the data in each plot are included within the respective plot. Within each plot, each curve pertains to a different heat flux, q''_w.

6. Conclusions

This study explored microgravity flow boiling of nPFH in a rectangular channel of 5.0 mm height, 2.5 mm width (heated), and 114.6 mm length, with subcooled inlet conditions. Experiments were successfully performed using the FBCE on the ISS to amass a large database for both single- and double-sided heating of a rectangular channel in a long-duration, high-quality microgravity environment. The database spans broad ranges of mass velocity (199.4 – 3200.0 kg/m^{2}s) and inlet subcooling (0.2 – 46.0°C) at two inlet pressures (124.2 – 176.7 kPa). With the single-sided results already reported in [24], firstly, this study reported the experimental flow visualization and heat transfer results for double-sided heating. High-speed-video images were presented portraying flow patterns and temporal flow behavior, and local flow velocities of vapor were measured and compared with volumetric mean velocity to analyze flow acceleration due to vapor production alone (and not buoyancy). Heat transfer results were reported in the form of flow boiling curves and both parametric curves and streamwise profiles of wall temperature and heat transfer coefficient. Parametric effects on these boiling aspects were ascertained for double-sided heating in microgravity. Secondly, the effects of heating configuration were analyzed by comparing and contrasting flow and heat transfer data for single- and double-sided heating. Key conclusions are as follows:

(i) Investigation of the parametric effects of mass velocity, inlet subcooling, and inlet pressure on flow behavior and heat transfer for double-sided heating revealed, at low $\Delta T_{sub,in}$, boiling curves overlap in the nucleate boiling regime for all G. However, at low G, vapor production is rapid, and vapor occupies nearly the entire channel, which in turn impedes nucleate boiling and degrades heat transfer at relatively low heat fluxes. For instance, at the lowest $G \approx 200$ kg/m^{2}s with $\Delta T_{sub,in} \approx 16.2$°C and 71% q''_{CHF}, the bulk fluid has an inlet velocity of 0.1 m/s, but rapid vapor production results in vapor velocities as high as 1.1 m/s just midway along the channel. But even this significant acceleration is unable to resupply the wall with fresh liquid and promote nucleate boiling. At high G, the inherently strong flow inertia causes vapor to be flushed out of the channel more rapidly, extending nucleate boiling to and enhancing heat transfer at higher heat fluxes. At high $\Delta T_{sub,in}$, boiling curves do not overlap as they do for low $\Delta T_{sub,in}$. Stronger condensation effects of the subcooled liquid at the liquid-vapor interface increase with G, resulting in thinner vapor layers within the channel and enhanced heat transfer. The effects of condensation become significant for around $G \geq 2400$ with $\Delta T_{sub,in} \geq 15$°C. Inlet pressure insignificantly affects all flow boiling aspects, except wall temperature, which is higher at higher pressure.

(ii) Flow instabilities, manifesting as temporal anomalies in flow behavior and large oscillations in pressure and temperature, increase in severity upon increasing heat flux and/or decreasing mass velocity (*i.e.*, increasing Boiling number). For double-sided heating at moderate mass

velocity of $G \approx 801$ kg/m^{2}s and highly subcooled inlet of $\Delta T_{sub,in} \approx 29.5$°C, severe flow reversal causing significant fluctuations in both mass flow rate and inlet pressure commence at 86% q''_{CHF}. Flow reversal within the channel result in abnormalities in the boiling curves at moderate G and high $\Delta T_{sub,in} \geq 29.5$°C.

(iii) Flow patterns for double-sided heating are more complex than those for single-sided heating, observed in [24], as the two vapor layers interact with each other. They first mesh together like mechanical gear teeth with a wavy liquid core separating them and then completely merge at a downstream location when the liquid either vaporizes or gets churned into the vapor to form a chaotic two-phase mixture. This is prevented at high subcooling with a high mass velocity, where condensation effects from the central liquid core isolate the two vapor layers. Regardless of the different flow patterns, both single- and double-sided heating result in similar parametric trends and local heat transfer coefficients for similar operating conditions, *i.e.*, combinations of G, $\Delta T_{sub,in}$, p_{in}, and % q''_{CHF}. However, the curves are stretched over a broader local-quality range for double-sided as heat addition from both walls increases the quantity of vapor within the channel more rapidly than single-sided.

(iv) The heat fluxes at which ONBD and CHF occur are distinctly different for single- and double-sided heating. These heat fluxes are larger for single-sided heating at high inlet subcoolings, where the bulk fluid's local subcooling is better preserved downstream, enhancing condensation of vapor near the heated wall. On the other hand, the heat fluxes are augmented for double-sided heating at low inlet subcoolings, where vapor production along both walls significantly accelerates the bulk flow, supplying the heated wall with fresh liquid. The threshold inlet subcooling/quality demarcating these effects is somewhat dependent on mass velocity (with higher G increasing the threshold). At $G \approx 200 – 2400$ kg/m^{2}s, the threshold $\Delta T_{sub,in}$ lies in the approximate range of 20 – 30°C (*i.e.*, threshold $x_{e,in}$ of roughly -0.40 – -0.20).

CRediT author contribution statement – **I. Mudawar**: Conceptualization, Methodology, Supervision, Writing – review and editing, Funding acquisition. **V.S. Devahdhanush**: Methodology, Software, Formal analysis, Investigation, Data curation, Writing – original draft, Writing – review and editing. **S.J. Darges**: Formal analysis, Investigation, Writing – original draft. **M.M. Hasan**: Conceptualization, Investigation, Writing – review and editing. **H.K. Nahra**: Investigation, Writing – review and editing. **R. Balasubramaniam**: Investigation, Writing – review and editing. **J.R. Mackey**: Investigation.

Declaration of Competing Interest – None. The authors declare that they have no known competing financial interests or personal relationships that could have appeared to influence the

work reported in this paper.

Data Availability – The experimental data presented in this paper, along with the raw data for all experimental cases in Table 4, will be publicly made available in a NASA repository later.

Acknowledgement – The authors are appreciative of the support of the National Aeronautics and Space Administration (NASA) under grant no. 80NSSC22K0328. The authors are also thankful to the FBCE personnel at NASA Glenn Research Center, Cleveland, Ohio, especially Nancy Hall (FBCE Project Manager), Rochelle May and Phillip Gonia (Software Engineering), Mark Sorrells (Assembly, Integration and Test Lead), Jesse DeFiebre (Fluids Lead), Monica Guzik (FBCE Chief Engineer), and ZIN FCF Mission Operations Team, for their dedicated technical assistance and successful completion of ISS testing.

References

[1] F.P. Chiaramonte, J. McQuillen, H.K. Nahra, P. Manoharan, H. Vanhala, B.J. Motil, J. Kim, V. Carey, W.G. Anderson, J. Plawsky, L. Carter, A. Jackson, 2019 NASA division of space and life and physical sciences research and applications fluid physics workshop report, NASA/CP-20205001256, NASA Glenn Research Center, Cleveland, OH, USA, 2020.

[2] C. Konishi, I. Mudawar, M.M. Hasan, Criteria for negating the influence of gravity on flow boiling critical heat flux with two-phase inlet conditions, Int. J. Heat Mass Transfer 65 (2013) 203–218, doi: 10.1016/j.ijheatmasstransfer.2013.05.070.

[3] L.E. O'Neill, I. Park, C.R. Kharangate, V.S. Devahdhanush, V. Ganesan, I. Mudawar, Assessment of body force effects in flow condensation, part II: Criteria for negating influence of gravity, Int. J. Heat Mass Transfer 106 (2017) 313–328, doi: 10.1016/j.ijheatmasstransfer.2016.07.019.

[4] J. Straub, Boiling heat transfer and bubble dynamics in microgravity, Adv. Heat Transfer 35 (2001) 57–172, doi: 10.1016/S0065-2717(01)80020-4.

[5] M. Misawa, An experimental and analytical investigation of flow boiling heat transfer under microgravity conditions, Ph.D. thesis, University of Florida, FL, USA, 1993.

[6] M. Saito, N. Yamaoka, K. Miyazaki, M. Kinoshita, Y. Abe, Boiling two-phase flow under microgravity, Nucl. Eng. Des. 146 (1–3) (1994) 451–461, doi: 10.1016/0029-5493(94)90350-6.

[7] H. Ohta, Experiments on microgravity boiling heat transfer by using transparent heaters, Nucl. Eng. Des. 175 (1–2) (1997) 167–180, doi: 10.1016/S0029-5493(97)00172-6.

[8] Y. Ma, J.N. Chung, An experimental study of forced convection boiling in microgravity, Int. J. Heat Mass Transfer 41 (15) (1998) 2371–2382.

[9] Y. Ma, J.N. Chung, An experimental study of critical heat flux (CHF) in microgravity forced-convection boiling, Int. J. Multiphase Flow 27 (10) (2001) 1753–1767, doi: 10.1016/S0301-9322(01)00031-3.

[10] H. Zhang, I. Mudawar, M.M. Hasan, Flow boiling CHF in microgravity, Int. J. Heat Mass Transfer 48 (15) (2005) 3107–3118, doi: 10.1016/j.ijheatmasstransfer.2005.02.015.

[11] S. Luciani, D. Brutin, C. Le Niliot, O. Rahli, L. Tadrist, Flow boiling in minichannels under normal, hyper-, and microgravity: Local heat transfer analysis using inverse methods, J. Heat Transfer 130 (10) (2008) 1–13, doi: 10.1115/1.2953306.

[12] S. Luciani, D. Brutin, C. Le Niliot, L. Tadrist, O. Rahli, Boiling heat transfer in a vertical microchannel: Local estimation during flow boiling with a non intrusive method, Multiphase Sci. Technol. 21 (4) (2009) 297–328, doi: 10.1615/MultScienTechn.v21.i4.30.

[13] C. Baltis, G.P. Celata, M. Cumo, L. Saraceno, G. Zummo, Gravity influence on heat transfer rate in flow boiling, Microgravity Sci. Technol. 24 (3) (2012) 203–213, doi: 10.1007/s12217-012-9298-5.

[14] D. Brutin, V.S. Ajaev, L. Tadrist, Pressure drop and void fraction during flow boiling in rectangular minichannels in weightlessness, Appl. Therm. Eng. 51 (1–2) (2013) 1317–1327, doi: 10.1016/j.applthermaleng.2012.11.017.

[15] M. Narcy, E. de Malmazet, C. Colin, Flow boiling in tube under normal gravity and microgravity conditions, Int. J. Multiphase Flow 60 (2014) 50–63, doi: 10.1016/j.ijmultiphaseflow.2013.11.011.

[16] C. Konishi, H. Lee, I. Mudawar, M.M. Hasan, H.K. Nahra, N.R. Hall, J.D. Wagner, R.L. May, J.R. Mackey, Flow boiling in microgravity: Part 1 – Interfacial behavior and experimental heat transfer results, Int. J. Heat Mass Transfer 81 (2015) 705–720, doi: 10.1016/j.ijheatmasstransfer.2014.10.049.

[17] Y. Zhang, B. Liu, J. Zhao, Y. Deng, J. Wei, Experimental study of subcooled flow boiling heat transfer on a smooth surface in short-term microgravity, Microgravity Sci. Technol. 30 (6) (2018) 793–805, doi: 10.1007/s12217-018-9629-2.

[18] M.T. Lebon, C.F. Hammer, J. Kim, Gravity effects on subcooled flow boiling heat transfer, Int. J. Heat Mass Transfer 128 (2019) 700–714, doi: 10.1016/j.ijheatmasstransfer.2018.09.011.

[19] D.M. Iceri, G. Zummo, L. Saraceno, G. Ribatski, Convective boiling heat transfer under microgravity and hypergravity conditions, Int. J. Heat Mass Transfer 153 (2020) 119614, doi: 10.1016/j.ijheatmasstransfer.2020.119614.

[20] B. Liu, B. Yuan, P. Xu, J. Zhao, Y. Zhang, J. Wei, Y. Yang, Q. Cao, A method for approximating the CHF of subcooled flow boiling in microgravity by ground tests, Int. J. Multiphase Flow 122 (2020) 103161, doi: 10.1016/j.ijmultiphaseflow.2019.103161.

[21] C. Konishi, I. Mudawar, Review of flow boiling and critical heat flux in microgravity, Int. J. Heat Mass Transfer 80 (2015) 469–493, doi: 10.1016/j.ijheatmasstransfer.2014.09.017.

[22] P. Di Marco, W. Grassi, Pool boiling in microgravity: Assessed results and open issues, in: Proceedings of 3rd European Thermal-Sciences Conference, Heidelberg, Germany, 2000, pp. 81–90.

[23] R. Raj, J. Kim, J. McQuillen, Pool Boiling Heat Transfer on the International Space Station: Experimental Results and Model Verification, J. Heat Transfer 134 (10) (2012) 101504, doi: 10.1115/1.4006846.

[24] I. Mudawar, V.S. Devahdhanush, S.J. Darges, M.M. Hasan, H.K. Nahra, R. Balasubramaniam, J.R. Mackey, Heat transfer and interfacial flow physics of microgravity flow boiling in single-side-heated rectangular channel with subcooled inlet conditions – Experiments onboard the International Space Station, Int. J. Heat Mass Transfer 207 (2023) 123998, doi: 10.1016/j.ijheatmasstransfer.2023.123998.

[25] H.S. Lee, H. Merte, F. Chiaramonte, Pool boiling curve in microgravity, J. Thermophys. Heat Transfer 11 (2) (1997) 216–222, doi: 10.2514/2.6225.

[26] H. Merte, Momentum effects in steady nucleate pool boiling during microgravity, Ann. N. Y. Acad. Sci. 1027 (2004) 196–216, doi: 10.1196/annals.1324.018.

[27] J.F. Zhao, G. Liu, S.X. Wan, N. Yan, Bubble dynamics in nucleate pool boiling on thin wires in microgravity, Microgravity Sci. Technol. 20 (2) (2008) 81–89, doi: 10.1007/s12217-008-9010-y.

[28] J.F. Zhao, J. Li, N. Yan, S.F. Wang, Bubble behavior and heat transfer in quasi-steady pool boiling in microgravity, Microgravity Sci. Technol. 21 (S1) (2009) 175–183, doi: 10.1007/s12217-009-9151-7.

[29] V.K. Dhir, G.R. Warrier, E. Aktinol, D. Chao, J. Eggers, W. Sheredy, W. Booth, Nucleate pool boiling experiments (NPBX) on the International Space Station, Microgravity Sci. Technol. 24 (5) (2012) 307–325, doi: 10.1007/s12217-012-9315-8.

[30] G.R. Warrier, V.K. Dhir, D.F. Chao, Nucleate pool boiling experiment (NPBX) in microgravity: International Space Station, Int. J. Heat Mass Transfer 83 (2015) 781–798, doi: 10.1016/j.ijheatmasstransfer.2014.12.054.

[31] O. Oikonomidou, S. Evgenidis, C. Argyropoulos, X. Zabulis, P. Karamaoynas, M.Q. Raza, J. Sebilleau, F. Ronshin, M. Chinaud, A.I. Garivalis, M. Kostoglou, A. Sielaff, M. Schinnerl, P. Stephan, C. Colin, L. Tadrist, O. Kabov, P. Di Marco, T. Karapantsios, Bubble growth analysis during subcooled boiling experiments on-board the international space station: Benchmark image analysis, Advances in Colloid and Interface Science 308 (2022) 102751, doi: 10.1016/j.cis.2022.102751.

[32] M. Bucci, M. Zupančič, A.I. Garivalis, A. Sielaff, P. Di Marco, I. Golobič, The role of the electric field in the departure of vapor bubbles in microgravity, Physics of Fluids 35 (1) (2023) 017109, doi: 10.1063/5.0127123.

[33] A. Sielaff, D. Mangini, O. Kabov, M.Q. Raza, A.I. Garivalis, M. Zupančič, S. Dehaeck, S. Evgenidis, C. Jacobs, D. Van Hoof, O. Oikonomidou, X. Zabulis, P. Karamaounas, A. Bender, F. Ronshin, M. Schinnerl, J. Sebilleau, C. Colin, P. Di Marco, T. Karapantsios, I. Golobič, A. Rednikov, P. Colinet, P. Stephan, L. Tadrist, The multiscale boiling investigation on-board the International Space Station: An overview, Appl. Therm. Eng. 205 (2022) 117932, doi: 10.1016/j.applthermaleng.2021.117932.

[34] H. Ohta, H. Asano, O. Kawanami, K. Suzuki, R. Imai, Y. Shinmoto, S. Matsumoto, T. Kurimoto, H. Takaoka, K. Fujii, M. Sakamoto, K. Sawada, H. Kawasaki, A. Okamoto, K. Kogure, T. Oka, K. Usuku, T. Tomobe, M. Takayanagi, Development of boiling and two-phase flow experiments on board ISS (Research objectives and concept of experimental setup), Int. J. Microgravity Sci. Appl. 33 (1) (2016) 330101, doi: 10.15011/ijmsa.33.330102.

[35] K. Inoue, H. Ohta, Y. Toyoshima, H. Asano, O. Kawanami, R. Imai, K. Suzuki, Y. Shinmoto, S. Matsumoto, Heat loss analysis of flow boiling experiments onboard International Space Station with unclear thermal environmental conditions (1st Report: Subcooled liquid flow conditions at test section inlet), Microgravity Sci. Technol. 33 (2) (2021) 28, doi: 10.1007/s12217-021-09869-5.

[36] K. Inoue, H. Ohta, H. Asano, O. Kawanami, R. Imai, K. Suzuki, Y. Shinmoto, T. Kurimoto, S. Matsumoto, Heat loss analysis of flow boiling experiments onboard International Space Station with unclear thermal environmental conditions (2nd Report: Liquid-vapor two-phase flow conditions at test section inlet), Microgravity Sci. Technol. 33 (5) (2021) 57,

doi: 10.1007/s12217-021-09902-7.

[37] P. Chorin, A. Boned, J. Sebilleau, C. Colin, O. Schoele-Schulz, N. Picchi, C. Schwarz, B. Toth, D. Mangini, Conception of a compact flow boiling loop for the International Space Station- First results in parabolic flights, Comptes Rendus. Mécanique 351 (S2) (2023) 1–20, doi: 10.5802/crmeca.147.

[38] V.S. Devahdhanush, I. Mudawar, H.K. Nahra, R. Balasubramaniam, M.M. Hasan, J.R. Mackey, Experimental heat transfer results and flow visualization of vertical upflow boiling in Earth gravity with subcooled inlet conditions – In preparation for experiments onboard the International Space Station, Int. J. Heat Mass Transfer 188 (2022) 122603, doi: 10.1016/j.ijheatmasstransfer.2022.122603.

[39] S.J. Darges, V.S. Devahdhanush, I. Mudawar, H.K. Nahra, R. Balasubramaniam, M.M. Hasan, J.R. Mackey, Experimental results and interfacial lift-off model predictions of critical heat flux for flow boiling with subcooled inlet conditions – In preparation for experiments onboard the International Space Station, Int. J. Heat Mass Transfer 183 (2022) 122241, doi: 10.1016/j.ijheatmasstransfer.2021.122241.

[40] V.S. Devahdhanush, S.J. Darges, I. Mudawar, H.K. Nahra, R. Balasubramaniam, M.M. Hasan, J.R. Mackey, Flow visualization, heat transfer, and critical heat flux of flow boiling in Earth gravity with saturated liquid-vapor mixture inlet conditions – In preparation for experiments onboard the International Space Station, Int. J. Heat Mass Transfer 192 (2022) 122890, doi: 10.1016/j.ijheatmasstransfer.2022.122890.

[41] V.S. Devahdhanush, I. Mudawar, Subcooled flow boiling heat transfer in a partially-heated rectangular channel at different orientations in Earth gravity, Int. J. Heat Mass Transfer 195 (2022) 123200, doi: 10.1016/j.ijheatmasstransfer.2022.123200.

[42] S.J. Darges, V.S. Devahdhanush, I. Mudawar, Assessment and development of flow boiling critical heat flux correlations for partially heated rectangular channels in different gravitational environments, Int. J. Heat Mass Transfer 196 (2022) 123291, doi: 10.1016/j.ijheatmasstransfer.2022.123291.

[43] I. Mudawar, S.J. Darges, V.S. Devahdhanush, Parametric experimental trends, interfacial behavior, correlation assessment, and interfacial lift-off model predictions of critical heat flux for microgravity flow boiling with subcooled inlet conditions – Experiments onboard the International Space Stat, Int. J. Heat Mass Transfer 213 (2023) 124296, doi: 10.1016/j.ijheatmasstransfer.2023.124296.

[44] W.A. Arnold, T.G. Hartman, J. McQuillen, Chemical characterization and thermal stressing studies of perfluorohexane fluids for space-based applications, J. Spacecr. Rockets 44 (1) (2007) 94–102, doi: 10.2514/1.22537.

[45] J. Lee, V.S. Devahdhanush, S.J. Darges, I. Mudawar, Effects of flow loop compressible volume position on system instabilities during flow boiling in micro-channel heat sinks, Int. J. Heat Mass Transfer 198 (2022) 123394, doi: 10.1016/j.ijheatmasstransfer.2022.123394.

[46] E.W. Lemmon, I.H. Bell, M.L. Huber, M.O. McLinden, NIST Standard Reference Database 23: Reference Fluid Thermodynamic and Transport Properties-REFPROP, Version 10, NIST, Gaithersburg, MD, USA, 2018.

[47] C. Konishi, I. Mudawar, M.M. Hasan, Investigation of localized dryout versus CHF in saturated flow boiling, Int. J. Heat Mass Transfer 67 (2013) 131–146, doi: 10.1016/j.ijheatmasstransfer.2013.07.082.